Cavity-Enabled Spin Squeezing
for a Quantum-Enhanced Atomic Clock

by

Monika Helene Schleier-Smith

A.B., Harvard University (2005)

Submitted to the Department of Physics
in partial fulfillment of the requirements for the degree of

Doctor of Philosophy

at the

MASSACHUSETTS INSTITUTE OF TECHNOLOGY

June 2011

Author . . . .
Department of Physics
May 06, 2011

Certified by . . . .
Vladan Vuletić
Lester Wolfe Associate Professor of Physics
Thesis Supervisor

Accepted by . . . .
Krishna Rajagopal
Associate Department Head for Education

Cavity-Enabled Spin Squeezing
for a Quantum-Enhanced Atomic Clock

by

Monika Helene Schleier-Smith

Submitted to the Department of Physics
on May 06, 2011, in partial fulfillment of the
requirements for the degree of
Doctor of Philosophy

Abstract

For the past decade, the stability of microwave atomic clocks has stood at the standard quantum limit, set by the projection noise inherent in measurements on ensembles of uncorrelated particles. Here, I demonstrate an atomic clock that surpasses this limit by operating with atoms in a particular type of entangled state called a "squeezed spin state." The generation of non-classical spin correlations in a dilute cloud of atoms is facilitated by an optical cavity, which allows for strong collective coupling of the atomic ensemble to a single mode of light. Since the light exiting the cavity is entangled with the atoms, an appropriate measurement performed on the light field can project the atomic ensemble into a squeezed spin state. I demonstrate 3.0(8) dB of spin squeezing by this method of quantum non-demolition measurement. I further introduce a new method, cavity feedback squeezing, which uses the light field circulating in the resonator to mediate an effective interaction among the atoms. The light-mediated interaction mimics the spin dynamics of the one-axis twisting Hamiltonian, under which a coherent spin state evolves deterministically into a squeezed spin state. The states prepared by cavity feedback are intrinsically squeezed by up to 10(1) dB and detectably squeezed by up to 5.6(6) dB. Applied in an atomic clock, they produce an Allan variance 4.7(5) dB below the standard quantum limit for averaging times of up to 50 s.

In a detour from engineering collective spin dynamics, I present direct observations of collective motional dynamics of atoms under the influence of cavity cooling. I demonstrate cooperatively enhanced cooling of a single collective motional mode down to a mean occupation number of 2.0 (-0.3/+0.9) phonons. The cooling is quantitatively well described by a simple, analytic quantum optomechanical model.

Thesis Supervisor: Vladan Vuletić
Title: Lester Wolfe Associate Professor of Physics

Acknowledgments

> Only where love and need are one,
> And the work is play for mortal stakes,
> Is the deed ever really done
> For heaven and the future's sakes.
> —Robert Frost, "Two Tramps in Mud Time."

Not that I ever felt the stakes were mortal, but much of the work I'm about to describe did seem like play. For that, Vladan Vuletić and Ian Leroux deserve my first and foremost thanks. Vladan is ever the optimist, a fount of clever ideas, a willing and gifted teacher; he is a role model both as a scientist and as a person. Ian, *never* the optimist, is an exceedingly constructive critic, capable of precisely and throughly analyzing any problem on the spot—with eloquence and humor to boot. I could not have dreamed of a better team to accompany me on the journey to my Ph.D.

In the waning of my graduate-school days, Hao Zhang and Mackenzie Van Camp have injected renewed enthusiasm into our lab. Though I have jokingly berated Hao for asking too many questions, the truth is that I have immensely enjoyed our discussions—in which I always manage to learn more than I teach. Looking back to the early days, I gratefully acknowledge Igor Teper and Yu-ju Lin for sharing their wisdom as I built my first laser and trapped my first cold atoms.

All of my colleagues in the Vuletić group have fostered an exceptionally nourishing environment, where no question is too stupid to ask and no piece of equipment too sacred to lend. I particularly want to thank my fellow members of the first generation at MIT: Marko Cetina, Andrew Grier, Jonathan Simon, Haruka Tanji-Suzuki, and (again) Ian Leroux.

En route to MIT and throughout my time here, I have greatly valued the mentorship and advice of James Ellenbogen, John Doyle, and Ike Chuang.

My pursuit of a Ph.D. has been free of financial stress thanks to the Hertz Foundation Daniel Stroock Fellowship—generously endowed by Ray Sidney—as well as the NSF.

For easing all other stress and for enriching me in deeper ways, I am indebted to my friends. Whether we've played music together or watched plays together; run, hiked, swum, biked, or boated together; whether you've cooked for me, cheered for me, or simply made me laugh, I am grateful for the times we've had. Melissa Dell, Tamar Mentzel, and Ardavan Oskooi: special thanks for putting up with more than your fair share.

Finally, I must thank my family—not only *ex officio*, but for inspiration and encouragement far beyond the call of duty. My brother, Johann Schleier-Smith, has been engaging my curiosity with scientific and mathematical questions for as long as I can remember. My mother, Ingeborg Schleier, has devoted herself selflessly to giving her children every opportunity to thrive. I trust that my father, Shedd Smith, would have been proud.

Contents

List of Figures

List of Tables

Chapter 1

Introduction

Over the past few decades, atomic clocks—and an array of analogous measurement devices ranging from magnetometers to accelerometers, all based on ensembles of atoms—have become extraordinarily well engineered. By 1999, the atomic fountain clock at the Paris Observatory reached the point where its stability was limited no longer by purely technical noise sources but rather by the statistical fluctuations inherent in the probabilistic behavior of uncorrelated events (or particles) [1]. This threshold of precision is known as the *standard quantum limit* (SQL). The challenge of 21st-century metrology, then, is to extend the engineering into the quantum regime—where controlling the quantum correlations among atoms in principle allows precision far beyond the SQL.

The bulk of this thesis describes the journey to first surpassing the standard quantum limit on stability in an atomic clock. In the present chapter, I explicate how this limit arises and introduce an approach to surpassing it called it *spin squeezing*. Here, the *spin* is an abstract representation of the clock's internal oscillator, which can be thought of as a spinning top whose gyrations mark the passage of time. The *squeezing* refers to redistributing the unavoidable quantum uncertainty in the spin's orientation to our advantage: at the expense of a greater uncertainty in how far the top is tilted, Heisenberg's uncertainty principle allows a reduced uncertainty in the phase of the top's precession, and thus a more precise measure of time.

Spin squeezing [2–4] relies on introducing non-classical correlations (entanglement) among the atoms constituting the clock. I will demonstrate two methods of introducing these correlations, both taking advantage of an interaction of the atoms with light confined in an optical cavity. For background, I first present the theory of the atom-light interaction (Ch. 2), the experimental setup (Ch. 3), and our manner of probing the atoms via the cavity (Ch. 4). This last facilitates the realization of a long-standing proposal [5] to induce spin squeezing by measurement [6–8], as I describe in Ch. 5: by detecting the light that emerges from the cavity, we obtain information about the atomic ensemble as a whole but not about the state of any individual atom, and as a result the ensemble can no longer be described in terms of uncorrelated single-atom states. In Ch. 6, I propose [9]

and demonstrate [10] an alternative approach to squeezing that obviates the need for a measurement by letting the light circulating inside the cavity apply coherent feedback to the ensemble. This method produces the largest spin squeezing to date and enables the proof-of-principle demonstration of a quantum-enhanced atomic clock, which I present in Ch. 7.

The apparatus built to meet the technical demands of spin squeezing also lends itself to other experiments requiring sensitive probing of atomic ensembles. I illustrate this in Ch. 8 with a study in cavity cooling [11]—a method that holds promise for laser-cooling not only atoms but also molecules or indeed arbitrary polarizable particles, but whose effect on any more than a single particle is not yet fully understood. I show that in an ensemble, the many atoms cooperate to speed up cavity cooling of a particular collective motional mode; we directly observe this mode while cooling it close to the quantum ground state. The observations are well described by a simple model—based on an analogy with radiation-pressure cooling of a spring-mounted mirror—that helps to elucidate fundamental limits to cavity cooling in ensembles.

All of the work described in this thesis was done in close collaboration with Ian Leroux. While I have endeavored to give a self-contained account of our joint experiments, I occasionally take the liberty of omitting details that are covered in depth in his complementary dissertation [12].

1.1 Why Spin: Ensembles of Two-Level Atoms

It is no accident that the rapid development of atomic physics since the mid-twentieth century—fueled by the invention of the maser and the laser—has been accompanied by equally rapid advances in precision metrology. The arsenal of modern metrology includes a broad class of instruments whose essential purpose is to determine the difference in energy ΔE between two discrete quantum states of an atom. These two states might, for example, be the magnetic-field-insensitive "clock states" [13] of the cesium atom; the resonant frequency $\nu_{\mathrm{Cs}} = \Delta E/h$ of the transition between them *defines* 1 second $\equiv 9,192,631,770/\nu_{\mathrm{Cs}}$. They might, alternatively, be two states with different magnetic moments, whose energy difference provides a sensitive measure of magnetic field. They might even be states of different momentum which, taking different trajectories through space, experience a difference in gravitational potential—allowing interferometric determination of the strength of the gravitational field. Thus clocks [1, 14–17], magnetometers [18–22], and gravimeters [23, 24]—as well as a host of other atom interferometers [25, 26]—can all benefit from perfecting the same task of measuring the energy difference between two atomic states (Fig. 1-1).

In order to measure an energy—a continuous quantity—using only a discrete, two-level system, one arranges for the measurement result to be encoded in a *probability* of finding

Atomic clock: ^{133}Cs hyperfine $\quad \Delta E/h \equiv 9\,192\,631\,770$ Hz $\quad |\uparrow\rangle \quad |\downarrow\rangle$

Magnetometer: $\quad \Delta E \propto B$

Gravimeter: $\quad \Delta U \propto g$

Figure 1-1: A variety of precision measurements rely on determining the energy difference between two discrete quantum states. The two states can always be represented abstractly as spin states $|\uparrow\rangle$ and $|\downarrow\rangle$, as illustrated for three examples discussed in the text: an atomic clock, measuring the ground-state hyperfine splitting in Cs, which defines the second; a magnetometer, measuring an energy splitting induced by a magnetic field B; and a gravimeter, using two states of different momentum to measure the local gravitational acceleration g via atom interferometry.

the system in one of its two states.[1] One can extract this probability either by repeated interrogation of a single particle or by interrogating many particles in parallel. A single aluminum ion under repeated interrogation [27, 28] currently constitutes the most accurate clock in the world. However, it takes this clock [28] half an hour just to reach a level of uncertainty that can be reached in one minute by an optical-lattice clock using an ensemble of $10^3 - 10^4$ strontium or ytterbium atoms [15, 17]. Wherever technically feasible, atomic precision measurement devices thus employ the parallelism of an ensemble. By using N *uncorrelated* atoms, these devices ideally attain a given statistical uncertainty N times faster than they would with a single atom. In this thesis, I demonstrate experimentally that we can engineer non-classical correlations among the atoms in an ensemble to obtain an even greater enhancement of measurement sensitivity with atom number N.

Any ensemble of N atoms with two states of interest—regardless of the details of their physical manifestation—can be regarded abstractly as a collection of spin-1/2 particles. Each such particle has two possible projections $s_z^i = \pm 1/2$ of its spin $\mathbf{s}_i$ along the z axis, allowing us to represent the state of the ith atom by s_z^i. For an atom in a superposition of the two (pseudo)-spin states $|\uparrow\rangle \equiv |s = 1/2, s_z = +1/2\rangle$, $|\downarrow\rangle \equiv |s = 1/2, s_z = -1/2\rangle$, the spin $\mathbf{s}$ has a well-defined azimuthal angle ϕ (with $\tan\phi = s_y/s_x$) that represents the quantum mechanical phase of the superposition $\sqrt{1/2 + \langle s_z\rangle} |\uparrow\rangle + \sqrt{1/2 - \langle s_z\rangle}e^{i\phi} |\downarrow\rangle$; as a function of time t, $\phi = \omega t$ precesses at the transition frequency $\omega = \Delta E/\hbar$. The state of the ensemble is then described (see Fig. 1-2(a)) by a similarly precessing *collective* spin vector $\mathbf{S} = \sum_{i=1}^{N} \mathbf{s}_i$ of length $|\langle\mathbf{S}\rangle| \leq S$, where the maximum possible length $S = N/2$—arising if all spins are aligned—characterizes pure states that are totally symmetric with respect to particle exchange [29, 30]. The collective spin projection $S_z = (N_\uparrow - N_\downarrow)/2$, represents the difference in populations $N_\uparrow, N_\downarrow$ of the two spin states $|\uparrow\rangle , |\downarrow\rangle$, a readily accessible observable in typical experiments.

1.2 Ramsey Spectroscopy and the Standard Quantum Limit

To measure the transition frequency ω, one typically employs the method of Ramsey spectroscopy, which is illustrated in Fig. 1-2(b). Starting with all atoms in $|\downarrow\rangle$, one applies a (near)-resonant field oscillating at $\omega_d \approx \omega$ to perform a $\pi/2$ rotation that places the ensemble spin vector in the xy-plane. Fig. 1-2 depicts this collective spin state in a frame rotating at ω_d, so that for $\omega_d = \omega$ the ensemble spin points along a fixed axis ($\mathbf{S} = S\hat{x}$). More generally, then, the spin precesses about the $\hat{z}$ axis at the detuning $\omega - \omega_d$, and one wishes to measure the phase $\phi = (\omega - \omega_d)T$ acquired in some fixed precession time T. In order to read out the phase $\phi = S_y/|\mathbf{S}|$ (with $\phi \ll 1$) at the end of the precession, one converts it by a rotation about $\hat{x}$ into a population difference $2S_z = N_\uparrow - N_\downarrow$ between the

---

[1]Specifically, the energy is encoded in the quantum mechanical phase between the two states, which can be converted to a probability of projection into one state or the other by the Ramsey sequence described in Sec. 1.2.
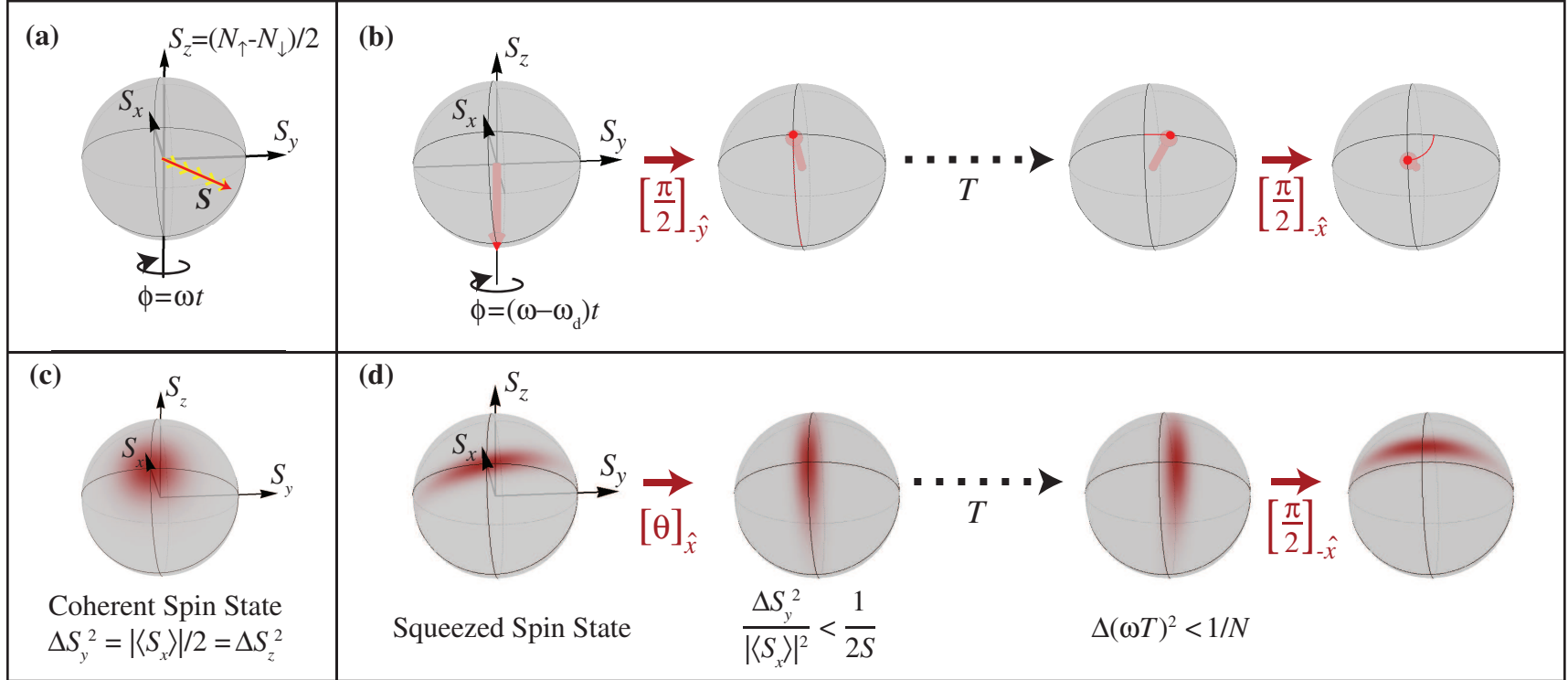
Figure 1-2: (a) Bloch-sphere representation of an ensemble of N two-level atoms as a spin vector $\mathbf{S} = \sum_{i=1}^{N} \mathbf{s}_i$ (red) formed by summing the single-atom spins $\mathbf{s}_i$ (yellow). The azimuthal angle ϕ represents the phase $\phi = \omega t$ of the spin precession, where the precession rate is set by the energy difference $\hbar\omega$ between states $|\uparrow\rangle$ and $|\downarrow\rangle$. The spin component S_z is directly proportional to the difference in populations $N_\uparrow, N_\downarrow$ of the two spin states. (b) Ramsey sequence for measurement of the clock transition frequency ω, illustrated in a rotating frame at the drive frequency ω_d, as described in text. Each arrow labeled $[\frac{\pi}{2}]_{\hat{r}}$ indicates a $\pi/2$ rotation about the axis $\hat{r}$. (c) Schematic illustration of a coherent spin state along $\hat{x}$ on the Bloch sphere; the red shading represents a tomographic probability distribution [31] for spin components in the yz plane, with variances $\Delta S_y^2 = |\langle S_x \rangle|/2 = \Delta S_z^2$ set by the length $|\langle S_x \rangle| = S$ of the ensemble spin vector for the totally symmetric state. (d) Modified Ramsey sequence incorporating a squeezed spin state. The sequence is initiated by placing the state into the phase-squeezed orientation, so that the reduced quantum uncertainty $\Delta\phi^2 = \Delta S_y^2/|\langle S_x \rangle|^2 < 1/(2S)$ will allow the phase $\phi = \omega T$ acquired in the precession time T to be determined to better than the standard quantum limit.

two states. Since the individual atoms are uncorrelated, the spin state populations are binomially distributed, leading to fluctuations $\Delta S_z^2 = N/4 = S/2$ in the outcome of an ideal measurement of S_z. These fluctuations result in an uncertainty

$$\Delta(\omega T)^2{}_{\text{SQL}} = \Delta S_z^2/|\langle \mathbf{S} \rangle|^2 = 1/N \tag{1.1}$$

in the phase acquired during the precession. This, the standard quantum limit (SQL) on clock precision, is the best phase measurement possible with N *uncorrelated* atoms [3, 4]. The ensemble spin state used in the Ramsey sequence to attain this limit, a totally symmetric product of the single-atom spins, is called a *coherent spin state* (CSS) [30]; the fluctuations in the outcome of the Ramsey measurement correspond to a quantum uncertainty in the spin's orientation, illustrated schematically in Fig. 1-2(c).

The SQL is a *quantum* limit in the sense that it arises from the quantization of the collective spin in units of individual atoms and vanishes in the large-N limit of a classical, continuously variable spin. However, the SQL is not the fundamental limit set by quantum mechanics; a way of overcoming it is suggested [2–4] by considering a truly fundamental limit set by the Heisenberg uncertainty relation:

$$\Delta S_y^2 \Delta S_z^2 \geq \left| \langle [S_y, S_z] \rangle \right|^2 / 4 = \left| \langle S_x \rangle \right|^2 / 4 \tag{1.2}$$

Here, in the special case where $\Delta S_y^2 = \Delta S_z^2$, one recovers the SQL on phase sensitivity $\Delta S_y^2/|\langle S_x \rangle|^2 \geq 1/(2|\langle S_x \rangle|) \geq 1/(2S)$, equivalent to Eq. 1.1. In principle, though, the Heisenberg uncertainty relations allow a reduced uncertainty in one spin component transverse to the mean spin vector (e.g., S_y) at the expense of a greater uncertainty in the other transverse spin component (S_z). Such redistribution of the spin noise is called *spin squeezing* [2]. Fig. 1-2(d) illustrates a squeezed spin state as applied to surpass the SQL in Ramsey spectroscopy [4].

1.3 Spin Squeezing

I shall use the term "squeezing," specifically, to refer to reducing the noise-to-signal ratio $\Delta S_\perp^2/|\langle \mathbf{S} \rangle|^2$ in the orientation of a collective spin by introducing non-classical correlations among the particles; here, $S_\perp$ represents any spin component orthogonal to $\langle \mathbf{S} \rangle$. For an ensemble of $N = 2S$ particles, where the best signal-to-noise ratio attainable by an unentangled state is that given by Eq. 1.1, the spin state is then necessarily squeezed if it obeys the Wineland [3, 4] criterion

$$\frac{\Delta S_\perp^2}{|\langle \mathbf{S} \rangle|^2} < \frac{1}{2S}. \tag{1.3}$$

While various other metrics for squeezing can be found in the literature [2, 32–34], the Wineland criterion has the virtue of being a black-box test for both entanglement [32, 33]

and metrological gain, expressed in terms of experimentally measurable quantities, with no assumption that the spin state is symmetric or remains so throughout the squeezing process.

In accordance with Eq. 1.3, squeezing is quantified by the parameter $\zeta \equiv 2S\Delta S_\perp^2/|\langle \mathbf{S} \rangle|^2 < 1$ representing the reduction in noise-to-signal ratio (in variance) below the standard quantum limit. While this might appear to be a simple and unambiguous parametrization, there has nevertheless been some variability in its application in the literature produced by a flurry of recent experiments. The spin variance $\Delta S_\perp^2$ may, for example, include either the full measured noise—including detection noise—or only the noise inferred to be intrinsic to the quantum state. In Refs. [6] and [10], we account for imperfect initial coherence of the state subjected to squeezing by evaluating the reduction in noise-to-signal ratio $\zeta_0 \equiv 2S_0\Delta S_\perp^2/|\langle \mathbf{S} \rangle|^2 < 1$ relative to the best obtainable with a CSS of spin length $S_0 < S = N/2$. (The condition $\zeta_0^{-1} < 1$ guarantees both entanglement and metrological gain under the verifiable assumptions described in Sec. 5.5.) In reviewing demonstrations of spin squeezing below, I refer to Table 1.1 for a summary of results organized to facilitate comparison of various experiments on an equal footing.

A squeezed spin state of two ions—entangled via a quantum gate operation [35]—enabled the first demonstration of quantum-enhanced Ramsey spectroscopy ($\zeta^{-1} = 0.7(1)$ dB) in a landmark experiment by Meyer *et al.* in the group of David Wineland [36]. While up to 14 ions have since been entangled by similar means [44, 45], advances in spin squeezing have been driven by techniques more readily scalable to large ensembles of (neutral) atoms. These methods can broadly be placed into two classes: squeezing by collisional interaction [32, 37–39]; and light-induced squeezing [5–10, 43, 46].

Interparticle interactions, by providing a mechanism for non-classical correlations to develop among the particles, can induce a coherent spin state to evolve into a squeezed spin state [2]. Experiments with Bose-Einstein condensates in multi-well potentials have shown that collisional interactions can reduce the fluctuations in atom number per well [37, 47, 48]; for two wells represented as pseudospin states $|\uparrow\rangle$ and $|\downarrow\rangle$, spin squeezing has been verified in such a system [37]. For spin states corresponding instead to an internal (hyperfine) degree of freedom, the same collisional mechanism can produce squeezing given a state-dependent scattering length [32], as demonstrated in recent experiments by the groups of M. Oberthaler [38] and P. Treutlein [39]. Gross *et al.* [38] have inferred up to $\zeta^{-1} = 8.2(9)$ dB of spin squeezing by this approach (see Table 1.1).

In the context of metrology, one may wish to avoid interatomic interactions, as these perturb the transition frequency to be measured. Thus, there is considerable interest [5, 9, 49, 50] in inducing squeezing with light, which—although it also perturbs the transition frequency—can controllably be turned off after squeezing before initiating the precision measurement. An early foray in this vein effected a 1.4(4)% reduction in spin noise by optical pumping with ellipticity-squeezed light. Using only classical light, the hyperfine

21

Method	Notes	(Pseudo)-spin states	Particle number N	Spin Noise Reduction (dB)	Inferred Squeezing (dB)		Observed Squeezing (dB)		Ref.
Quantum gate [35]		^{9}Be$^+$ hf	2					0.7(1)	[36]
Collisional interaction [32]	Bose-Einstein condensates	Spatial	2×10^3	7(1)		3.8(3)			[37]
		^{87}Rb hf	4×10^2	8.2(9)		8.2		1.4	[38]
		^{87}Rb clock	1×10^3	3.7(4)		2.5(6)			[39]
QND Measurement [5]	free-space, Faraday rotation	^{133}Cs m_F	1×10^7	~ 5					[40]
		^{171}Yb m_I	3×10^5	1.8(1.5)					[41, 42]
	cavity, dispersive	^{87}Rb clock	3×10^4	**8.8(8)**	*3.0(8)*	**1.5(6)**			[6]
	free-space, dispersive	^{133}Cs clock	1×10^5	5.3(6)		3.4(7)		1.1	[7, 43]
	cavity, on resonance	^{87}Rb clock	7×10^5	4.9(6)	*3.4(6)*			1.1(4)	[8]
Cavity feedback [9]		^{87}Rb clock	3×10^4	**12(1)**	*10(1)*	**8.4(7)**	*5.6(6)*	**4.6(6)**	[10]

Table 1.1: State of the art in spin squeezing; results in bold are presented in this thesis. Experiments to date have demonstrated squeezing with the pseudo-spin states being clock states ("clock")—with a frequency difference insensitive to magnetic fields—or other hyperfine states ("hf") in ions or alkali atoms; or spatial states of a BEC in a multi-well potential. Also included are two experiments on QND measurement of a collective hyperfine or nuclear spin (states m_F or m_I), in which a noise reduction $S/(2\Delta S_\perp^2)$ was inferred but coherence was not quantified. While many experiments account for imperfect detection of the prepared states in inferring the degree of spin noise reduction or squeezing, others also (or instead) report the directly observed squeezing including detection noise. Tabulated here are the inferred spin noise reduction, inferred squeezing, and observed squeezing. In the tabulations of squeezing, upright numbers give the inverse Wineland parameter $\zeta^{-1} \equiv |\langle \mathbf{S} \rangle|^2/(2S\Delta S_\perp^2)$ quantifying improvement in signal-to-noise ratio over the standard quantum limit for the ensemble of $N = 2S$ particles; numbers in italics indicate squeezing $\zeta_0^{-1} = |\langle \mathbf{S} \rangle|^2/(2S_0\Delta S_\perp^2)$ relative to an unentangled reference state that is not fully coherent, with spin length $S_0 < N/2$.

spin $F = 4$ in individual Cs atoms has been squeezed [51, 52] by up to $\zeta^{-1} \approx 4$ dB under the influence of the tensor ac Stark shift; this squeezing is already close to its fundamental limit $\zeta^{-1} \lesssim F$ set by the total hyperfine spin.

A scalable approach to light-induced squeezing—proposed in a seminal paper by Kuzmich, Bigelow, and Mandel [5]—is to perform a quantum non-demolition (QND) measurement of a collective spin variable, e.g., S_z. By probing an ensemble optically, one can imprint information about S_z onto a light field, entangling the spin and field states. A measurement can then be performed on the light to reduce the conditional uncertainty in S_z [6–8, 40–42]. If the measurement sufficiently preserves the coherence of the atomic state, it can produce spin squeezing [6–8], as first demonstrated in the cavity-aided experiment [6] presented in Ch. 5 and in simultaneous work by the Polzik group (Appel *et al.*) in free space [7]. While both of these experiments used dispersive measurements with a far-detuned probe, a very recent cavity-based experiment has applied a resonant probing scheme [8]. The squeezing induced by QND measurement—up to $\zeta^{-1} = 3.4(7)$ dB to date [7]—is *conditional*, in the sense that a different squeezed state is prepared in each iteration of the experiment depending on the measurement outcome. This simply means that one must make use of the measurement information in order to benefit from the squeezing.

From a fundamental standpoint, a squeezed state is thus equally useful for metrology whether it is prepared conditionally or deterministically. Practically, however, the degree of squeezing achievable conditionally will always be limited by one's ability to perform a sensitive yet non-destructive measurement. An alternative approach to light-induced squeezing was suggested by Takeuchi *et al.* [49]: if, after the atoms imprint their collective state onto the light, the light is allowed to interact (in an appropriately designed way) with the atoms again, the resulting feedback can give rise to deterministic squeezing. I show in Ch. 6—both theoretically [9] and experimentally [10]—that the requisite feedback can be provided by the light circulating in an optical cavity. This method of cavity feedback induces up to $\zeta_0^{-1} = 10(1)$ dB of spin squeezing in our system, resulting in states that would yield a phase sensitivity $\zeta^{-1} = 8.4(7)$ dB beyond the standard quantum limit if we could detect them perfectly.

In an actual Ramsey measurement, the quantum projection noise will necessarily be augmented by detection noise, as well as by any classical phase noise encountered in the measurement. Thus, preparation of a squeezed state is not, by itself, sufficient to perform Ramsey spectroscopy beyond the standard quantum limit. Besides the pioneering two-ion squeezing experiment of Meyer *et al.* [36] described above, three very recent experiments with atomic ensembles have directly shown quantum-enhanced Ramsey interferometry. Louchet-Chauvet *et al.* have attained a 1.1 dB enhancement over the SQL via measurement squeezing [43]; and Gross *et al.* a 1.4 dB enhancement via collisional squeezing [38]. In Ch. 7 of this thesis, I demonstrate an atomic clock enhanced by 4.7(5) dB over

the standard quantum limit via cavity feedback squeezing [53].

Note that squeezed-state Ramsey spectroscopy is not the only approach to performing a phase measurement beyond the standard quantum limit. Using a maximally entangled (GHZ) state of three ions, Leibfried *et al.* have demonstrated a phase measurement 3.2(1) dB beyond the SQL [44]. At another extreme, in the group of Eugene Polzik, Wasilewski *et al.* have entangled two ensembles of $\sim 10^{12}$ atoms via conditional two-mode squeezing [54], thereby constructing a magnetometer that would already achieve impressive performance at the SQL but surpasses it by 1.5 dB [22]. Given the wide range of applications for atomic precision measurements—from time-keeping, through sensing and navigation, to precision tests of fundamental physics—a diversity of approaches to their quantum enhancement is entirely apropos.

1.4   Why the Optical Cavity

Opposite the collective atomic spin introduced above, the principle actor in this thesis is the optical cavity. I have alluded to the role of the cavity in manipulating the spin by optical feedback, but I have yet to introduce its more general role: the essential purpose of the cavity is simply to increase the optical depth of the atomic sample.

To understand the significance of the optical depth, recall that our light-induced squeezing methods—both measurement and cavity feedback—rely on probing a collective spin variable S_z. Knowledge of the collective variable S_z beyond the SQL requires either knowledge of the states of individual atoms or anti-correlations among the states of different atoms. The former corresponds to destruction of the superposition state and a loss of signal $|\langle S_x \rangle|$. We are interested instead in the latter—i.e., in probing *only* a collective variable without revealing the states of individual atoms. The only way that the atoms can reveal their states (via the probe light) is by scattering the probe photons. To obtain only collective information about the atomic states, one needs to ensure that the dominant scattering process is collective scattering into a single mode—specifically, forward-scattering into the mode of the probe light. This requires a large resonant optical depth OD $\gg 1$ of the ensemble [55, 56]. While optical depths up to OD $\sim 10^2$ are realizable in free space, much larger optical depths OD $\sim 10^4$ can be reached in a cavity due to the enhancement by the finesse. Correspondingly, fundamental limits to the performance of light-induced squeezing [55, 56] are most favorable in a cavity.

Chapter 2

Atom-Light Interaction

The interaction of our ensemble of atoms with probe light in the optical resonator is essential both in providing a mechanism for squeezing and in enabling us to characterize the ensemble spin state. In this chapter, I begin in Section 2.1 by introducing the key features of this interaction in a simplified model system. Sections 2.2-2.3 expand the treatment to describe our real experimental system, and Sec. 2.4 presents an experiment that both verifies of our calculated atom-resonator coupling and demonstrates the reversibility of decoherence associated with its inhomogeneity. Finally, Sec. 2.5 derives the cavity cooperativity and introduces its role in quantifying effects of spontaneous emission into free space.

2.1 Model System

The essential features of the atom-light interaction in our system are captured by a simplified model in terms of three-level atoms uniformly coupled to an optical cavity. I will discuss how our real system maps onto this model in Secs. 2.2-2.3 below. For now, let us assume that each atom has two stable ground states $|\uparrow\rangle, |\downarrow\rangle$ at energies $\pm\hbar\omega/2$; and an excited state $|e\rangle$—with linewidth Γ—at energy $\hbar\omega_0$, where ω_o is an optical frequency (see Fig. 2.1). Consider an ensemble of N such atoms, uniformly coupled to a cavity mode at frequency $\omega_c = \omega_o$, such that the detuning of the cavity from the $|\uparrow\rangle \rightarrow |e\rangle$ and $|\downarrow\rangle \rightarrow |e\rangle$ transitions has equal magnitude $\Delta = \omega/2$ but opposite sign. (We choose this symmetric arrangement for simplicity, because we are interested only in effects that distinguish between the two states.) The Hamiltonian for this system is

$$H_{\text{sys}} = \hbar\omega_c c^\dagger c + \hbar \sum_{i=1}^{N} \left(\frac{\omega}{2} \left[|\uparrow\rangle_i \langle\uparrow|_i - |\downarrow\rangle_i \langle\downarrow|_i \right] + \omega_o |e\rangle_i \langle e|_i + g \left[c |e\rangle_i \langle\uparrow|_i + c |e\rangle_i \langle\downarrow|_i + H.c. \right] \right),$$

(2.1)

where $2g$ represents the vacuum Rabi frequency.

We shall be interested in the dispersive aspect of the atom-light interaction and not in populating the atomic excited state. I therefore assume a large detuning $\Delta \gg \Gamma, \kappa$ of the
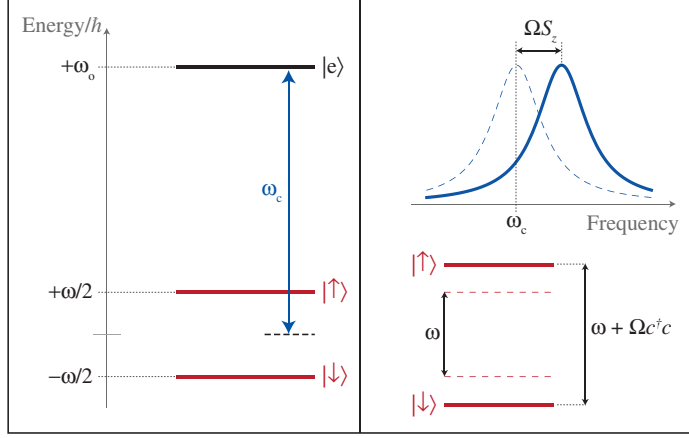
Figure 2-1: Energy diagram of model three-level system, as described in the text. The left panel shows the unshifted levels. The right panel illustrates the shift of the cavity resonance (blue) by ΩS_z and the differential ac Stark shift of the atomic levels (red) by $\Omega c^\dagger c$, relative to the situation in the absence of atom-cavity coupling (dashed).

cavity mode from atomic resonance. Here, for sufficiently low intracavity photon number $\langle c^\dagger c \rangle \ll (\Delta/g)^2$, we can adiabatically eliminate the excited state [57] to obtain an effective Hamiltonian

$$H_{\mathrm{sys}} = \hbar\omega_c c^\dagger c + \hbar \sum_{i=1}^{N} \left[\left(\frac{\omega}{2} + \frac{g^2}{\Delta} c^\dagger c \right) \left(|\uparrow\rangle_i \langle\uparrow|_i - |\downarrow\rangle_i \langle\downarrow|_i \right) \right]. \tag{2.2}$$

This Hamiltonian can be expressed more simply in terms of a collective spin operator $\mathbf{S}$, with z-component $S_z = \sum_{i=1}^{N} (|\uparrow\rangle_i \langle\uparrow|_i - |\downarrow\rangle_i \langle\downarrow|_i)/2$ proportional to the population difference between states $|\uparrow\rangle$ and $|\downarrow\rangle$. In terms of this collective spin, we have

$$H_{\mathrm{sys}}/\hbar = \omega_c c^\dagger c + \Omega c^\dagger c S_z + \omega S_z, \tag{2.3}$$

where $\Omega = 2g^2/\Delta$ quantifies the atom-light interaction. The effect of this interaction on the light is to shift the cavity resonance in proportion to S_z, via the opposite phase shifts imparted to the light by atoms in states $|\uparrow\rangle$ and $|\downarrow\rangle$. The effect on the atoms is to shift the transition frequency between states $|\uparrow\rangle$ and $|\downarrow\rangle$ in proportion to the number $c^\dagger c$ of photons in the cavity, via the differential ac Stark effect. The action of the atoms on the light can be used to perform a quantum non-demolition measurement of S_z by detecting the shift of the cavity resonance (Ch. 5). Alternatively, exploiting both facets of the interaction—namely, the modification of the light field *by* the atoms and the backaction of the modified light field *on* the atoms—allows for squeezing by cavity feedback (Ch. 6).
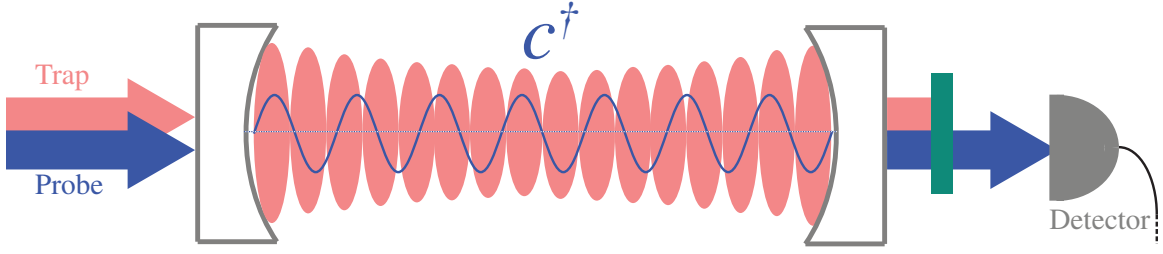
Figure 2-2: Atoms are trapped in a lattice (pink) that is incommensurate with the cavity mode used for probing (blue). To account for the inhomogeneous coupling of atoms to the probe light, we describe the atomic ensemble in terms of the appropriately weighted collective spin $\boldsymbol{\mathcal{S}}$ defined in Eq. 2.5.

2.2 Inhomogeneous Coupling

In our experiment, the atoms are confined within the cavity by an optical lattice that is incommensurate with the standing-wave mode used for probing (Fig. 2-2). The uniform atom-probe coupling g in Eq. 2.1 is therefore replaced by an atom-dependent value g_i. Correspondingly, the ith atom shifts the cavity mode by $\pm\Omega_i \equiv 2g_i^2/\Delta$ and experiences a differential light shift Ω_i per intracavity photon. In other words, the cavity mode couples to an asymmetrically weighted ensemble spin vector $\boldsymbol{\mathcal{S}}$ with $\mathcal{S}_z \propto \sum_{i=1}^{\mathcal{N}} \Omega_i \left[|\uparrow\rangle_i \langle\uparrow|_i - |\downarrow\rangle_i \langle\downarrow|_i \right]$, where I use $\mathcal{N}$ to denote the total number of atoms in an ensemble with non-uniform coupling. We normalize $\boldsymbol{\mathcal{S}} \equiv \Omega^{-1} \sum_{i=1}^{\mathcal{N}} \Omega_i \mathbf{s}_i$ in terms of an effective coupling Ω chosen to uphold the usual relation between spin length and variance, $\Delta\mathcal{S}_{\perp\text{CSS}}^2 = \mathcal{S}/2$, in a coherent spin state; this requires

$$\Omega = \frac{\sum_{i=1}^{\mathcal{N}} \Omega_i^2}{\sum_{i=1}^{\mathcal{N}} \Omega_i} \tag{2.4}$$

and results in an effective total spin

$$\mathcal{S} = \frac{1}{2} \frac{\left(\sum_{i=1}^{\mathcal{N}} \Omega_i\right)^2}{\sum_{i=1}^{\mathcal{N}} \Omega_i^2}. \tag{2.5}$$

We accordingly define the effective atom number $N = 2\mathcal{S}$. The description of the ensemble in terms of $\boldsymbol{\mathcal{S}}$ is sufficient for quantifying spin squeezing because we require only measurements of spin length and variance and comparison of these quantities to their values in a coherent spin state. We always measure the spin via the cavity and therefore always measure the appropriately weighted ensemble spin $\boldsymbol{\mathcal{S}}$.

In terms of $\boldsymbol{\mathcal{S}}$ and the effective interaction strength Ω, the Hamiltonian can be written as

$$H_{\text{sys}}/\hbar = \omega_c c^\dagger c + \Omega c^\dagger c \mathcal{S}_z + \omega S_z \tag{2.6}$$

where it should be emphasized that the middle term involves the asymmetrically weighted spin vector but the last term involves the symmetrically weighted one. The commutator between the two, $[\mathcal{S}_i, S_j] = i\hbar\epsilon_{ijk}\mathcal{S}_k$ (where ϵ_{ijk} is the Levi-Civita symbol), shows that the asymmetrically weighted spin $\boldsymbol{\mathcal{S}}$ transforms as an ordinary spin vector under the symmetric single-particle rotations generated by any S_j. Thus, the final term $\hbar\omega S_z$ in the Hamiltonian of Eq. 2.6 generates the usual precession of $\boldsymbol{\mathcal{S}}$ about the z-axis on an asymetrically weighted Bloch sphere; and similarly, microwaves that couple uniformly to all atoms generate the desired rotations of $\boldsymbol{\mathcal{S}}$. Note, however, that two asymmetrically weighted spin vectors do *not* obey the usual angular momentum commutation relations, i.e., $[\mathcal{S}_i, \mathcal{S}_j] \neq i\hbar\epsilon_{ijk}\mathcal{S}_k$. As we shall see in Sec. 2.4, the atom-light interaction term $\hbar\Omega c^\dagger c \mathcal{S}_z$ can therefore reduce the length of the spin vector $\boldsymbol{\mathcal{S}}$ in a system with non-uniform coupling, but this effect is largely reversible by spin echo.

Outside this chapter, I will not distinguish notationally between $\mathbf{S}$ and $\boldsymbol{\mathcal{S}}$. In the context of experiments, $\mathbf{S}$ will always refer to the asymmetrically weighted spin vector that couples to the cavity mode and that we thus measure, and S will denote its length, related to the effective atom number N by $S = N/2$. For our ensemble of atoms—effectively uniformly distributed along the probe mode, since the atomic cloud is much longer than the beat length between the trap and probe lattices—the effective atom number is related to the number of real atoms by $N/\mathcal{N} = 2/3$.

2.3 Quantifying the Atom-Resonator Coupling

The atom-light interaction in a cavity can be quantified very accurately, as the vacuum Rabi frequency $2g$—describing the coupling of the vacuum field in the cavity to a given atomic transition—depends only on the cavity mode volume V and on the known optical transition frequency ω_o and dipole matrix element d_o. In particular, for the simple case of a two-level atom situated on the cavity axis at an antinode of the standing-wave mode, one can conveniently express the coupling $g_0 = d_o\sqrt{\omega_o/(2\epsilon_0\hbar V)}$ [58] in terms of the excited-state linewidth $\Gamma = \omega_o^3 d_o^2/(3\pi\epsilon_0\hbar c^3)$ as

$$g_0^2 = 6\Gamma\omega_{\text{FSR}}/(\pi k^2 w^2). \tag{2.7}$$

Here, $k = \omega_o/c$ represents the wavenumber of the atomic transition, and I have expressed the mode volume $V = L\pi w^2/4$ in terms of the free spectral range $\omega_{\text{FSR}} = \pi c/L$ of the cavity of length L and the mode waist w. Both ω_{FSR} and w can be precisely and accurately determined from the cavity transmission spectrum (see Sec. 3.1 and Ref. [59]).

In a real, multi-level atom, Eq. 2.7 is still valid for the coupling g_0 on a cycling transition. Generically, however, one must take into account polarization-dependent couplings between each of the two pseudo-spin states and various excited states. The atom-cavity interaction can then be quantified in terms of the differential light shift Ω_a between the

two relevant ground states $|\uparrow\rangle,|\downarrow\rangle$ in an atom at an antinode per intracavity photon, calculated by summing contributions from all relevant excited states. Our experiments use ^{87}Rb atoms, where for states $|\uparrow\rangle = |F = 2, m_F = 0\rangle$ and $|\downarrow\rangle = |F = 1, m_F = 0\rangle$ probed with linear polarization on the D_2 line, the result takes the form

$$\Omega_a = f g_0^2 \left(\frac{1}{\Delta_2} - \frac{1}{\Delta_1} \right). \tag{2.8}$$

Here, $f = 2/3$ is the oscillator strength of the D_2 line and each Δ_F represents an effective detuning of the cavity mode from the $\left|5^2 S_{1/2}, F\right\rangle \rightarrow \left|5^2 P_{3/2}, F'\right\rangle$ transitions, appropriately averaged over excited hyperfine states F'. For example, with the cavity mode 3.18 GHz blue-detuned from the $F = 2 \rightarrow F' = 3$ transition one obtains equal and opposite effective detunings $\Delta_F = \pm 2\pi \times 3.29$ GHz. Our cavity parameters (Tab. 3.1) yield $g_0 = 2\pi \times 557(6)$ kHz, resulting in an antinode differential light shift of $\Omega_a = 2\pi \times 126$ Hz per intracavity photon. We choose this configuration for the probing scheme that will be introduced in Fig. 3.4(b) and used for cavity feedback squeezing.

In terms of Ω_a, an atom at an arbitrary position $\mathbf{r}$ experiences a differential light shift $\Omega_a h^2(\mathbf{r})$ due to a single photon in a TEM$_{00}$ mode, where $h(\mathbf{r}) = e^{-(x^2+z^2)/w^2} \sin(ky)$ represents the mode amplitude. The same quantity $\Omega_a h^2(\mathbf{r})$ also represents the shift in the cavity mode frequency associated with a change in the atom's hyperfine state. Thus, for our extended sample of atoms uniformly distributed over the standing-wave mode, we calculate the mode shift per unit effective spin as

$$\Omega = \Omega_a \left\langle h^4 \right\rangle / \left\langle h^2 \right\rangle, \tag{2.9}$$

where

$$\frac{\left\langle h^4 \right\rangle}{\left\langle h^2 \right\rangle} = \frac{\left\langle \sin^4 ky \right\rangle}{\left\langle \sin^2 ky \right\rangle} \frac{w^2 + 4\sigma_r^2}{w^2 + 8\sigma_r^2} \tag{2.10}$$

in terms of the radial cloud size $\sigma_r \ll w$. In the limit where the atoms are radially cold ($\sigma_r = 0$), the axial average yields $\left\langle h^4 \right\rangle / \left\langle h^2 \right\rangle = 3/4$. For our typical radial cloud size $\sigma_r = 7(1)$ μm, small compared to the $w = 57$ μm mode waist, this value is reduced to $\left\langle h^4 \right\rangle / \left\langle h^2 \right\rangle = 0.71(1)$.

2.4 Verifying the Atom-Resonator Coupling

We verify our quantitative understanding of the atom-resonator coupling by directly measuring the differential ac Stark shift Ω_a per intracavity photon, with the cavity 3.57 GHz blue-detuned from the $F = 2 \rightarrow F' = 3$ transition. The measurement is performed using a Ramsey sequence in which we apply a pulse of probe light during the precession time. In particular, we prepare a coherent spin state along $\hat{x}$, apply a pulse of probe light with variable intensity, then perform a final $\pi/2$ rotation that converts $\mathcal{S}_x \rightarrow \mathcal{S}_z$ and measure $\mathcal{S}_z$,

thereby deducing the phase that was imparted by the probe. The result is plotted in Fig. 2-3 as a function of the number of transmitted probe photons p.

To compare the observed phase evolution with theory, we use Eq. 2.6 to predict that the jth atom's phase should evolve—in a frame rotating at ω—according to

$$\frac{ds_+^j}{dt} = \frac{i}{\hbar}\Omega\left[\mathcal{S}_z, s_+^j\right] = i\Omega_j s_+^j c^\dagger c. \tag{2.11}$$

Replacing the intracavity photon number $c^\dagger c$, in a semiclassical approach, by the c-number n_c (see Sec. 6.1 for a more rigorous treatment), we find that $\left\langle s_+^j(t)\right\rangle = e^{i\Omega_j n_c t}$. The number of photons transmitted during the time t is related to the intracavity photon number n_c by $p = n_c(\kappa/2)t$, since photons leave through each mirror at a rate $\kappa/2$. The phase shift of an antinode atom per transmitted photon is thus given by $\varphi_a = \Omega_a n_c t/p = 2\Omega_a/\kappa$. For an ensemble of atoms uniformly distributed along the cavity axis, the x-component of the ensemble spin after p photons have been transmitted is then

$$\langle\mathcal{S}_x\rangle \propto \frac{\int_0^{2\pi} \sin^2(ky)\cos(p\varphi_a\sin^2(ky))\,dy}{\int_0^{2\pi}\sin^2(ky)\,dy} = J_0(u)\cos(u) - J_1(u)\sin(u), \tag{2.12}$$

where the J_n are Bessel functions of the first kind and $u = p\varphi_a/2$. Figure 2-3 shows a fit of this form, from which we extract $\varphi_a = 230(20)$ μrad. A fit to a full numerical model including the radial cloud size yields $\varphi_a^{\text{meas}} = 250(20)$ μrad, in excellent agreement with the value $\varphi_a^{\text{calc}} = 2\Omega_a/\kappa = 253(8)$ μrad calculated from Eqs. 2.7-2.8 and our cavity parameters.

The decay in the length of the spin vector in Fig. 2-3 is due to the inhomogeneity of the atom-probe coupling and can be reversed by a spin echo technique, which is described in detail in Sec. 4.4. Briefly, instead of applying a single probe pulse, we apply two such pulses separated by a π microwave rotation. The average phase shift imparted to each atom in the first probe pulse is reversed during the second probe pulse, but each pulse individually still carries the information about the atomic state $\mathcal{S}_z$ that is required to produce squeezing. The green solid squares in Fig. 2-3 show the final value of $\langle\mathcal{S}_x\rangle/\mathcal{S}$ after the two probe pulses. The contrast $|\langle\mathcal{S}_x\rangle|/\mathcal{S}$ is largely restored, decreasing only slightly due to effects of atomic motion (see Sec. 4.4).

2.5 Scattering and Cooperativity

A fundamental limitation to any light-induced squeezing scheme is scattering into modes other than the single probe mode. We have so far neglected such spontaneous scattering, having eliminated the excited state from our model in Sec. 2.1 to obtain an effective Hamiltonian describing a frequency shift of the probe mode by atoms in the two ground states. Physically, this frequency shift arises from forward-scattering by the atoms into the cavity mode: light in the cavity acquires a phase shift via interference with the forward-

30
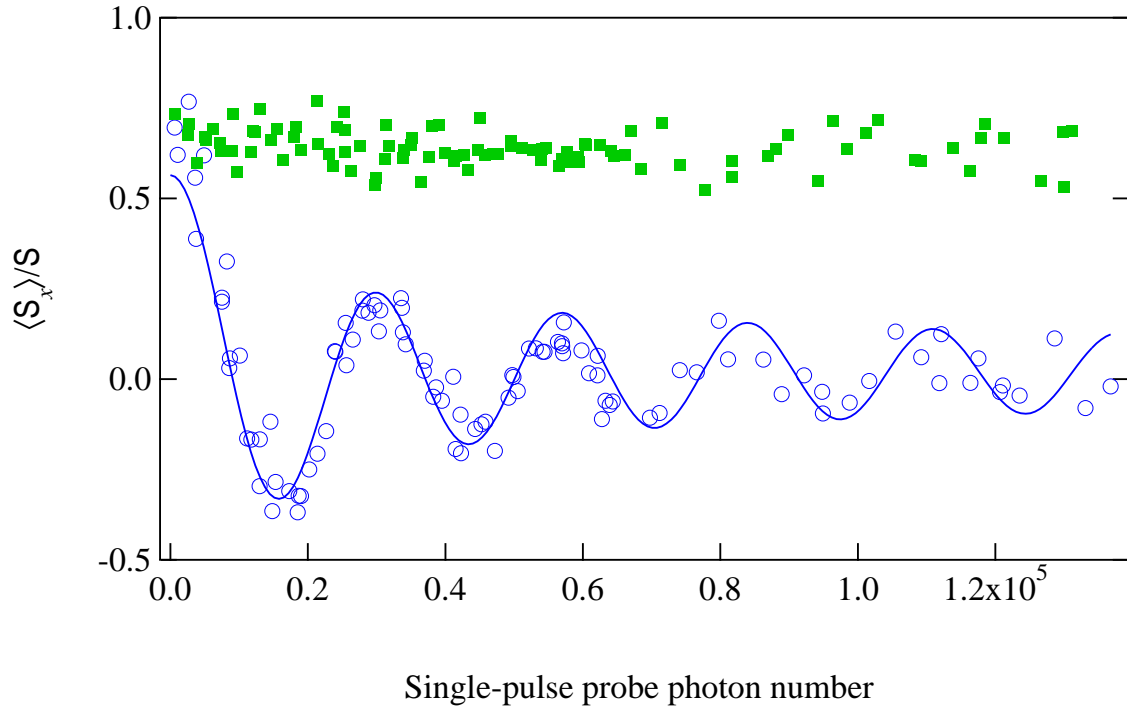
Figure 2-3: Verification of the atom-photon interaction via a Ramsey measurement (blue open circles) of the differential ac Stark shift, as described in the text. The blue curve is fit to the data using the model in Eq. 2.12, yielding $\varphi_a = 230(20)$ μrad. The decay in contrast is due to the inhomogeneity of the coupling and can largely be reversed (green solid squares) by spin echo.

scattered field. Thus, scattering is indispensable to light-induced squeezing; indeed, we shall see in Chs. 5 and 6 that the number of photons scattered into the cavity determines the factor by which the probe light can reduce spin noise. The essential forward-scattering is necessarily accompanied by detrimental free-space scattering, which can reveal or change the states of individual atoms, thereby causing decoherence [60,61] and reintroducing spin noise. Thus, fundamental limits to light-induced squeezing [55,56] depend on the ratio of photons scattered into the cavity to photons scattered into free space: the cooperativity [62,63].

The cooperativity η of a single atom in a cavity depends only on the geometry of the cavity mode. A Gaussian mode of wavenumber k and waist w subtends a solid angle $\Omega_c = 4\pi \times 4/(k^2 w^2)$ [59]. Multiplying $\Omega_c/(4\pi)$ by the cavity enhancement factor $4\mathcal{F}/\pi$ at an antinode, where $\mathcal{F}$ is the finesse, yields the cavity-to-free-space scattering ratio averaged over all polarizations. For an atom driven with either of the two polarizations supported by the cavity, however, the scattering into the cavity is enhanced by an additional factor of $3/2$ relative to that into free space, resulting in a maximum cooperativity

$$\eta_0 = \frac{24\mathcal{F}}{\pi k^2 w^2}. \tag{2.13}$$

The cooperativity can alternatively be expressed in terms of characteristic frequencies g, κ and Γ. In the weak-coupling limit $\eta < 1$, this can readily be seen from Fermi's golden rule: the rate at which an excited atom emits into a resonant cavity is $4g^2/\kappa$, and comparing this to the free-space scattering rate Γ results in an expression

$$\eta = \frac{4g^2}{\kappa\Gamma} \tag{2.14}$$

of the cooperativity as an interaction-to-decay ratio [63]. By evaluating this expression with $g = g_0$ as given by equation 2.7, one can verify the equivalence of Eqs. 2.13 and 2.14.

In addition to describing the probability for an excited atom to emit into the cavity, η_0 also quantifies the probability of the reverse process, namely that a resonant photon sent through the cavity excites the atom. This can be seen by taking the atomic cross section $6\pi/k^2$, dividing it by the effective area $\pi w^2/2$ of the cavity mode, and multiplying the resulting single-pass optical depth by the cavity enhancement factor $4\mathcal{F}/\pi$. One obtains twice the value in equation 2.13, i.e., the cavity-enhanced resonant optical depth of a single atom at an antinode is given by $2\eta_0$. This optical depth can also be understood from a Fermi's golden rule argument. The rate dp/dt at which photons leave a two-sided cavity in the forward direction is related to the intracavity photon number n_c by $dp/dt = n_c\kappa/2$. Comparing the absorption rate $4n_c g^2/\Gamma$ to the transmission rate and applying Eq. 2.14 confirms the optical depth 2η on cavity resonance.

In an ensemble, the cooperativity is collectively enhanced, since all atoms (in the same state) scatter into the cavity in phase to produce a power that scales as N^2, whereas the power scattered into free space scales only as N. Thus, the figure of merit relevant

to squeezing is the *collective cooperativity* $N\eta$, or equivalently the resonant optical depth $\mathrm{OD} = 2N\eta$ of the ensemble [55, 56]. The latter parametrization enables comparison with free-space squeezing schemes [7], where achieving the requisite optical depth $\mathrm{OD} \gg 1$ is a significant challenge [7, 64].

To more specifically quantify the destructive effect of free-space scattering relative to the desired effect of the atom-light interaction, it is useful to express the dimensionless parameter $\varphi \equiv 2\Omega/\kappa$ characterizing the latter in terms of the cooperativity:

$$\varphi = \frac{\eta\Gamma}{2}\left(\frac{1}{\Delta_2} - \frac{1}{\Delta_1}\right), \tag{2.15}$$

where $\eta = f\eta_0 \langle h^4 \rangle / \langle h^2 \rangle$ for an extended ensemble. Since φ represents the cavity mode shift (in half-linewidths) associated with changing an atom's state, it is a measure of how much information about the atomic state is carried by each photon, and it will govern the rate at which squeezing can occur. For comparison, since 2η represents the resonant optical depth on a cycling transition, the scattering rate per effective atom in state F is related to the rate dp/dt of photon transmission by

$$\Gamma_{\mathrm{sc}} = 2\eta\left(\frac{\Gamma}{2\Delta_F}\right)^2 \frac{dp}{dt}. \tag{2.16}$$

Returning to the simplifying assumption (or approximation) of equal and opposite detunings $\Delta_2 = -\Delta_1 \equiv \Delta$, we obtain the relation

$$\varphi^2 dp/dt = 2\eta\Gamma_{\mathrm{sc}}, \tag{2.17}$$

We apply this relation in Chs. 5 and 6 to calculate fundamental limits to squeezing.

Chapter 3

Experimental Setup

To set the stage for presenting the experiments forming the main body of this thesis, I now proceed to describe the apparatus used throughout. We achieve the strong collective atom-light coupling required for spin squeezing by placing our ^{87}Rb atoms into an optical resonator. I describe the physical parameters of the resonator in Sec. 3.1. We optically trap the atoms in a dipole trap in the cavity mode, so that the atoms are transversely well confined within the mode of the squeezing light. Details of the trapping and cooling of the atoms are provided in Sec. 3.2. To maximize the atomic coherence time in the trap, we engineer a cancellation of the vector and scalar light shifts, as explained in Sec. 3.3. Section 3.4 introduces the probe laser and the scheme for locking it to the cavity, while Sec. 3.5 presents the microwave system utilized for coherent rotations of the ensemble spin state. A diagram of all fields relevant to trapping, cooling, manipulating, and probing the atoms in the cavity is provided in Fig. 3-1.

3.1 Optical Resonator

The design and construction of our symmetric, near-confocal Fabry-Perot cavity (see Fig. 3-2) are described in detail in the thesis of Igor Teper [65]. The geometrical parameters of the optical resonator can be determined very precisely from the cavity transmission spectrum [59], allowing an equally precise determination of the atom-cavity coupling g_0 (Eq. 2.7). In particular, the free spectral range $\omega_{\mathrm{FSR}} = \pi c / L$ indicates the length L of the cavity, and the transverse mode spacing indicates the deviation from confocality, from which we can establish the mirror curvature and the mode waist w. The spectroscopically determined values are listed in Tab. 3.1.

The cavity linewidth κ can also be measured from the transmission spectrum, given a probe laser much narrower than κ. Alternatively, the linewidth can be measured by a ring-down measurement [12], given a photodiode with bandwidth $\gg \kappa$ and a sufficiently fast switch-off of the incident light. Failing these conditions, a transmission spectrum would overestimate the linewidth, whereas a ring-down measurement would underestimate it.
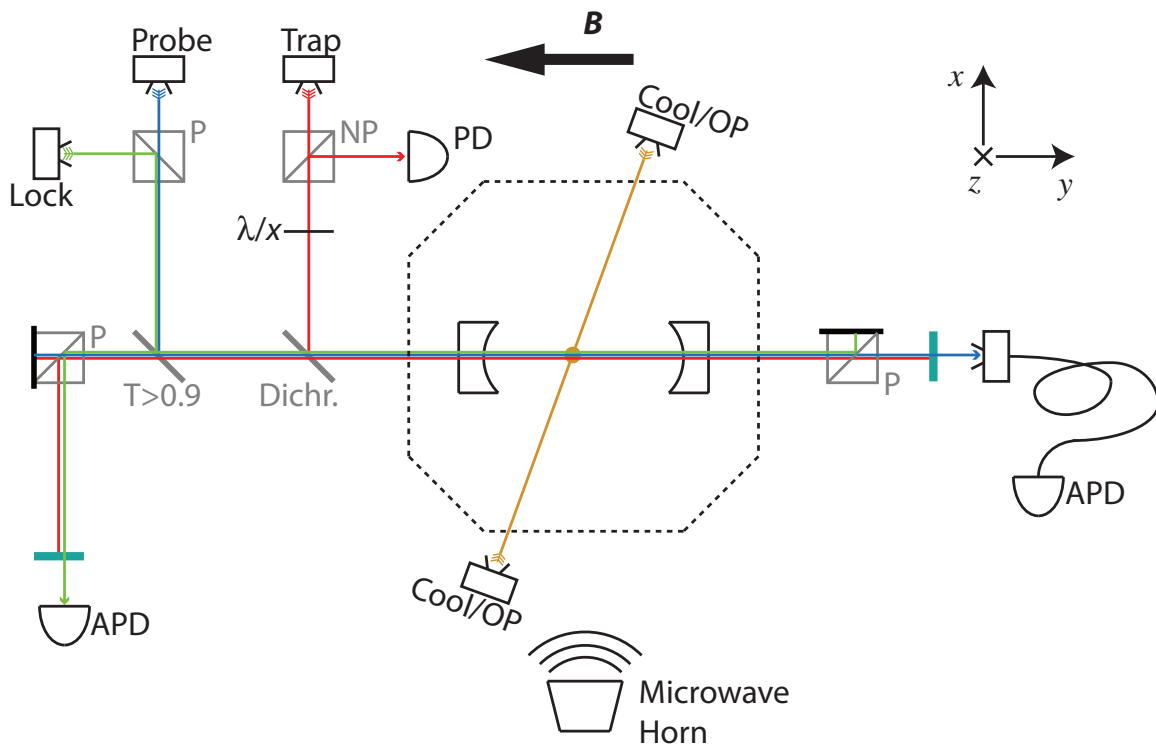
Figure 3-1: Experimental setup for atom trapping, cooling, state preparation, and probing, viewed from above. P and NP indicate polarizing and non-polarizing beamsplitters. (A)PD indicates (avalanche) photodiode. A partial reflector with $> 90\%$ transmission ($T > 0.9$) permits detection of the reflected locking light. A dichroic mirror (dichr.) combines the 780 nm probe/lock light (further described in Sec. 3.4) with the 851 nm trap light (Sec. 3.2). The polarization of the trap light is controlled by a variable retarder (λ/x). A pair of counterpropagating beams in the xy plane (Cool/OP), and a third beam from below, are used for optical pumping and polarization gradient cooling. For magic-polarization trapping (Sec. 3.3), a uniform magnetic field $\mathbf{B}$ is aligned with the cavity axis. Microwaves (Sec. 3.5) are used to drive the ^{87}Rb clock transition.

Parameter		$\lambda = 780$ nm	$\lambda = 851$ nm
Free spectral range[1]	$\omega_{\mathrm{FSR}}/(2\pi)$	5632(1) MHz	
Transverse mode spacing	$\omega_{\mathrm{t}}/(2\pi)$	226.3(3) MHz	
Mirror separation	L	26.62(1) mm	
Mirror curvature radius	R	25.04(2) mm	
Mode waist	w_λ	$56.9(4)\mu$m	$59.5(5)\mu$m
Linewidth	$\kappa_\lambda/(2\pi)$	1.01(3) MHz	135(2) kHz
Finesse	$\mathcal{F}_\lambda$	$5.6(2) \times 10^3$	$4.2(1) \times 10^4$
Antinode cooperativity	$\eta_{0,\lambda}$	0.203(7)	1.65(4)

Table 3.1: Resonator parameters. The mode waists are calculated at the position of the atoms, 2.6(5) mm from cavity center. Outside this table, all resonator values refer to the probe wavelength $\lambda = 780$ nm unless otherwise specified.

However, we are able to meet the conditions for either measurement of the linewidth κ_{780} at the 780-nm wavelength of the D_2 line by probing the cavity with a sideband (see Sec. 3.4) modulated at ~ 14 GHz onto a laser that is narrowed by a high-bandwidth lock to the cavity (see App. A). Changing the modulation frequency allows us to step the sideband across the cavity resonance to directly measure the lineshape via the transmitted intensity. Alternatively, the sideband can simply be placed on cavity resonance and then rapidly switched off—by switching the RF modulation—and the decaying cavity transmission detected on a fast photodiode. We find excellent agreement between the linewidth $\kappa_{780}^t = 2\pi \times 1.012(3)$ MHz measured in transmission and the value $\kappa_{780}^r = 2\pi \times 1.01(3)$ MHz inferred from the ringdown lifetime $1/\kappa_{780}^r$. From a similar ring-down measurement, we have also measured the cavity linewidth at the 851 nm wavelength of our dipole trap.

The many parameters describing our resonator—at each wavelength λ—can be distilled into a single figure of merit, the *cooperativity* derived in Sec. 2.5:

$$\eta_{0,\lambda} \equiv \frac{24\mathcal{F}_\lambda}{\pi k^2 w^2}, \qquad (3.1)$$

where $k = 2\pi/\lambda$. This dimensionless parameter quantifies the interaction of a single atom with the cavity mode by comparing the mode's transverse confinement $\propto w^2$ with the atomic cross section $\propto 1/k^2$ and accounting for the cavity enhancement factor—i.e., the ratio of intracavity to incident intensity—of $4\mathcal{F}_\lambda/\pi$ at an antinode. Here, $\mathcal{F}_\lambda = \omega_{\mathrm{FSR}}/\kappa_\lambda$ is the cavity finesse at the relevant wavelength. Table 3.1 includes this and all other cavity parameters, at both 780 nm and 851 nm.

---

[1]We can easily measure the free spectral range with a fractional uncertainty $< 10^{-5}$, but the cavity length varies by $\sim 2 \times 10^{-4}$ in our experiments due to heating of the cavity induced by a nearby microchip (see Fig. 3-2).
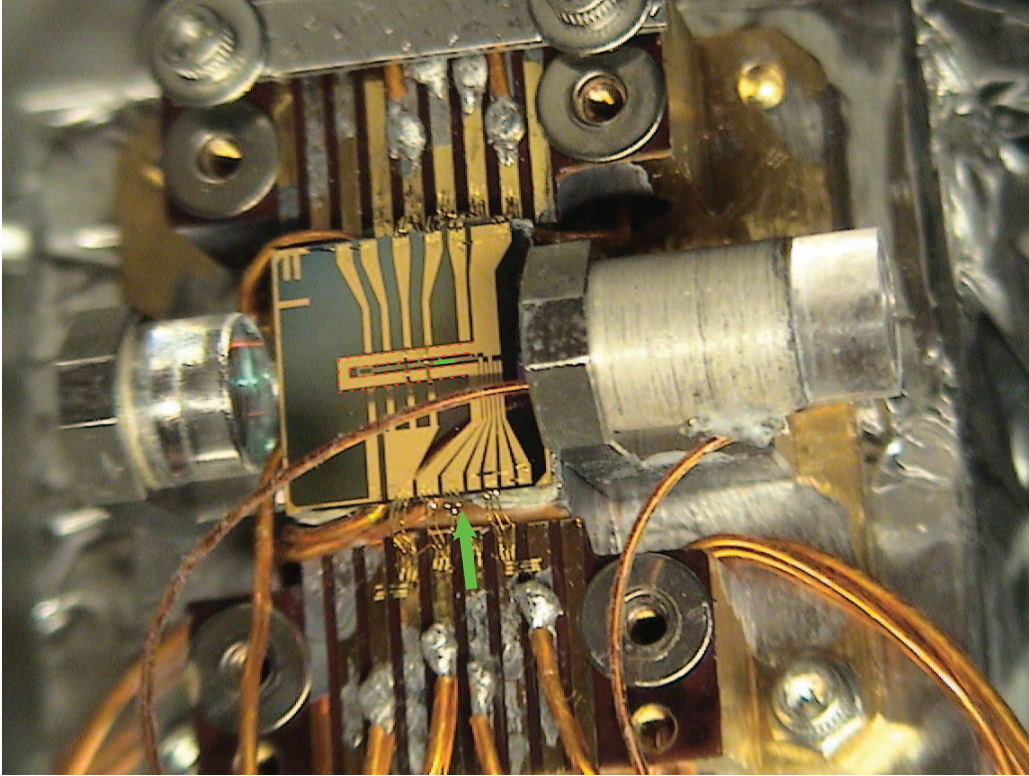
Figure 3-2: Microfabricated chip and optical resonator. The coil highlighted with dotted red lines forms a quadrupole trap in the cavity mode; the precise position of the trap minimum is adjusted by bias fields formed by macroscopic coils (not pictured). The green line indicates the approximate length and position of the atomic cloud, and the green arrow indicates the perspective of a camera used to record the images in Fig. 3-3.

3.2 Cooling and Trapping

Our experiments begin by loading a three-beam, retro-reflected magneto-optical trap (MOT) with ^{87}Rb atoms. The source of atoms is a dispenser that uses a non-evaporable getter as a reducing agent to release atomic ^{87}Rb from a rubidium salt [66]. After loading the MOT, we optically pump the atoms into the low-field-seeking $|F = 2, m_F = 2\rangle$ state using circularly polarized 780-nm light resonant with the $F = 2 \rightarrow F' = 3$ transition. The atoms are thus magnetically trapped in a quadrupole field and can be transported by moving the quadrupole field minimum by adjusting bias fields.

We transport the atoms into the mode of the optical resonator, which is situated 200 μm below a microfabricated chip [65, 67, 68] that has been described in detail in the thesis of Yu-ju Lin [67]. We compress the atomic cloud into a quadrupole trap formed by a U-shaped coil on the chip to facilitate its loading into a standing-wave dipole trap formed by 851-nm light in the cavity mode. Fig. 3-2 shows the microchip and cavity and indicates the axial position of the atomic cloud, while Fig. 3-3 presents absorption images of the atomic cloud before and after loading into the optical dipole trap.
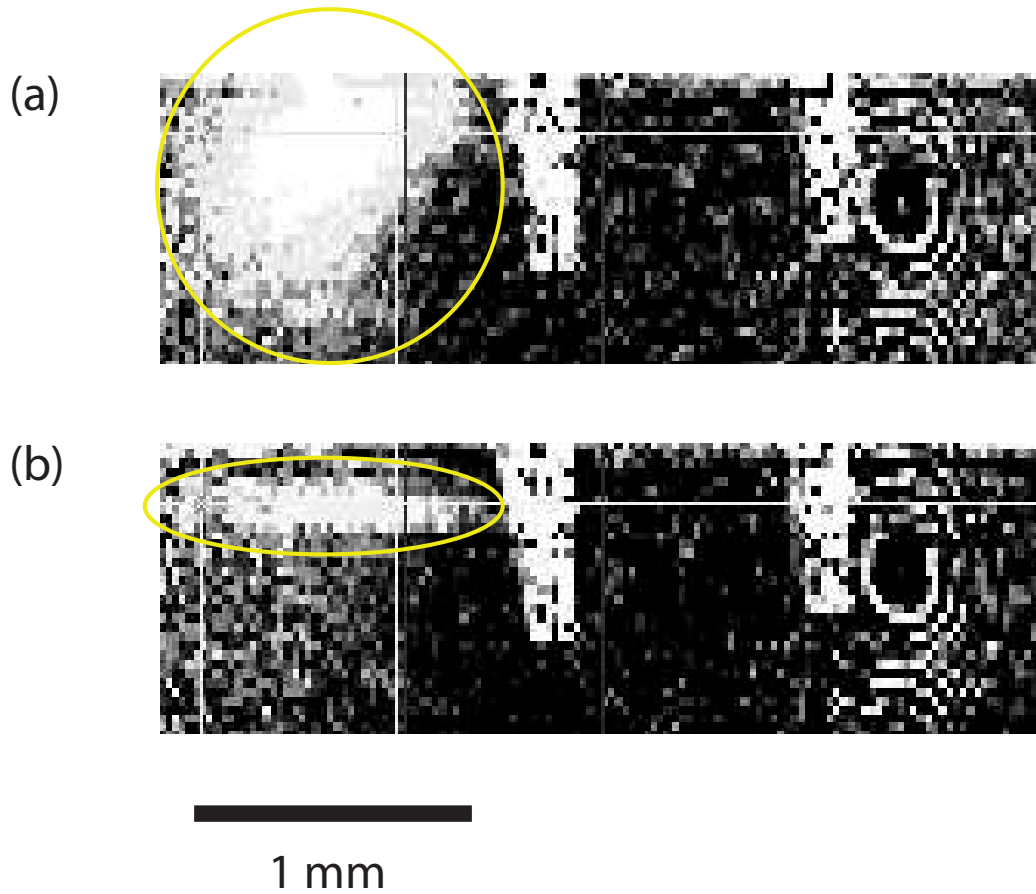
Figure 3-3: Absorption images of atomic cloud, circled in yellow: (a) in quadrupole trap; (b) after loading into optical dipole trap in cavity mode. The upper edge of each image corresponds to the microchip surface.

Optical dipole trap		Atomic cloud	
Axial frequency	480(40) kHz	Length	1 mm
Radial frequency	1.5(2) kHz	RMS radius	7(1) μm
Trap Depth	18(6) MHz	Radial temperature	1.0(4) MHz

Table 3.2: Typical characteristics of standing-wave dipole trap and atom cloud. The trap depth can be determined (consistently) either from a spectroscopic measurement of the axial trap frequency (as in Fig. 8-4); or from the radial trap frequency inferred from the optimal spin echo timing (see Sec. 4.4), combined with the known mode waist. The radial temperature measurement is described in Sec. 4.3.

Our cavity's high finesse $\mathcal{F}_{851} = 42000$ at the wavelength of the trap laser allows us to form a lattice up to ~ 100 MHz deep with < 20 mW of input power from a diode laser. However, all of the major experiments in this thesis are performed at the trap depth $U_0 = 2\pi \times 18(6)$ MHz. Table 3.2 summarizes the properties of the atomic cloud in the dipole trap of this depth. We reach a radial temperature of 1.0(4) MHz after 5 ms of polarization gradient cooling in a "gray molasses" [69]. In particular, operating at zero magnetic field, we apply two cooling beams counter-propagating in the xy-plane with lin $\perp$ lin polarizations and a third, circularly polarized cooling beam propagating along $-\hat{z}$ (upward); contributing to each cooling beam are two lasers, one blue-detuned from the $F = 2 \to F' = 2$ transition, the other blue-detuned from the $F = 1 \to F' = 1$ transition. The polarization gradient cooling requires degenerate Zeeman sublevels and therefore a linear polarization of the dipole trap. Following the cooling, we switch the trap polarization (using a variable retarder) to a "magic" elliptical polarization that maximizes the atomic coherence time in the trap (see Sec. 3.3). We typically allow ~ 100 ms for this retarder (and a magnetic field applied along $\hat{y}$) to settle before proceeding to preparation of internal atomic states (beginning with the optical pumping described in App. B).

The cavity-enhanced lattice places high demands on laser frequency stability, since any frequency noise converted to intensity noise at twice the axial trap frequency $\omega_{\mathrm{ax}} \approx 2\pi \times 500$ kHz can cause parametric heating [70]. The narrowing of the trap laser by a combination of passive optical feedback and high-bandwidth active feedback is described in App. A. We have measured a 540(50) ms lifetime in the trap for a 1 MHz trap frequency. (The standing wave can largely be canceled by modulating the trap laser at ω_{FSR} to add sidebands resonant with the two adjacent TEM$_{00}$ modes; this extends the lifetime to 7 s, consistent with lifetimes previously measured in a magnetic trap [65].)

3.3 Magic-Polarization Trap

To minimize inhomogeneous broadening of the clock transition, the trap light is elliptically polarized such that the vector light shift cancels, to lowest order, the differential scalar light

shift of the clock states. Such a cancellation is possible because the vector light shift acts as an effective magnetic field [71] and can be added to a real magnetic field to yield a quadratic Zeeman shift which, like the scalar light shift, is linear in the local intensity of trap light. In particular, in a magnetic field B_y along the resonator axis, for an atom at potential $U < 0$ in the dipole trap, the $|F = 1, m_F = 0\rangle \rightarrow |F = 2, m_F = 0\rangle$ transition frequency is shifted by

$$\frac{\delta_{\mathrm{HF}}(U)}{2\pi} = -\frac{\omega_{\mathrm{HF}}}{\Delta}\frac{U}{h} + \beta_{\mathrm{QZ}}\left(B_y + fb_{\sigma_+}\frac{U}{h}\right)^2, \qquad (3.2)$$

where $\omega_{\mathrm{HF}} = 2\pi \times 6.835$ GHz is the ground-state hyperfine splitting; $\Delta^{-1} = (2/\Delta_{D2} + 1/\Delta_{D1})/3$ in terms of the detunings Δ_{D1} and Δ_{D2} from the D_1 and D_2 lines; $\beta_{\mathrm{QZ}} = 575$ Hz/G^2 sets the scale of the quadratic Zeeman shift [13]; f is the circular polarization fraction of the trap light; and the coefficient $b_{\sigma_+} = (\Delta_{D1}^{-1} - \Delta_{D2}^{-1})\Delta \times h/3\mu_B = 0.061$ G/MHz gives the effective magnetic field per unit trap depth for σ_+-polarized light. For a given field B_y, the broadening is minimized by choosing f to place the minimum of the parabola described by Eq. 3.2 at the mean trapping potential $\langle U \rangle$ seen by the atoms. For $B_y^2 > (\omega_{\mathrm{HF}}/\Delta)\langle U \rangle/\beta_{\mathrm{QZ}}$, the optimum circular polarization f is inversely proportional to B_y, so that the residual broadening scales as $1/B_y^2$.

The polarization can be optimized experimentally by maximizing the coherence time of a Ramsey measurement. Fig. 3.3 shows the measured Ramsey coherence time at $B_y = 5.6$ G as a function of circular polarization fraction f. At an optimum circular polarization fraction $f = 0.5(1)$, in agreement with the value calculated to minimize Eq. 3.2 at our trap depth $-U \approx 18$ MHz, we measure a Ramsey coherence time of 10(2) ms. We have evidence that this coherence time is no longer limited by the trap.

A systematic study of this technique has since been carried out by Lundblad *et al.* [72], and improvements to it have been proposed by Chicireanu *et al.* [73].

3.4   Probing Scheme

Both measurement squeezing and squeezing by cavity feedback rely on a laser that sensitively probes frequency shifts of a particular cavity mode ("probe mode") due to the atoms' state-dependent index of refraction. We stabilize this probe laser relative to another cavity mode ("lock mode") that is much farther detuned from atomic resonance and thus negligibly affected by the atoms. We generate sidebands on the probe laser, both for the probing itself and for Pound-Drever-Hall frequency stabilization relative to the lock mode (see App. A), using broadband fiber-coupled electro-optic modulators (EOMs) manufactured by EOSPACE (model PM-0K5-10-PFA-PFA-780-UL). Figure 3.4 illustrates the frequencies of the probe laser carrier and the lock and probe sidebands relative to the cavity modes and atomic transition frequencies; shown are two different schemes, one used for squeezing by QND measurement (a), the second used in the subsequent experiments involving cavity
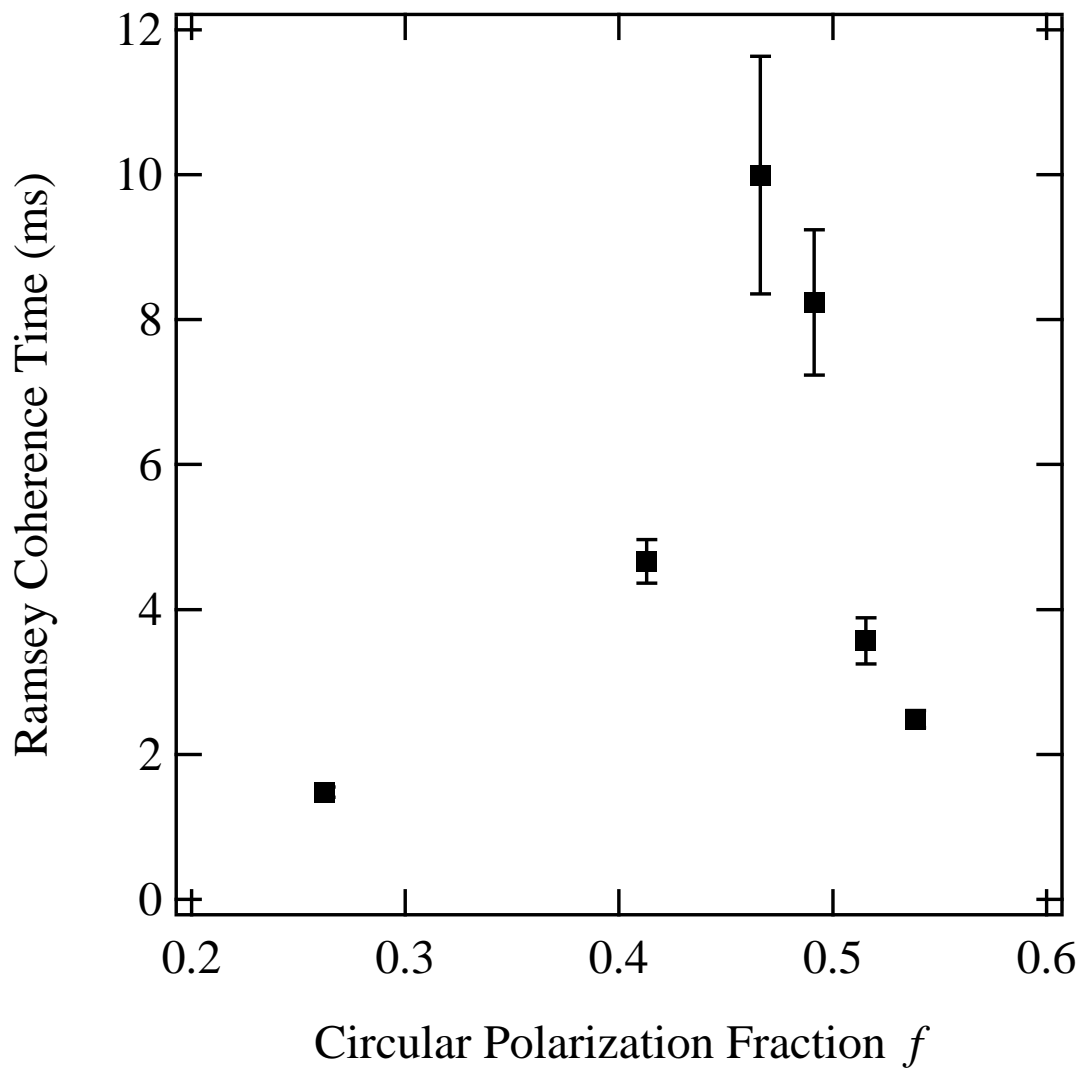
Figure 3-4: Ramsey coherence time in 851-nm optical dipole trap, showing a sharp maximum at the magic polarization fraction $f = 0.5(1)$ for the bias field $B_y = 5.6$ G and trap depth $U_0 \approx 2\pi \times 18$ MHz.

feedback squeezing (b).

In both schemes, the probe sideband is near-resonant with a TEM_{00} mode tuned roughly halfway between the $F = 1 \rightarrow F' = 2$ and $F = 2 \rightarrow F' = 3$ transitions of the ^{87}Rb D_2 line. In particular, the sideband is detuned by $\Delta \approx \kappa/2$ from this cavity resonance to maximize the dependence of transmitted intensity on atom-induced shifts of the resonance frequency. The lock sideband is placed on a TEM_{01} mode; this allows it to be spatially filtered from the probe light at the cavity output for detection. In addition, the node of the TEM_{01} mode on the cavity axis minimizes the atoms' exposure to the lock light. While this helps avert scattering-induced decoherence, we also rely on a large detuning $\delta_{lock} \geq 2\pi \times 10$ GHz of the lock mode from the $F = 2 \rightarrow F' = 3$ transition, especially to minimize inhomogeneous differential light shifts associated with the lock mode curvature and finite atomic temperature. The resonator length is stabilized via a beat note between the probe laser carrier and the reference laser [12].

Under certain conditions, measurement squeezing can benefit from a compensation scheme in which the probe sideband at detuning $+\delta$ from the probe mode is accompanied by a symmetric sideband at detuning $-\delta$ from an atom-insensitive TEM_{00} mode; this is accomplished by placing the laser carrier precisely halfway between two TEM_{00} modes. The total transmitted intensity from the probe and compensation sidebands is then insensitive to laser frequency jitter. As this insensitivity comes at the price of doubling the photon shot noise with compensation light that contributes no information about the atomic state, the compensation scheme is advantageous only if the probe sideband power is sufficiently high that frequency-noise-induced fluctuations in its transmission dominate over the photon shot noise. We applied this compensation sideband technique (Fig. 3.4(a)) in our measurement squeezing experiments in order to operate with minimal lock sideband power and maintain fixed performance relative to the photon shot noise limit over a wide range in probe power. The probe and compensation sidebands were separated by five cavity free spectral ranges ($5\omega_{FSR} = 2\pi \times 28.2$ GHz) and the lock sideband placed on the TEM_{01} mode nearest the laser carrier, at a detuning $\delta_{lock} = -2\pi \times 10.4$ GHz from the $F = 2 \rightarrow F' = 3$ transition.

Subsequent to the measurement squeezing experiments, we adopted the upgraded probing scheme shown in Fig. 3.4(b). This scheme places the lock sideband at an increased detuning $\delta_{lock} = 2\pi \times 33.3$ GHz from the $F = 2 \rightarrow F' = 3$ transition. We achieve the requisite 36.6-GHz phase modulation by applying to the EOM an RF input at $\nu_{RF} = 18.3$ GHz and using a second-order sideband. We dispense with the compensation sideband (which, not interacting with the atoms, has no benefit for cavity feedback squeezing; and, in the relevant parameter regime, has little impact on detection) by moving the probe carrier away from the halfway point between TEM_{00} modes.

We control the power in the probe sideband at $2\nu_{RF} = 36.6$ GHz by mixing the RF source at ν_{RF} with an intermediate-frequency (IF) signal at $\nu_{IF} = 90$ MHz. The mixer outputs signals at $\nu_{RF} \pm \nu_{IF}$ that interfere in the EOM to form sidebands at $2\nu_{RF}$, whose

power depends on the IF power (easily adjusted) but whose frequency is independent of $\nu_{\rm IF}$. We generate an optical beat note that represents the detuning of the probe sideband from the reference laser by sending the probe carrier and reference laser (separated by 34.6 GHz) together through a fiber-coupled electro-optic amplitude modulator driven with a portion of the same RF signal (at $\nu_{\rm RF} = 18.3$ GHz) used to generate the probe sideband.

The lock sideband can be switched off for short times during the experiment to preserve the phase coherence of the atomic state. The lock carrier is always on, with $\sim 10\ \mu$W power incident on the cavity at a detuning of 51 MHz from cavity resonance in the scheme of Fig. 3.4(b).

At the cavity output, the probe light is sent through a single-mode fiber to an avalanche photodiode (Hamamatsu model S3884) operating at a gain $M = 13$. The transmitted light is detected with an overall quantum efficiency $\mathcal{Q} = 0.5(1)$. The photodetection circuit consists of an op-amp current-to-voltage converter with a 10 MΩ first-stage transimpedance gain, resulting in a measured noise equivalent power of 12 fW/$\sqrt{\rm Hz}$, consistent with the calculated Johnson noise. Reaching this noise level requires careful matching of the op-amp input impedances, including the reactive component.

3.5   Microwave Setup

We use microwaves to address the ^{87}Rb hyperfine transition, at a frequency $\omega_{\rm HF} = 2\pi \times$ 6.83468 GHz [13]. We generate the frequency $\omega_{\rm HF}$ by mixing a stable 6.8 GHz phase-locked oscillator (Wentzel Associates)—referenced to a commercial (SRS) rubidium frequency standard—with an IF signal (at 35 MHz) output by a direct digital synthesizer (DDS; Analog Devices AD9959) whose frequency and phase are computer-controlled [12]. A voltage-variable attenuator adjusts the IF power. The frequency synthesis, switching, and amplification culminate in a microwave power of ~ 0.5 W at $\omega_{\rm HF}$ being broadcast toward the vacuum chamber by a 10 dBi microwave gain horn (HD Communications Corp.). We orient the horn so that it produces, at the position of the atoms, a magnetic field oscillating parallel to the static field $B\hat{y}$ (see Fig. 3-1) to maximize coupling to the $|F = 1, m_F = 0\rangle \rightarrow |F = 2, m_F = 0\rangle$ transition. We can thereby achieve a Rabi frequency as high as 12 kHz; however, we typically operate with an 8.3 kHz Rabi frequency chosen to produce a $\pi/2$ rotation in a conveniently round 30 μs.

We observe significant inhomogeneous broadening of the Rabi frequency, attributable to near-field effects of the microchip. The role of the chip is corroborated by measuring the coherence of Rabi oscillations as a function of the axial position of the atomic cloud. We choose the axial position that minimizes the Rabi broadening, ~ 3 mm from cavity center.
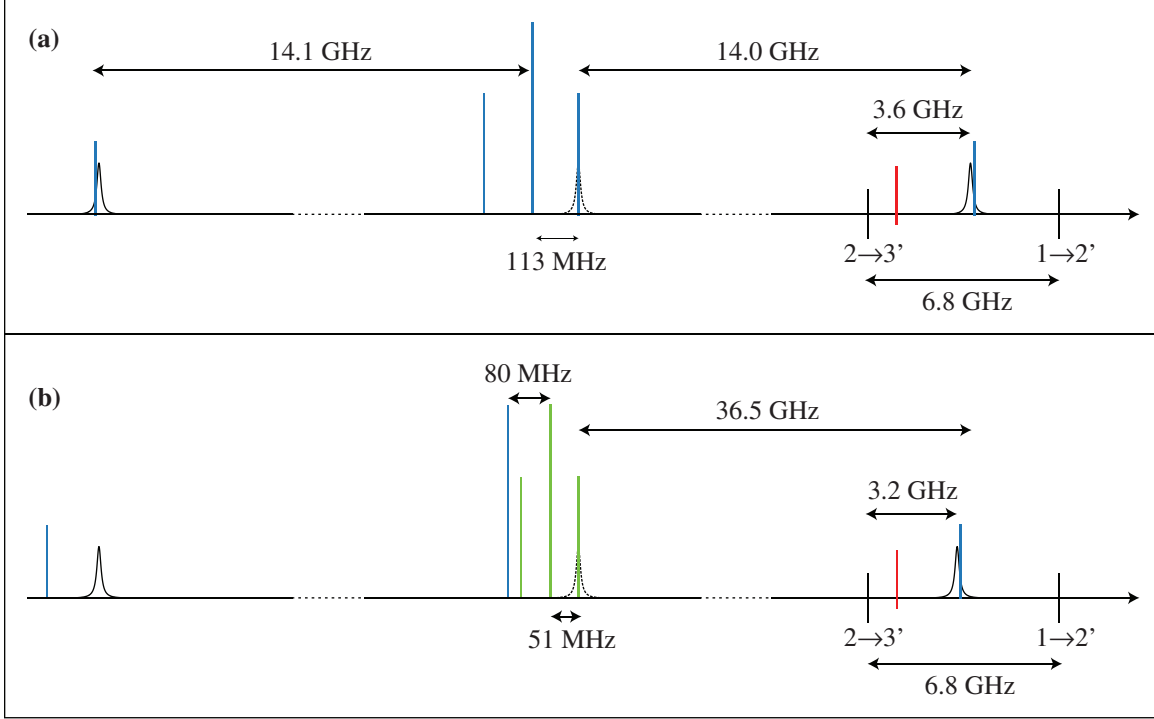
Figure 3-5: Frequency-domain diagram (not to scale) of probe and locking light relative to cavity and atomic resonances. Lorentzian profiles indicate TEM_{00} (solid) and TEM_{01} (dashed) modes. The TEM_{00} mode between the atomic resonances is used for probing, while the TEM_{01} mode is used for Pound-Drever-Hall stabilization of the probe laser (blue) to the cavity. A reference laser (red line) 1.13 GHz blue of the $F = 2 \rightarrow F' = 3$ transition is used for absolute frequency stabilization. (a) Scheme used for squeezing by QND measurement, with compensation sideband. (b) Scheme used for cavity feedback squeezing, with larger lock-probe detuning and without compensation sideband. In the latter scheme only, the probe (blue) and lock (green) light follow different optical paths, as illustrated in Fig. 3-1, to improve their respective mode-matching to the TEM_{00} and TEM_{01} modes; to avoid interference effects, the probe and lock are furthermore placed in orthogonal polarization modes and their carriers are separated by 80 MHz (via an AOM).

Chapter 4

Cavity-Aided Probing

Whereas many atomic physics experiments rely heavily on imaging, we instead obtain all our information about the atoms via a single cavity mode,[1] taking advantage of the shift of the cavity resonance by the atoms' state-dependent index of refraction. The cavity shift can be deduced from the resonator transmission (Sec. 4.1) and used to determine the total atom number (4.2), the radial temperature (Sec. 4.3), or the effective atom number in each hyperfine state. A typical time trace of the cavity transmission during various manipulations of the atoms is shown in Fig. 4-1.

For squeezing, be it by measurement or by cavity feedback, it is essential that information about the ensemble spin state be transferred to the light with the minimum possible disturbance of the atomic populations and coherences. Thus, much of this chapter will focus on the design of a minimally destructive probing scheme (Sec. 4.4) and the characterization of its performance (Sec. 4.5).

4.1 Cavity Transmission

We measure S_z via the resonator mode shift $\delta\omega_c = \Omega S_z$. There are several possible approaches to determining $\delta\omega_c$, using either the intensity or phase of either the transmitted or reflected light. We use the intensity of light transmitted by a probe laser tuned to the slope of the cavity resonance. As a function of S_z, the number of photons p transmitted by the cavity is related to the number of incident photons p_{in} by a Lorentzian function

$$p(S_z) = p_{\mathrm{in}} \left[1 + \frac{(\omega_L - \omega_c - \Omega S_z)^2}{(\kappa/2)^2} \right]^{-1}, \tag{4.1}$$

where ω_L is the frequency of the probe laser and ω_c the frequency of the cavity resonance for $S_z = 0$. The sensitivity of the transmission measurement to changes in S_z is maximized—at

---

[1]The sole exception is the absorption image shown in Fig. 3-3. Shortly after taking this image, we blocked the imaging beam with a microwave horn and never needed to use it again.
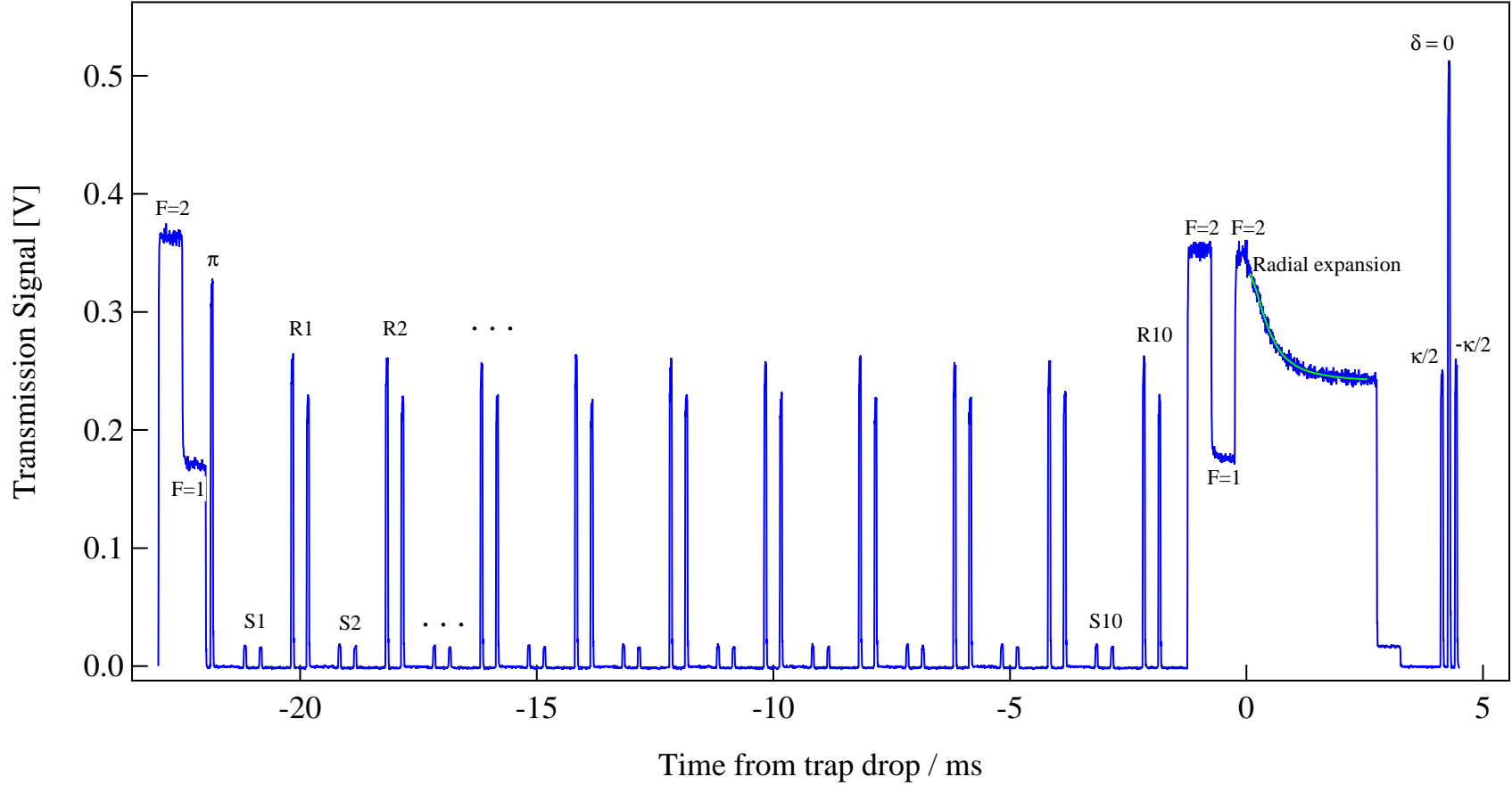
Figure 4-1: Typical trace of cavity transmission *vs.* time, obtained with the single-sideband probing scheme described in Sec. 3.4. Atoms are optically pumped into F=2 and F=1 to measure atom number. The light is briefly turned off to apply a π pulse, then pulsed back on to measure the resulting population transfer, which reflects both the optical pumping purity and the fidelity of the simple π pulse. Next, ten interations of cavity feedback squeezing at low probe intensity (S1...S10) and readout at high probe intensity (R1...R10) are performed. Afterwards, the atom number is measured again. Releasing the atoms from the trap and fitting the transmission measured during the radial expansion allows for determination of the radial temperature. Finally, the probe-cavity detuning $\delta \approx \kappa/2$ is verified by changing it in two steps of $-\kappa/2$ and comparing the observed transmission to the known Lorentzian lineshape.

fixed intracavity power—by placing the probe laser at the detuning $\delta \equiv \omega_L - \omega_c = \pm\kappa/2$ that maximizes the logarithmic slope $p^{-1}\left|dp/dS_z\right|_{S_z=0}$.

We always operate at sufficiently large probe-atom detuning that the mode shifts $\delta\omega_c \sim \Omega\sqrt{S/2}$ due to the CSS projection noise are much smaller than $\kappa/2$, so that the resonator transmission is linear in S_z for our measurements of spin noise. However, we use mode shifts as large as $\delta\omega_c = \Omega S \lesssim 1.7\kappa$ to measure total atom number and contrast. We therefore take into account the full Lorentzian lineshape in all measurements of S_z, using the same procedure for measuring projection noise, contrast, and total atom number.

4.2 Atom Number Measurement

At the beginning and/or end of each experiment cycle, we measure the effective atom number N. We determine the atom number by pumping all atoms first into $F = 2$, then into $F = 1$, and in each case measuring the resonator transmission. Although the resonator mode shifts $\delta\omega_c$ are linear in N, they are on the order of κ for our typical atom numbers, so that the transmitted power is a non-linear function of $\delta\omega_c$ which we must invert to obtain the atom number. To verify our determination of the resonator shift from the non-linear transmission signal, we additionally measure the average mode shift over several cycles of the experiment by finding the probe sideband frequencies $\omega_L^{(F)}$ that maximize the probe transmission when all atoms are pumped into hyperfine state F. By thus directly measuring the mode frequency shift, we obtain a linear measure of effective atom number $N^L = (\omega_L^{(2)} - \omega_L^{(1)})/\Omega$. In Figure 4-2 we plot N^L against the average atom number N extracted from the nonlinear transmission signal. The data are taken under the experimental conditions used for squeezing by measurement (Sec. 5.2), where $\Omega = 2\pi \times 88(3)$ Hz. The fit $N^L = 0.98(4)N$ with reduced $\chi^2 = 0.3$ indicates that the two measurements are in good agreement.

4.3 Radial Temperature Measurement

We measure the radial temperature T_r of the atomic ensemble by suddenly turning off the trap and observing the decaying atom-resonator coupling, manifest as a time-dependent cavity shift

$$\frac{\delta\omega_c(t)}{\delta\omega_c(0)} = \left(1 + \frac{4\Upsilon t^2}{mw^2}\right)^{-1}, \tag{4.2}$$

where m is the mass of ^{87}Rb, $w = 56.9(4)$ μm is the cavity mode waist at the position of the atoms, and Υ—which depends on both the temperature and the initial cloud size—can be expressed, given the trap depth U_0, as $\Upsilon = U_0 k_B T_r/(U_0 + k_B T_r)$. These equations assume that $k_B T_r \ll U_0$ so that the trap may be approximated as harmonic and the initial phase

49
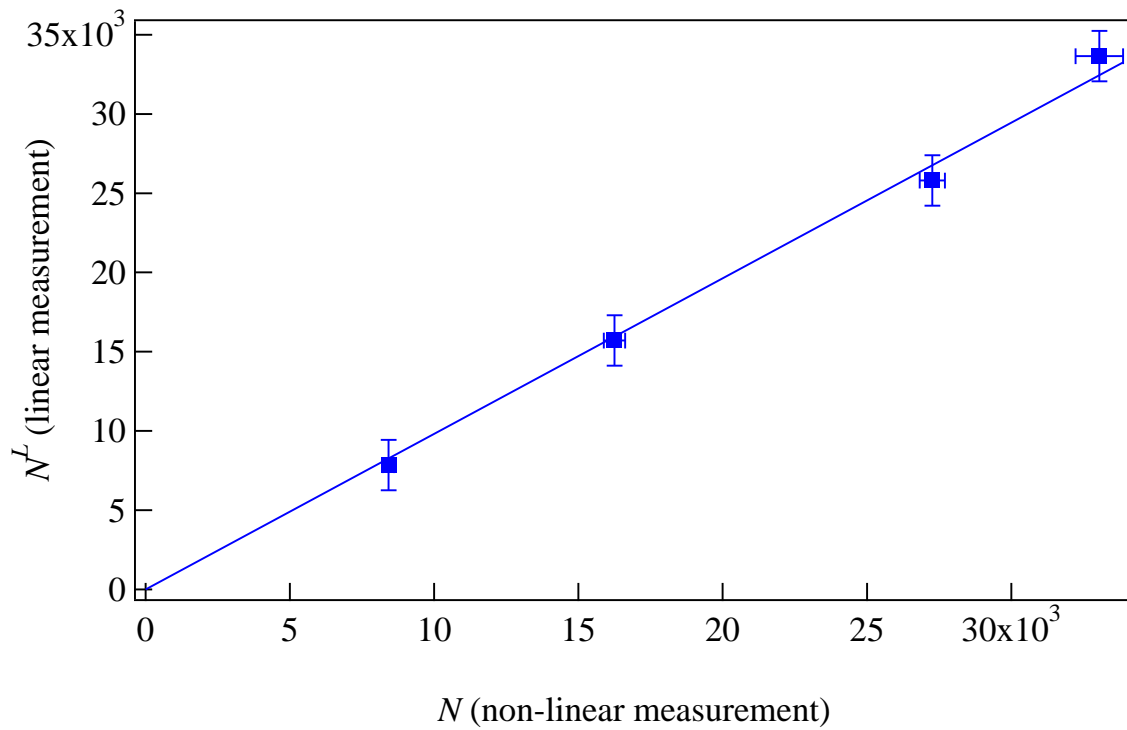
Figure 4-2: Comparison of two methods of determining effective atom number, as described in the text. The vertical error bars indicate the uncertainty in positioning the probe sideband on cavity resonance. The horizontal error bars arise because the atom number N is the average over a different set of loading cycles from those in which N^L is measured.

space distribution taken to be Gaussian. In this limit,

$$k_B T_r = \frac{\Upsilon}{1 - \Upsilon/U_0} \approx \Upsilon. \tag{4.3}$$

In the sample trace in Fig. 4-1, a fit (green curve) to the cavity transmission vs. expansion time t—accounting for the Lorentzian lineshape—yields $T_r = 0.8(1)$ MHz. Note that the same method provides consistent results for the radial temperature even for initial cavity shifts $\delta\omega_c(0) \gtrsim \kappa$.

4.4 Probing with Spin Echo

We apply a spin echo technique to minimize inhomogeneous dephasing due to the probe light. In particular, we always apply probe light in two pulses, in between which we apply microwaves to rotate all of the atomic pseudo-spins by π. This procedure ensures that the phase shift incurred by each atom during the first light pulse is, on average, canceled by the second light pulse. Two effects that can limit the effectiveness of this technique are atomic motion and imperfect microwave pulses. I discuss measures taken to mitigate these effects in Secs. 4.4.1-4.4.2 below, before describing in detail the determination of S_z from the two probe pulses.

4.4.1 Atomic Motion

The spin echo cancellation is degraded if atoms change their coupling to the probe light by moving between the two pulses. Thus, the entire sequence must be performed in one of the following ways: (i) fast compared to any atomic motion; (ii) slow enough to average over the atomic motion; or (iii) timed to match the periodicity of the atomic motion. In our system, the first option is immediately excluded by the 60 μs required to drive a π pulse. Instead, we use a probe pulse duration $\mathcal{T}_1 = 50$ μs that averages over the 500-kHz axial motion (and also optimizes technical noise of the measurement); and time the separation between pulses to match the 330-μs half-period of the radial motion. The pulse separation is optimized by measuring the contrast of a Ramsey-type measurement in which a spin-echo probing sequence with variable timing is inserted between the two $\pi/2$ pulses. Such a measurement constitutes our most precise determination of the radial trap frequency; subsequent to this one-time optimization of the spin-echo timing, we have periodically reoptimized the contrast after spin echo by varying the trap power, thereby recovering the intended trap frequency $\omega_r = \pi/(330\ \mu\text{s})$.

4.4.2 Pi Pulse Optimization

In order to perform a high-fidelity π rotation for the spin echo, we use a composite pulse sequence (SCROFULOUS [74–76]) that I shall denote $\tilde{\pi}$. The SCROFULOUS pulse $\tilde{\pi}_\phi =$

$\pi_{\phi-\pi/3}\pi_{\phi+\pi/3}\pi_{\phi-\pi/3}$ consists of three simple π pulses with phases indicated by the subscripts. I have chosen the phase convention so that in the limit where the simple π pulses have perfect fidelity, $\tilde{\pi}_\phi = \pi_\phi$. In the relevant case of imperfect simple π pulses, the SCROFULOUS pulse compensates for errors in Rabi frequency (or pulse length). Whereas our simple π pulses produce at best 90% inversion due to inhomogeneity in the Rabi frequency across the length of the atomic cloud (see Sec. 3.5), the composite $\tilde{\pi}$ pulses produce 98(1)% inversion. Note that the resonator locking light is always off during the microwave pulses and is turned back on 20 μs prior to the start of the second probe pulse.

While the SCROFULOUS pulse compensates for errors in Rabi frequency, it does not compensate (but rather augments) the effect of microwave detuning. For a Rabi frequency Ω_R, detuning the microwaves from resonance with the clock transition by an amount Δ_μ corresponds to tilting the axis of rotation on the Bloch sphere below the xy-plane by an angle Δ_μ/Ω_R for $\Delta_\mu \ll \Omega_R$. For an initial spin $\mathbf{S} = S\hat{x}$, a simple π rotation about $\hat{x}$ ($\phi = 0$) thus results in a frequency-dependent final z-projection $S_z = -2\Delta_\mu/\Omega_R$; the equivalent SCROFULOUS sequence doubles this dependence to $S_z = -4\Delta_\mu/\Omega_R$. However, for a π or $\tilde{\pi}$ pulse about $\hat{y}$ ($\phi = \pi/2$), the value of S_z is to lowest-order unaffected by the rotation, independent of detuning. Thus, we choose the phase $\phi = \pi/2$ to avoid converting fluctuations in the clock transition frequency into noise in the spin orientation. This choice of phase is particularly important at low photon rates, where the total phase shift per probe pulse is $\ll \pi$; at high photon rates, a large inhomogeneous phase shift after the first pulse effectively averages over all possible phases of the $\tilde{\pi}$ rotation and thus averages out any associated noise.

4.4.3 State Detection

To measure S_z, we use the information from both light pulses of the spin echo sequence.[2] In particular, our measurement M of S_z can be expressed as the average $M = (M_+ + M_-)/2$ of two single-pulse measurements $M_\pm = \pm\omega_\pm/\Omega$, where $\omega_\pm$ are the atom-induced shifts of the cavity mode determined from the probe transmission before and after the $\tilde{\pi}$ pulse. Here, we switch the sign convention for $S_z = \pm(N_\uparrow - N_\downarrow)/2$ at the $\tilde{\pi}$ rotation to compensate for the population exchange between states $|\uparrow\rangle$ and $|\downarrow\rangle$. Figure 4-3 illustrates two such two-pulse measurements, as used for squeezing by measurement and subsequent readout of the state thus prepared.

The spin echo approach has benefits for the measurement itself, not only for preserving coherence. Firstly, the spin echo measurement is insensitive to any fluctuations or drifts in laser intensity or laser-cavity detuning that are slow enough to be common to the two pulses $M_\pm$. Furthermore, whereas each individual pulse measures the population difference between the entire $F = 1$ and $F = 2$ hyperfine manifolds, the two-pulse measurement M

---

[2]Note that this differs from the method of Appel *et al.* [7], who apply two pulses to preserve coherence but use the measurement information from only the second pulse.
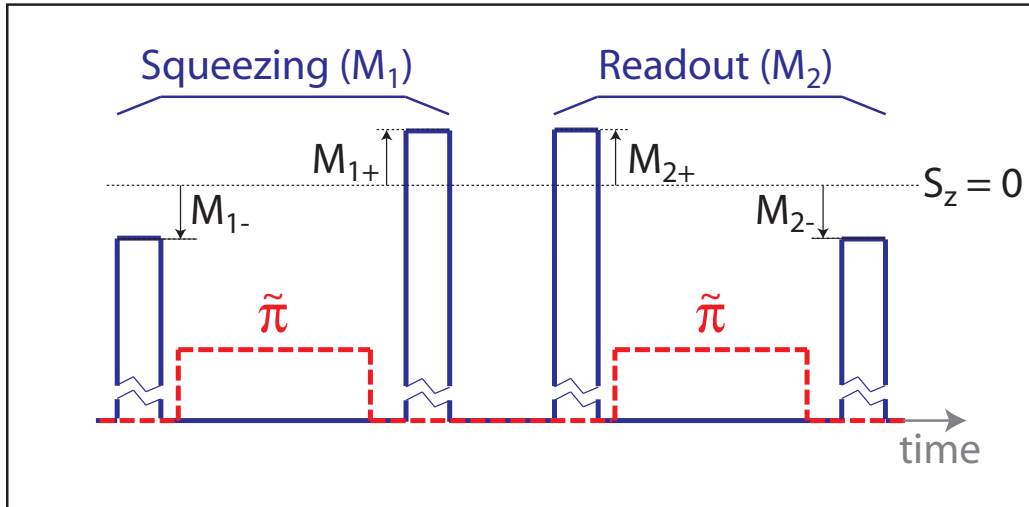
Figure 4-3: Measurements M_1 and M_2 of S_z for spin squeezing and readout. Each measurement is obtained from the probe light transmitted (solid blue line) in two pulses, before and after applying microwaves (dashed red line) to perform a $\tilde{\pi}$ rotation. Specifically, each measurement can be expressed as the average $M_i = (M_{i+} + M_{i-})/2$ of two single-pulse measurements $M_{i\pm} = \pm\delta\omega_{i\pm}/\Omega$, where $\delta\omega_{i\pm}$ are the atom-induced shifts of the cavity resonance deduced from the transmitted probe light. With each $\tilde{\pi}$ rotation, we switch the sign convention for $S_z = \pm(N_\uparrow - N_\downarrow)/2$ to compensate for the population exchange between states $|\uparrow\rangle$ and $|\downarrow\rangle$.

cancels any contribution from atoms not addressed by the $\tilde{\pi}$ pulse. Since the microwave Rabi frequency is small compared to the Zeeman splitting, this ensures that any atoms remaining outside the $m_F = 0$ clock states (due to imperfect optical pumping) are ignored. The spin echo sequence thus intrinsically probes precisely the variable S_z of interest. This feature can be exploited to achieve insensitivity to total atom number [77] in light-induced spin squeezing at any detuning, i.e., our special detuning yielding a mode shift $\omega \propto N_\uparrow - N_\downarrow$ is a technical convenience but not a requirement for either of the squeezing methods described in this thesis.

4.5   Measurement Sensitivity

For optimal light-induced squeezing, the probing must be conducted as close as possible to the photon shot noise limit. For deterministic squeezing by cavity feedback, this means specifically that the fluctuations in intracavity intensity should be dominated by photon shot noise. The requirement for conditional squeezing additionally encompasses detecting the transmitted light with high quantum efficiency and minimal technical noise. Even for deterministic squeezing, a sensitive spin measurement is essential to detecting the prepared states and thereby benefiting from the squeezing. Thus, a crucial step in any spin squeezing endeavor is a detailed evaluation and optimization of the measurement sensitivity.

To characterize the sensitivity of our spin measurement, we begin by evaluating its variance in the absence of atoms as a function of the transmitted probe photon number p. Figure 4-4 shows this atom-free measurement variance for probing either with (green) or without (black) a compensation sideband. Each is well described by a model

$$\Delta M^2{}_{\text{QND}} = b_{-2}p^{-2} + b_{-1}p^{-1} + b_0 p^0 \qquad (4.4)$$

allowing for three noise contributions: electronic noise of the detector scaling as $\Delta M^2 \propto p^{-2}$; photon shot noise and avalanche excess noise scaling as $\Delta M^2 \propto p^{-1}$; and laser frequency noise that is independent of photon number. We quantify these contributions as follows:

- **Photon shot noise and avalanche excess noise:** To calculate the photocurrent noise due to the probe and compensation light, we take into account both the shot noise of the light detected with a quantum efficiency $\mathcal{Q} = 0.43(4)$ and the excess noise factor $f_{\text{APD}} = 1.9(4)$ of the avalanche photodiode operated at a gain of 13 [78]. For probing with a single sideband, we obtain $b_{-1} = (f_{\text{APD}}/\mathcal{Q})(\kappa/2)^2/\Omega^2 = 1.4(3) \times 10^8$; the compensation sideband doubles b_{-1}.

- **Electronic noise:** From a fit to the noise measured in the absence of atoms (open green squares in Fig. 4-4) in which we constrain the coefficient b_{-1} to the value calculated above, we obtain an electronic noise contribution $b_{-2} = 1.5(3) \times 10^{13}$, most of which is attributable to the Johnson noise of the transimpedance gain resistor in the photodetection circuit.

- **Laser frequency jitter:** In the presence of the compensation sideband, the data are well fit by assuming no contribution from laser frequency jitter, $b_0 = 0$. Without the compensation sideband, based on the laser frequency fluctuations $S_\omega = 6(2) \times 10^{-10}(\kappa/2)^2/\text{Hz}$ (see App. A) in the frequency band of interest ($\sim 1 - 10$ kHz), we expect a contribution $b_0 = BS_\omega/\Omega^2 = 100(30)$, where $B = 1/(2T) = 5$ kHz is the bandwidth of the measurement. A fit to the black circles in Fig. 4-4 agrees, yielding $b_0 = 103(7)$.

In the ideal case where the measurement does not change the atomic state, $\Delta M^2{}_{\text{QND}}$ would represent the imprecision of our measurement of S_z. In reality, however, the measurement can change S_z via Raman scattering or infidelity of the microwave pulses used for the spin echo. While $\Delta M^2{}_{\text{QND}}$ dictates how precisely we can determine the *average* value of S_z over the course of the measurement, our ability to characterize a quantum state rests on our ability to determine S_z *at a specific point in time*. We quantify the imprecision of our spin measurement by performing two successive measurements M_1, M_2, in the presence of atoms initiated in a CSS with $\langle S_z \rangle = 0$, and evaluating $[\Delta M^2]_{S_z} \equiv \text{Var}(M_1 - M_2)/2$ to assess how well the two measurements agree. Provided that the measurements are identical and their noise is uncorrelated, this spin measurement variance reflects the imprecision of
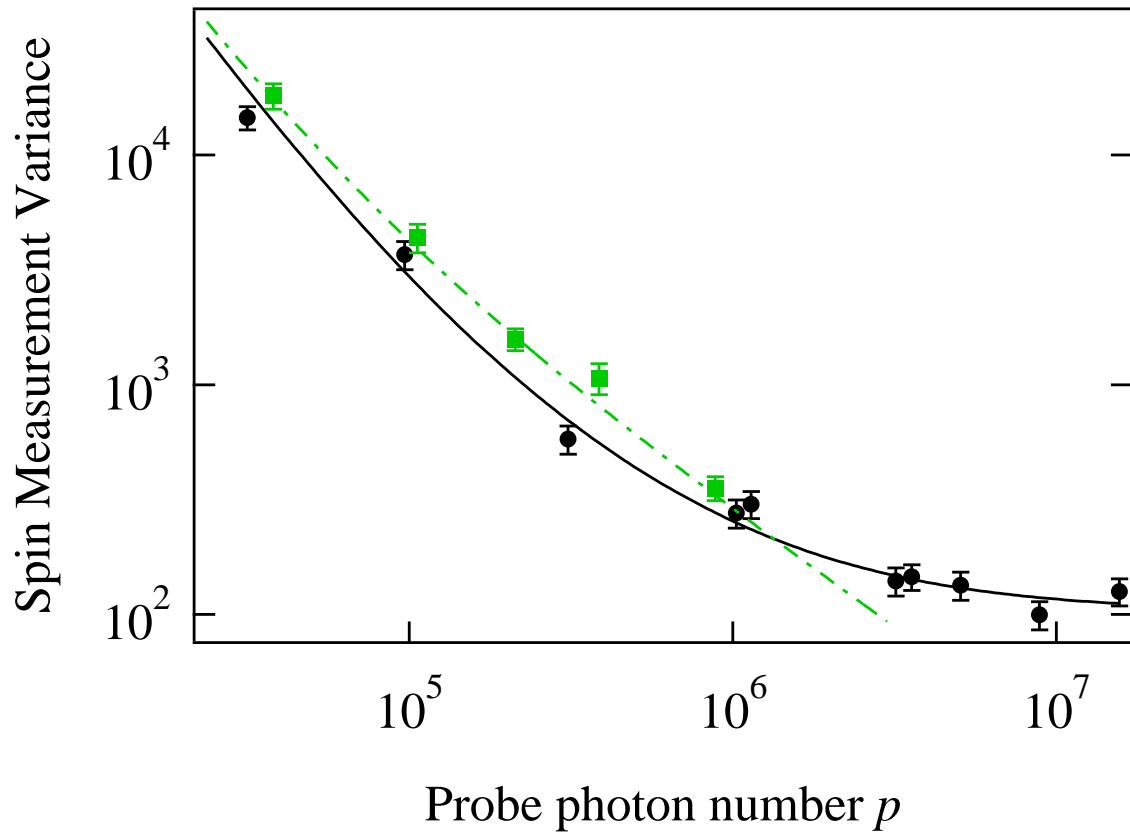
Figure 4-4: Atom-free measurement variance $\Delta M^2_{\mathrm{QND}}$: comparison of observed noise, either with (green) or without (black) compensation sideband, with the model of Eq. 4.4.

our determination of S_z in the state *at the end of the first measurement* (and, equivalently, the beginning of the second).

Figure 4-5 shows the spin measurement variance $[\Delta M^2]_{S_z} = \text{Var}(M_1 - M_2)/2$, as a function of the number of photons p_0 used in each measurement, for measurements either without atoms (open green squares) or with $2S = 3.3(2) \times 10^4$ atoms (solid blue diamonds) prepared in a CSS along $\hat{x}$. All data in Fig. 4-5 were obtained with a compensation sideband; similar data without the compensation sideband are presented in the thesis of Ian Leroux [12]. The variance observed without atoms follow the same curve (green) used to model the single-pulse variance ΔM^2_{QND} in Fig. 4-4, confirming that the noise of the two measurements is uncorrelated. The variance observed with atoms is consistent with a model $[\Delta M^2]_{S_z} = b_{-2}p^{-2} + b_{-1}p^{-1} + b_0 p^0 + b_1 p^1$, where the coefficients b_{-2} and b_{-1} are as given above; the coefficient b_0 is modified to include atom-related technical noise that is independent of photon number, including the effects of imperfect microwave rotations in the spin echo procedure; and the final term describes noise due to photon (Raman) scattering, $[\Delta M^2]_{S_z} \propto p$. The known atom-dependent noise contributions are quantified as follows:

- **Microwave infidelity:** The $\tilde{\pi}$ pulse used in the spin echo produces $98(1)\%$ inversion. We model the imperfect $\tilde{\pi}$ pulse as a perfect one combined with an incoherent process that flips on average $\mu = 2(1)\%$ of the spins, yielding $b_{0,\mu} = \mu S/2$. We treat the errors as incoherent because the atomic phase is inhomogeneously broadened by $(\phi_0/2)p = 1.3 \times 10^{-4} p$ radians when the microwaves are applied. At the optimum photon number $p = 3 \times 10^5$ for squeezing by measurement, the Ramsey contrast remaining after a single probe pulse is only $10(3)\%$ (see Fig. 2-3).

- **Raman scattering:** In our system, the probability of a Raman scattering event is $P_{\text{Ram}} = 5.6 \times 10^{-8}$ per probe photon transmitted through the resonator. This value, calculated including the full excited-state and ground-state hyperfine structures, includes probabilities $P_{\text{Ram}} = P_{\Delta F} + P_{\Delta m_F} + P_{\Delta F \Delta m_F}$ corresponding to three types of scattering events: those which change F but not m_F, those which change m_F but not F, and those which change both F and m_F, respectively. To first order in these probabilities, the total contribution of Raman scattering to the measurement variance (see App. C and Ref. [79]) is $b_1 = (4/3 P_{\Delta F} + 1/2 P_{\Delta m_F} + 1/3 P_{\Delta F \Delta m_F})N = 4.7 \times 10^{-8} S/2$ per probe photon.

Figure 4-5 shows a fit of the above model (solid blue curve) to the observed measurement variance in atom number units, $4[\Delta M^2]_{S_z}$, at $N = 3.3(2) \times 10^4$ and variable photon number p (solid blue diamonds). We fix the noise contributions enumerated above and leave free a term $b_{0,tech}$ to account for any additional technical noise that is independent of probe photon number. With this single free parameter $b_{0,tech} = 350(100) = 0.04(1)S/2$, the data show good agreement with our noise model. We no longer observe the extra noise $b_{0,tech}$ in the upgraded probing scheme adopted subsequent to our measurement squeezing experiments [12].
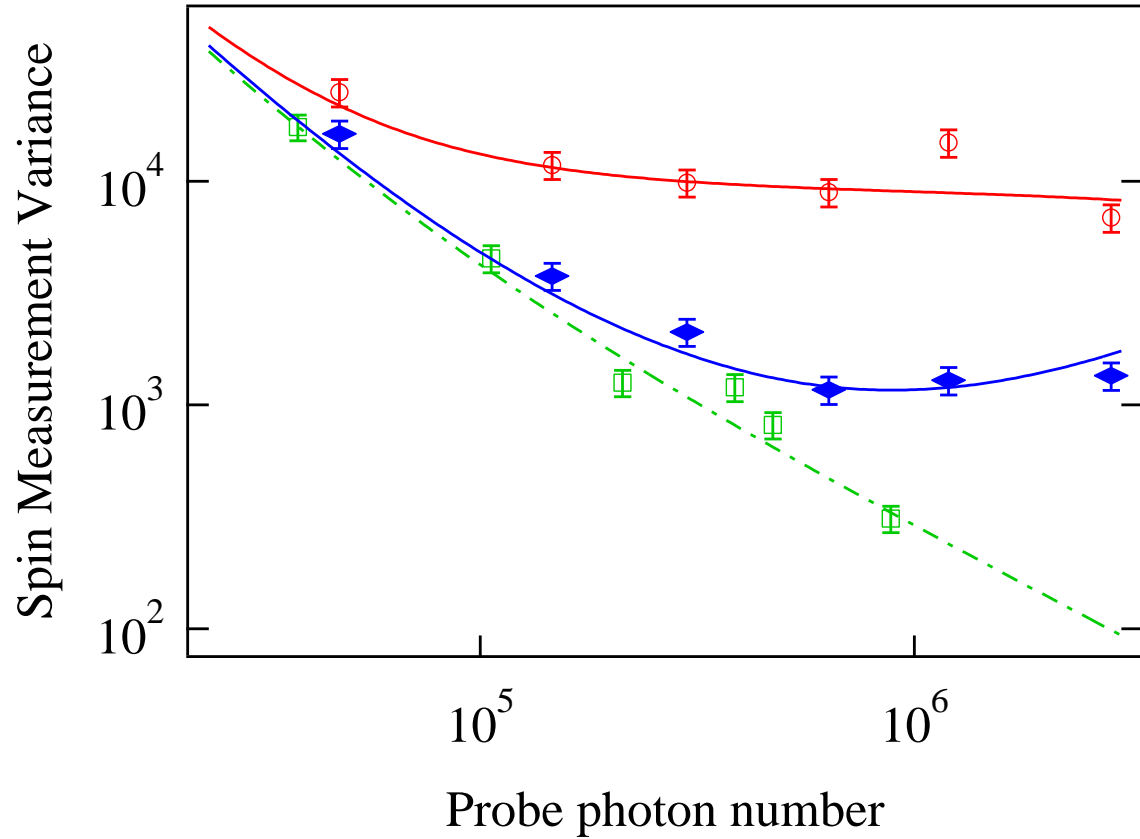
Figure 4-5: Comparison of observed variances with noise model. Shown as a function of probe photon number p are the measurement variance in atom number units, $[\Delta M^2]_{S_z} = \mathrm{Var}(M_1 - M_2)/2$, with (solid blue diamonds) and without (open green squares) atoms; and the variance $\mathrm{Var}(M_1)$ with atoms (open red circles), which includes the CSS projection noise. Curves correspond to the noise model described in the text.

In addition, we plot the variance $\mathrm{Var}(M_1)$ of a single measurement performed on the CSS (open red circles in Fig. 4-5), which includes the CSS projection noise. These data are consistent with a model $\mathrm{Var}(M_1) = b_{-2}/p^2 + b_{-1}/p + b_{0,\mathrm{tech/prep}} + (1 - \mu - [2P_{\Delta F}/3 + P_{\Delta m_F}/2 + 2P_{\Delta F \Delta m_F}/3]p)S/2$ (see App. C and Ref. [79]), where we fit the term $b_{0,\mathrm{tech/prep}} = 0.14(7)S/2$ to allow for technical noise in the state preparation but constrain all other parameters to the values given above.

Chapter 5

Squeezing by Quantum Nondemolition Measurement

> *Quantum mechanics tells us that, whenever a person measures some property of an electron (or of any other object in the microworld), his measurement inevitably will disturb the electron in a somewhat unpredictable way. The more accurate the measurement, the bigger and more unpredictable the disturbance. The disturbance is not due to the person's incompetence; rather, it is an intrinsic and inevitable feature of the laws of quantum mechanics.*
>
> —V. B. Braginsky, Y. I. Vorontsov, and K. S. Thorne, "Quantum Nondemolition Measurements" [80]

Only a select class of measurements is capable even in principle of surpassing the standard quantum limit (SQL). Every measurement has a backaction that serves to enforce the Heisenberg bound on uncertainty products $\Delta\hat{A}\Delta\hat{B} \geq |\langle[\hat{A},\hat{B}]\rangle|/2$ of non-commuting observables $\hat{A}$ and $\hat{B}$, so that a very precise measurement of $\hat{A}$—on the scale of the SQL—necessarily perturbs some other variable(s) $\hat{B}$. Care must therefore be taken to ensure that "what happens to $\hat{B}$ stays in $\hat{B}$" without affecting the subsequent evolution of $\hat{A}$, in order for the measurement result to remain valid. In particular, producing conditional squeezing requires a measurement after which the system remains in a state corresponding to the measurement outcome: a quantum non-demolition (QND) measurement [80, 81].

Our Hamiltonian (recalling Eq. 2.3)

$$H_{\text{sys}} = \hbar\omega_c c^\dagger c + \hbar\Omega c^\dagger c S_z + \hbar\omega S_z \tag{5.1}$$

has two important features that allow for a QND measurement of S_z. First, the interaction term $\propto c^\dagger c S_z$ provides a mechanism for transferring information about S_z to the probe light. Second, all terms in H_{sys} commute with S_z, so that neither the measurement itself nor the subsequent free evolution changes S_z. As discussed in Ch. 2, however, this Hamiltonian is idealized in that it does not include the effects of spontaneous emission from the excited state

used for probing. In actual fact, S_z-changing Raman scattering events place a fundamental limit on how far the measurement precision can exceed the SQL. In Sec. 5.1, I shall show that this fundamental limit is set by the optical depth of the atomic sample, so that the large optical depth achievable in an optical cavity enables measurements far below the standard quantum limit.

Sections 5.2-5.5 describe our experimental demonstration of conditional squeezing, which relies not only on performing a QND measurement of S_z with sensitivity below the SQL but also on preserving the coherence of the spin state. We achieve 3.0(8) dB of spin squeezing by QND measurement.

5.1 Theory

In squeezing by measurement, the reduction in spin fluctuations is *conditional*. The *unconditional* fluctuations in S_z after a QND measurement—which, by definition, does not alter S_z—are the same as they were in the initial uncorrelated state. Yet conditioned on the measurement outcome M, the expectation value $\langle S_z \rangle_M$ is altered and the uncertainty $[\Delta S_z^2]_M$ is reduced. I shall specifically use M to denote an estimate of S_z based on its effect on the probe (perhaps indirectly, e.g., via a detected photocurrent) without recourse to any prior knowledge of S_z. The conditional expectation value $\langle S_z \rangle_M$, on the other hand, represents the best prediction of S_z based not only on the probing but also on any prior knowledge of S_z given the initial state (e.g., a CSS with $\langle S_z \rangle = 0$). This prediction is a weighted average $\langle S_z \rangle_M = wM + (1-w)\langle S_z \rangle$ of the measurement outcome and the unconditional mean $\langle S_z \rangle$, where $w = \mathrm{Cov}(M, S_z)/\mathrm{Var}(M)$ is the weight that minimizes the variance $[\Delta S_z^2]_M = \mathrm{Var}(wM + (1-w)\langle S_z \rangle - S_z)$ of the difference between the prediction and the actual value of S_z.[1] Using this optimal weighting, one obtains the conditional variance

$$[\Delta S_z^2]_M = \frac{\mathrm{Var}(M)\mathrm{Var}(S_z) - \mathrm{Cov}(M, S_z)^2}{\mathrm{Var}(M)}. \tag{5.2}$$

Note that Eq. 5.2 is quite general; in particular, S_z and M could be replaced by any two linearly related commuting observables. By considering the equivalent of Eq. 5.2 with S_z and M interchanged, we obtain a useful relation

$$[\Delta S_z^2]_M = \frac{\mathrm{Var}(S_z)}{\mathrm{Var}(M)}[\Delta M^2]_{S_z} \tag{5.3}$$

between the conditional variance $[\Delta S_z^2]_M$ of S_z and the fluctuations $[\Delta M^2]_{S_z}$ in the measurement outcome at fixed S_z—i.e., the measurement imprecision.

To interpret M as a spin measurement and $[\Delta M^2]_{S_z}$ as its imprecision in spin units, one must assume not only that M scales linearly in S_z but also that the scale-factor is unity,

---

[1] I use the notation $\mathrm{Var}(\cdot)$ and $\mathrm{Cov}(\cdot, \cdot)$ to denote expressly unconditional variances and covariances.

i.e., $\langle M \rangle_{S_z} = S_z$. This condition can always be satisfied by an appropriate definition of M in terms of the detected observable. The resulting relation $\mathrm{Var}(M) = \mathrm{Var}(S_z) + [\Delta M^2]_{S_z}$ allows us to express the conditional variance of S_z in a more intuitive form using Eq. 5.3:

$$[\Delta S_z^2]_M = \frac{\mathrm{Var}(S_z)[\Delta M^2]_{S_z}}{\mathrm{Var}(S_z) + [\Delta M^2]_{S_z}}. \tag{5.4}$$

In the limit $[\Delta M^2]_{S_z} \gg \mathrm{Var}(S_z)$ of a weak measurement, the uncertainty in S_z is still set by the unconditional spin variance $\mathrm{Var}(S_z)$ of the input state; whereas in the opposite limit $[\Delta M^2]_{S_z} \ll \mathrm{Var}(S_z)$, the conditional variance $[\Delta S_z^2]_M$ is simply set by the measurement imprecision $[\Delta M^2]_{S_z}$.

Let us apply these relations to determine the conditional noise reduction attainable by an optimal QND measurement of S_z via the cavity transmission. For detection at the photon shot noise limit, with perfect quantum efficiency, the measurement imprecision $[\Delta M^2]_{S_z}$ depends only on the number of transmitted photons p and on the relation between the cavity transmission and S_z. Provided that the atom-induced cavity shifts $\delta\omega_c = \Omega S_z$ are small compared to the cavity linewidth ($\Omega\sqrt{S/2} \ll \kappa$), we have $|dp/dS_z| = \varphi p_0$, where $\varphi = 2\Omega/\kappa$ and p_0 is the mean transmitted photon number at the optimum probe-cavity detuning $\delta = \kappa/2$. Assuming the input field to be in a coherent state,[2] $[\Delta p^2]_{S_z} = p_0$. The measurement imprecision is then given by

$$[\Delta M^2]_{S_z}^{\mathrm{psn}} = \frac{[\Delta p^2]_{S_z}}{|dp/dS_z|^2} = \frac{1}{p_0\varphi^2}. \tag{5.5}$$

Assuming the measurement to be performed on a coherent spin state in the xy plane, so that $\mathrm{Var}(S_z) = \Delta S_{z\,\mathrm{CSS}}^2 = S/2$, we obtain via Eq. 5.4 a normalized conditional spin noise

$$\sigma^2 \equiv \frac{[\Delta S_z^2]_{M_1}}{\Delta S_{z\,\mathrm{CSS}}^2} = \frac{2}{2 + Q}, \tag{5.6}$$

where $Q \equiv S p_0 \varphi^2$.

The parameter Q governing the degree of spin noise reduction is directly proportional to the number of photons scattered into the cavity during the measurement. This can be seen from the relations in Sec. 2.5, which yield $Q = N\eta\Gamma_{\mathrm{sc}}\mathcal{T}$, where Γ_{sc} is the single-atom scattering rate into free space and $\mathcal{T}$ the total time for which the probe light is applied. Significantly, the relationship between Q and Γ_{sc} is independent of the probe-atom detuning Δ, so that detrimental effects of scattering cannot be ignored at any detuning. How far one can reduce the spin noise before being thwarted by scattering depends only on the collective cooperativity $N\eta$ (resonant optical depth $2N\eta$).

In particular, the main limitation on squeezing is imposed by Raman scattering [55,56,

---

[2]For a given (constant) S_z, the output field is then also in a coherent state because the cavity response is linear.

64]. By changing the atomic state over the course of the measurement, Raman scattering reduces the correlation between the measurement outcome and the actual value of S_{zf} of S_z at the *end* of the measurement, which characterizes the final state. As I show in App. C, the difference between S_{zf} and the average value $\overline{S_z}$ over the course of the measurement fluctuates as

$$\frac{\mathrm{Var}(S_{zf} - \overline{S_z})}{\Delta S_{z\,\mathrm{CSS}}^2} \approx \frac{4}{3}\rho\Gamma_{\mathrm{sc}}\mathcal{T} = \frac{4\rho Q}{3N\eta}, \tag{5.7}$$

where $\overline{S_z}$ represents the average value of S_z during the measurement and ρ represents the fraction of all scattering events that change the atomic state. (In an idealized three-level scheme, $\rho = 1/2$.) In the limit $Q \gg 1$ of interest for squeezing, the normalized spin noise conditioned on the measurement is then

$$\sigma_{\mathrm{scatt}}^2 \approx \frac{2}{Q} + \frac{4\rho Q}{3N\eta} \geq 4\sqrt{\frac{2\rho}{3N\eta}}, \tag{5.8}$$

where the minimum noise is reached at an optimum measurement strength $Q = \sqrt{3N\eta/(2\rho)}$. In our experiment, where a fraction $\rho = 1/3$ of all scattering events are Raman scattering events, at a typical collective cooperativity $N\eta = 3000$ Eq. 5.8 predicts 15 dB of spin squeezing.

5.2   Experimental Setup

The essential features of our experimental setup have been described in Ch. 3. The probe light is placed at a detuning $\Delta = 3.57(1)$ GHz from the $F = 2 \to F' = 3$ transition and is accompanied by a compensation sideband (see Sec. 3.4), placed on the opposite slope of a cavity mode 25 GHz from $F = 2 \to F' = 3$ transition, to reduce the sensitivity of the total cavity transmission to laser frequency noise. The differential shift $\delta\omega_c - \delta\omega_c'$ of the probe and compensation modes is directly proportional to S_z and independent of total atom number. Accounting for the full excited-state hyperfine structure and the inhomogeneous coupling to the probe mode, including the effect of a radial cloud size $\sigma_{\mathrm{r}} = 8(1)$ μm $\ll w$, we calculate $(\delta\omega_c - \delta\omega_c')/(2\pi) = S_z \times 89(3)$ Hz.

In a typical experiment (Fig. 5-1), after initializing the ensemble spin state by optical pumping (see App. B) into $|\downarrow\rangle = |F = 1, m_F = 0\rangle$ (**A**) and applying a $\pi/2$ microwave pulse to rotate the CSS into an equal superposition of $|\downarrow\rangle$ and $|\uparrow\rangle = |F = 2, m_F = 0\rangle$ (**B**), we perform two measurements M_1 and M_2 to induce and verify conditional spin squeezing. Each measurement uses the spin-echo technique described in Sec. 4.4 to minimize probe-induced dephasing. We quantify spin noise ΔS_z^2 by extracting variances from 100 repetitions of such a sequence.
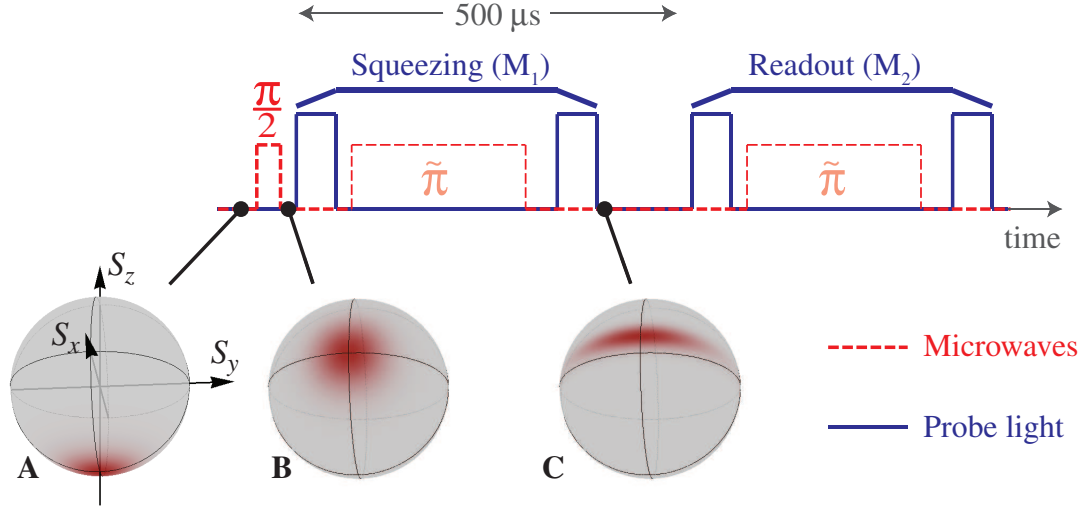
Figure 5-1: Timing of probe pulses (solid line) and microwave pulses (dashed line) in preparation and readout of a squeezed state. Also shown are semiclassical probability distributions on the Bloch sphere depicting the coherent spin states (**A**-**B**) and conditionally squeezed state **C** described in the text.

5.3   Conditional Spin Noise

Essential to quantifying spin squeezing is an accurate calibration of the coherent spin state projection noise. We determine the CSS projection noise level $\Delta S_{z\,\mathrm{CSS}}^2 = S/2$ directly from the measured effective atom number $N = 2S$, as our detailed understanding of the atom-cavity coupling (see Secs. 2.3-2.4) gives us a reliable measure of N (see Sec. 4.2). We verify our understanding of the CSS projection noise either by evaluating the variance $\mathrm{Var}(M_1)$ of the set of single measurements M_1; or by inserting between two measurements $\tilde{M}_1$ and $\tilde{M}_2$ a second CSS preparation, consisting of optical pumping into state $|\downarrow\rangle$ and a $\pi/2$ pulse, and evaluating $\mathrm{Var}(\tilde{M}_1 - \tilde{M}_2)/2$. Fig. 5-2 shows the dependence of the corresponding quantities $v_1 = \mathrm{Var}(M_1)$ (open triangles) or $v_2 = \mathrm{Var}(\tilde{M}_1 - \tilde{M}_2)/2$ (open circles) on S. For an ideal CSS preparation, one expects the linear scaling $v_{1,2} = a_0 + S/2$ indicated by the dashed red line, where a_0 is an offset associated with the measurement uncertainty. However, technical noise—e.g., due to microwave power fluctuations or any sensitivity of the measurement to fluctuations in total atom number—can add to $v_{1,2}$ a contribution which generically scales quadratically in atom number. The data are well fit by a quadratic model $v_{1,2} = a_0 + a_1 S + a_2 S^2$ (solid curve), where we constrain the linear slope $a_1 = 1/2$ and find a small technical noise contribution $a_2 S^2 < \Delta S_{z\,\mathrm{CSS}}^2$ with $a_2 = 9(3) \times 10^{-6}$. Slow drifts in microwave power of 0.4% over the set of measurements could account for the technical noise of v_1, which vanishes if the data are analyzed by comparing only adjacent cycles of

63
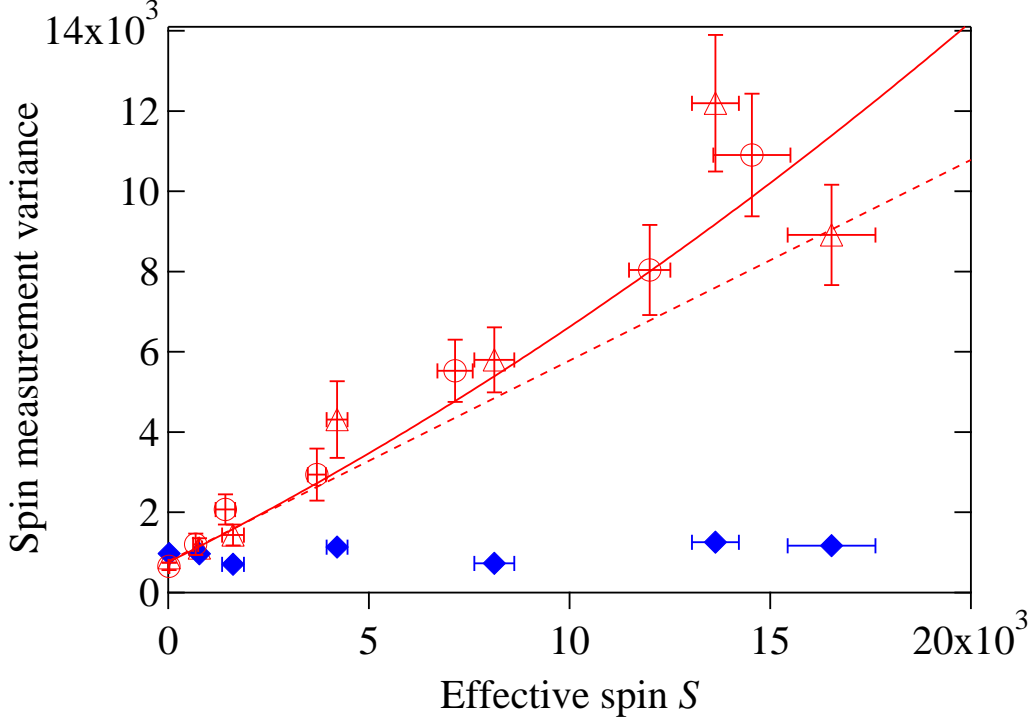
Figure 5-2: Spin noise measurements (see text): $v_1 = \mathrm{Var}(M_1)$ for a single CSS preparation (open triangles), $v_2 = \mathrm{Var}(\tilde{M}_1 - \tilde{M}_2)/2$ for two independently prepared CSSs (open circles), and $[\Delta M^2]_{S_z} = \mathrm{Var}(M_1 - M_2)/2$ for two measurements after a single CSS preparation (solid diamonds), all in units of atom number. Vertical error bars are statistical; horizontal error bars indicate standard deviation of measured atom numbers. The dashed line indicates the projection noise $\Delta S^2_{z\,\mathrm{CSS}} = S/2$ calculated from the measured atom number $2S$. The solid line is the quadratic fit with $a_2 = 9 \times 10^{-6}$, as described in the text.

the experiment.[3] Our ability to prepare an initial unentangled state close to a CSS—with S_z variance $\Delta S^2_{z\,\mathrm{prep}} \sim 1.3S/2$ for our largest atom number—is not a prerequisite for spin squeezing but does provide independent confirmation of the CSS reference level for spin noise measurements. We emphasize that, in quantifying spin squeezing below, we normalize to the actual CSS noise $\Delta S^2_{z\,\mathrm{CSS}} = S/2$ as obtained from our cavity parameters (dashed line), not to the 30% larger slope of the unconstrained quadratic fit to $v_{1,2}$.

To prepare a state with (conditionally) reduced ΔS^2_z (Fig. 5-1**C**), we simply measure S_z for a CSS on the x-axis with a transmitted photon number $p \approx 5 \times 10^5$ sufficient to resolve S_z beyond the CSS variance. Each such measurement M_1 yields a value of S_z

---

[3]This alternative analysis, in which we compare each measurement M_1 with the value M_1^{prec} in the preceding experiment cycle, yields a fit $\mathrm{Var}(M_1 - M_1^{\mathrm{prec}})/2 = 660(100) + 0.95(23)S/2 + 1(9) \times 10^{-6}S^2$, i.e. a result consistent with no contribution from the quadratic term. The variance $v_2 = \mathrm{Var}(\tilde{M}_2 - \tilde{M}_1)/2$ in Fig. 5-2 (open circles) is immune to slow drifts in microwave power. However, long after completing these experiments, we discovered that the state preparation preceding the measurement $\tilde{M}_2$ was compromised by an effect of leakage light during that preparation, which may account for the small technical noise observed in v_2.

that is random but known, as verified by a readout measurement M_2. Provided that S_z is not altered appreciably by M_1 (or in between the two measurements), and provided the measurements M_1, M_2 are identical and uncorrelated, $[\Delta M^2]_{S_z} \equiv \text{Var}(M_1 - M_2)/2$ represents the uncertainty of any single such measurement. We plot $[\Delta M^2]_{S_z}$ vs. S in Fig. 5-2 (solid blue diamonds), finding it a factor of 2 above the photocurrent noise level, with very weak dependence on atom number, and well below the CSS level. The variance $[\Delta M^2]_{S_z}$ is consistent with the noise model described and experimentally verified in Sec. 4.5, which establishes that the two identical measurements are indeed to a good approximation non-demolishing and uncorrelated at $p \approx 5 \times 10^5$. (At this photon number, spin flips induced by free-space scattering contribute at most 3.1(3)% of CSS projection noise to $[\Delta M^2]_{S_z}$; while negligible compared to the CSS level, this contribution can explain part of the small remaining variance of $M_1 - M_2$.)

In terms of the single-measurement uncertainty $[\Delta M^2]_{S_z}$, the conditional variance of the state after measurement M_1 is given by Eq. 5.4 as $[\Delta S_z^2]_{M_1} = \Delta S_{z\,\text{prep}}^2 [\Delta M^2]_{S_z}/(\Delta S_{z\,\text{prep}}^2 + [\Delta M^2]_{S_z})$. Here $\Delta S_{z\,\text{prep}}^2 \equiv \text{Var}(M_1) - [\Delta M^2]_{S_z}$ represents the variance of the state preparation process—close to, but above, the CSS value. Information gained in the measurement M_1 reduces the conditional variance from $\Delta S_{z\,\text{prep}}^2$ to a level that approaches the measurement imprecision $[\Delta M^2]_{S_z}$ in the limit $[\Delta M^2]_{S_z} \ll \Delta S_{z\,\text{prep}}^2$. At $N_0 = 3.3(2) \times 10^4$ and $p = 6 \times 10^5$, we observe a normalized spin noise $\sigma^2 \equiv [\Delta S_z^2]_{M_1}/\Delta S_{z\,\text{CSS}}^2 = -9.1(8)$ dB (plotted in Fig. 5-4 below). A slight correction for the effect of photon scattering (see App. C.2) yields $\sigma^2 = -8.8(8)$ dB.

The reduction of $[\Delta S_z^2]_{M_1}$ below the CSS value $\Delta S_{z\,\text{CSS}}^2$ is accompanied by an increase in ΔS_y^2 that is ~ 20 dB larger than required by the Heisenberg relation $\Delta S_y^2 [\Delta S_z^2]_{M_1} \geq [\hbar |\langle S_x \rangle|/2]^2$. As the fluctuations ΔS_y^2 are well described by the cavity feedback model presented in Ch. 6, I will quantify and discuss them in that context.

5.4   Coherence

To verify spin squeezing, we need to measure not only noise but also the signal size $|\langle S_x \rangle|$, observable as the interference contrast $\mathcal{C} = |\langle S_x \rangle|/S$ of Rabi oscillations driven subsequent to the squeezing measurement M_1. We measure $\mathcal{C}$ at an atom number $N = 4.0(1) \times 10^3$ by applying a microwave rotation about $\hat{y}$, of variable duration, between the measurements M_1 and M_2 (during which time both the probe light and the resonator locking light are off). Figure $5-3$ shows the Rabi oscillations as detected by the readout measurement M_2 of S_z, for various probe photon numbers p applied during M_1. The contrast as a function of photon number p is summarized in Fig. 5-4 below.

We observe a contrast loss that is linear in probe photon number p, as well as a process that imparts shot-to-shot phase fluctuations (via imbalances in the intracavity probe power between the two spin echo pulses) and yields a reduction in $|\langle S_x \rangle|$ that is quadratic in p.
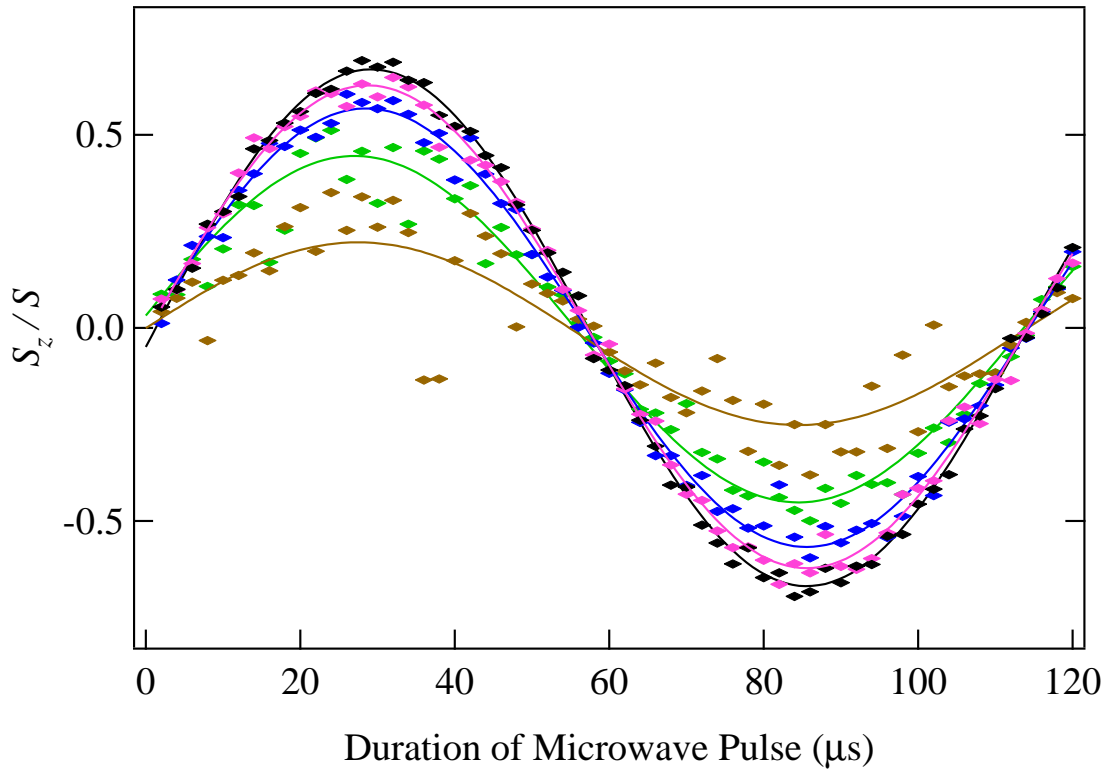
Figure 5-3: Rabi oscillations for determination of interference contrast. The black diamonds and outermost curve correspond to the initial contrast with only lock light, the other curves to probe photon numbers between $p = 10^5$ and $p = 9 \times 10^5$.
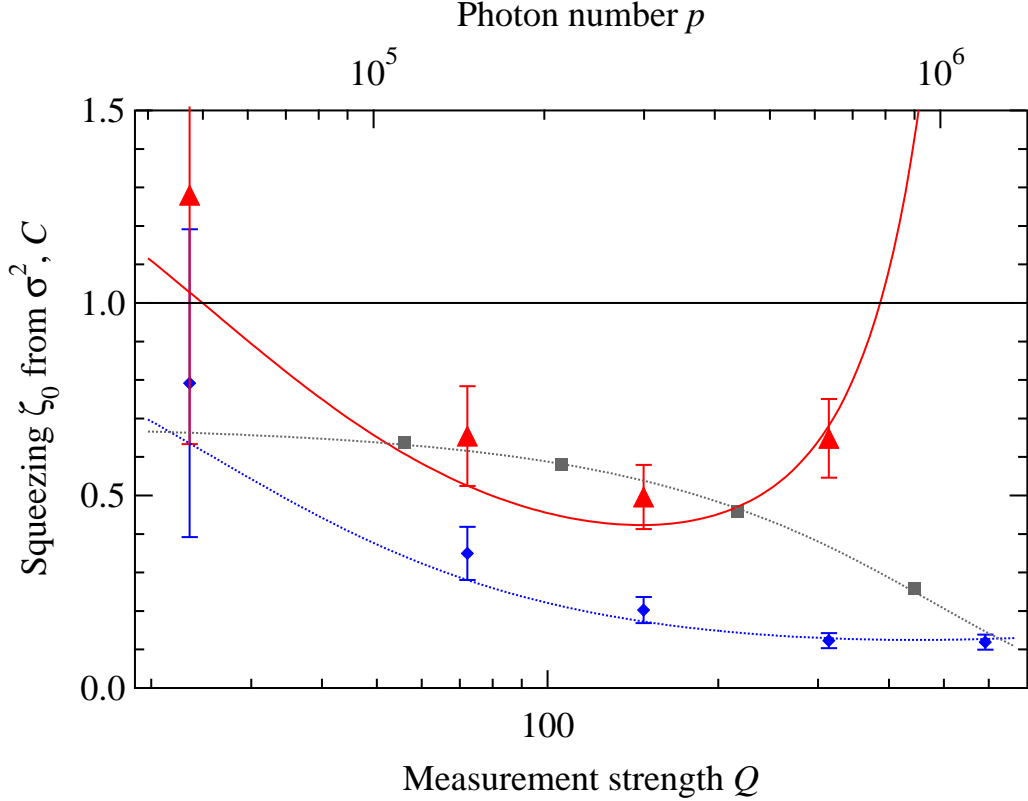
Figure 5-4: Measured data with fits of simple models for normalized spin noise $\sigma^2 = [\Delta S_z^2]_{M_1}/\Delta S_{z\,\mathrm{CSS}}^2$ (open diamonds), contrast $\mathcal{C}$ (open squares), and squeezing parameter ζ_0 (solid triangles).

We therefore fit to the data in Fig. 5-4 the expression $\mathcal{C} = \mathcal{C}_0 \exp(-\alpha p - \beta p^2/2)$, obtaining $\alpha = 7(1) \times 10^{-7}$, $\beta = 9(4) \times 10^{-13}$, and $\mathcal{C}_0 = 0.69(1)$.

The contrast measurement is performed at a relatively low atom number for two reasons. First, at large atom number, atom projection noise augments the imbalances in intracavity probe power between the spin echo pulses and thus augments the resulting phase fluctuations; this effect can in principle be compensated using the result of the squeezing measurement. (Alternatively, one can take advantage of this effect to perform cavity feedback squeezing: see Ch. 6.) Second, at lower atom number, the entire Rabi oscillation curve is in the linear regime of the Lorentzian resonator transmission profile. A method of measuring contrast at large atom number in spite of the non-linear transmission signal, which we have applied in more recent experiments, is described in the thesis of Ian Leroux [12].

5.5   Conditional Squeezing

Figure 5-4 shows both the contrast $\mathcal{C}$ (gray squares) and the normalized spin noise $\sigma^2 = [\Delta S_z^2]_{M_1}/\Delta S_{z\,\mathrm{CSS}}^2$ (blue diamonds) as a function of photon number p used in the state-

preparation measurement M_1. Also shown are a fit to σ^2 (dotted blue curve), based on the noise model in Sec. 4.5, and the fit to the contrast described in Sec. 5.4 above (dotted gray curve). The combination of these two datasets allows us to quantify the angular sensitivity of the state prepared by M_1 with p probe photons as $\Delta\theta^2(p) = [\Delta S_z^2]_{M_1}/|\langle S_x\rangle|^2 = \sigma^2/(2S\mathcal{C}^2)$. The red triangles show the ratio $\zeta_0 \equiv \Delta\theta^2(p)/\Delta\theta_0^2$, where $\Delta\theta_0^2 = 1/(2S_0)$ represents the projection-noise-limited sensitivity of a CSS with the spin length $S_0 = S\mathcal{C}(0)$ obtained when no probe light is applied. The angular sensitivity initially improves with photon number— as indicated by a decrease in ζ_0—until reaching an optimum $\zeta_0^{-1} = 3.0(8)$ dB improvement in signal-to-noise ratio, conditioned on a measurement with $p = 3 \times 10^5$ probe photons.

If the unentangled reference state at $p = 0$ is maximally coherent ($S_0 = S$), then the condition $\zeta_0 < 1$ is precisely the Wineland criterion for spin squeezing introduced in Sec. 1.3. Otherwise, $\zeta_0 < 1$ still demonstrates a gain for metrology, but the attribution of this gain to spin squeezing—i.e., to non-classical spin correlations—requires some knowledge of how the measurement can or cannot change the atomic state. Provided M_1 does not *increase* the classical spin correlations in the xy plane, then it cannot reduce $\zeta_0 \propto \Delta\theta^2(p)$ without introducing entanglement (e.g., non-classical correlations along $\hat{z}$). This can be seen from the relation

$$\Delta\theta^2 \equiv \frac{\Delta S_z^2}{\langle S_x\rangle^2 + \langle S_y\rangle^2} = 1 - \frac{\sum_{i\neq j}\left(\langle s_x^i\rangle\langle s_x^j\rangle + \langle s_y^i\rangle\langle s_y^j\rangle\right)}{\langle S_x\rangle^2 + \langle S_y\rangle^2}, \tag{5.9}$$

for an unentangled ensemble where the individual particles have spin $s = 1/2$. For simplicity, I have assumed uniform coupling $\mathbf{S} = \sum_i \mathbf{s}_i$ in writing the spin correlation term $c_{xy} = \sum_{i\neq j}(\langle s_x^i\rangle\langle s_x^j\rangle + \langle s_y^i\rangle\langle s_y^j\rangle)/(\langle S_x\rangle^2 + \langle S_y\rangle^2)$, but the expression readily generalizes to the case of inhomogeneous coupling. Generally, of course, the probe light tends to reduce c_{xy} (i.e., to cause dephasing), not to increase it. More particularly, in order to produce the net reduction in contrast $\mathcal{C}$ that we observe with increasing p, any measurement-induced *increase* in c_{xy} (rephasing) would have to conspire with coherent rotations about $\hat{x}$ or $\hat{y}$ to reduce $\mathcal{C}$ by rotating spins out of the xy plane (in some way that depends on p). The only mechanism for coherent rotation is the $\tilde{\pi}$ pulse we apply for spin echo during M_1, and its $98(1)\%$ fidelity (see Secs. 4.4) ensures that it has no appreciable effect on the spins' polar angles. Therefore, our contrast data establish that c_{xy}, like $\mathcal{C}$, decreases monotonically with photon number p, so that only entanglement can account for the reduction in ζ_0 by our measurement M_1. This confirms that we have demonstrated $\zeta_0^{-1} = 3.0(8)$ dB of spin squeezing by QND measurement.

We can further verify the squeezing using the black-box Wineland criterion (Eq. 1.3). Comparing the sensitivity $\Delta\theta^2(p)$ with the best sensitivity $\Delta\theta^2 = 1/N$ achievable with N uncorrelated atoms results in a Wineland parameter $\zeta = N\Delta\theta^2(p)$, and at $p = 3 \times 10^5$ we achieve $\zeta = 0.7(1)$, corresponding to $\zeta^{-1} = 1.5$ dB of spin squeezing by this strictest measure. The 1.5 dB difference between ζ_0 and ζ in our system is primarily due to the

resonator locking light, an effect that we have since reduced (see Secs. 3.4 and 6.2-6.3) by detuning the locking light further from atomic resonance.

5.6   Outlook

Comparing the normalized spin noise σ^2 in Fig. 5-4 (blue diamonds) with the ideal performance $\sigma^2 \approx 2/Q$ predicted by Eq. 5.6 shows that there is still substantial room for improvement in the noise reduction we attain at fixed measurement strength Q. One direction for improvement is to remove the compensation sideband (to avoid its extra shot noise) and probe closer to atomic resonance to increase the ratio of atom-induced cavity shifts to laser frequency noise. In addition, replacing the side-of-slope transmission measurement with a phase measurement on resonance would yield both practical and fundamental improvements. Practically, such a phase measurement can eliminate the need for avalanche gain in the photodetection (and the accompanying excess noise), as it is performed by mixing the weak probe light with a strong carrier. Fundamentally, the photon-shot-noise-limited scaling improves on cavity resonance to $\sigma^2 = 1/(1 + Q)$—where $Q = N\eta\Gamma_{\rm sc}\mathcal{T}$ as before—since the full cavity enhancement factor is only attained on cavity resonance. In addition, by eliminating cavity-feedback-induced phase fluctuations (see Ch. 6), a measurement performed on cavity resonance can more easily achieve an uncertainty area $\Delta S_y \Delta S_z$ close to the Heisenberg bound.

Even with our current measurement performance, a simple avenue for improvement is to increase the atom number, which has so far been limited by purely technical considerations (specifically, fear of exhausting a long-serving getter source of ^{87}Rb). In a cavity-based setup similar to ours, Chen *et al.* have recently demonstrated spin squeezing with 7×10^5 atoms [8]. Using a comparable number of atoms in our system, at fixed resolution of our QND measurement, we could hope to realize the compounded benefits of greater absolute angular sensitivity at the standard quantum limit and an ~ 8 dB enhancement of that sensitivity by conditional spin squeezing.

Chapter 6

Cavity Feedback Squeezing

> *Although realistic physical schemes are yet to be found, these nonlinear Hamiltonians will provide some clues in the search for squeezed atomic states.*
> —M. Kitagawa and M. Ueda, "Squeezed spin states"

In their seminal proposal of spin squeezing, Kitagawa and Ueda [2] pointed out that a coherent spin state can evolve into a squeezed state under the action of a Hamiltonian that is nonlinear in the spin operators. Whereas the linear, non-interacting Hamiltonian $H = \hbar\omega S_z$ simply generates a precession about the z axis at the rate ω, the "one-axis twisting" Hamiltonian $H \propto S_z^2$ causes a precession about the z axis at a rate proportional to S_z. This twisting distorts an initial coherent spin state (CSS) oriented along $\hat{x}$ into a state that is squeezed along an oblique axis, as illustrated in Fig. 6-1. One demonstrated approach to realizing one-axis twisting dynamics in an atomic ensemble [37–39] is by state-dependent collisional interactions in a Bose-Einstein condensate [32]. Here, I show that similar dynamics can be achieved without direct interatomic interactions by harnessing the collective interaction of an ensemble with a driven cavity mode.

Already in our usual probing scheme (Fig. 2.1), with a laser tuned to the slope of a cavity resonance whose frequency is shifted in opposite ways by atoms in $|\uparrow\rangle$ and $|\downarrow\rangle$, the intracavity intensity depends linearly on S_z. Since the intracavity light produces an AC Stark shift of the transition frequency ω, the precession rate on the Bloch sphere likewise depends linearly on S_z, as in the one-axis twisting described above. If the intracavity light is in a Fock state [12], the dynamics are precisely those of the S_z^2 Hamiltonian. In the most straightforward experimental implementation, however, the intracavity field is in a coherent state, and so the spin evolution is modified by the photon shot noise of the intracavity light. The resulting modified one-axis twisting dynamics nevertheless allow substantial squeezing, as I demonstrate both theoretically (Sec. 6.1) and experimentally (Sec. 6.2) below.

$c_{in,1}^\dagger$ $c^\dagger$ $c_{in,2}^\dagger$

S_z S_z S_z

Coherent spin state   One-axis twisting   Cavity feedback squeezing

$$H \propto S_z^{\,2}$$ $$H \propto c^\dagger c S_z$$
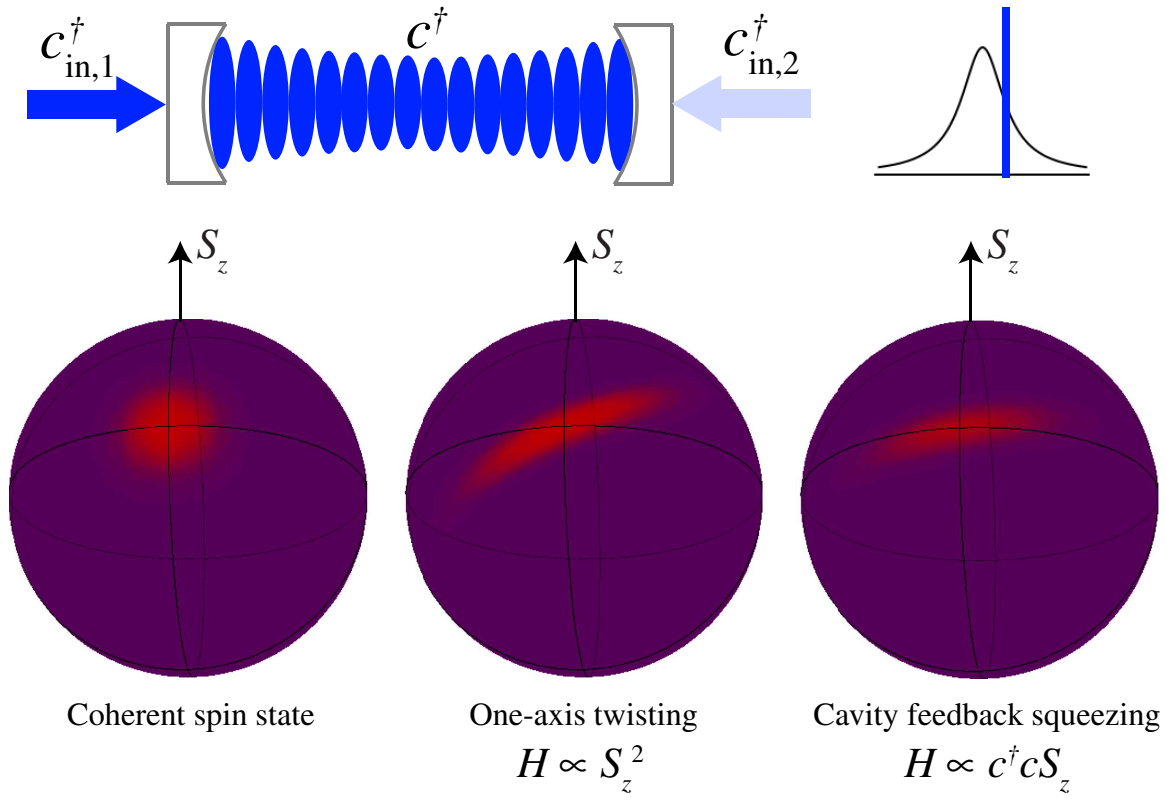
Figure 6-1: Cavity feedback squeezing: a probe laser (blue) is tuned (as in Fig. 2.1) to produce a differential light shift between two atomic states, described by a Hamiltonian $H \propto c^\dagger c S_z$. With the laser tuned to the slope of the cavity resonance, so that the intracavity photon number $c^\dagger c$ depends linearly on S_z, this results in a spin evolution similar to that of the one-axis twisting Hamiltonian $H \propto S_z^2$. Shown are calculated Wigner quasiprobability distributions for a spin $S = 30$ prepared initially in a coherent spin state (left) and evolving either by the true one-axis twisting Hamiltonian (center) or by cavity feedback (right).

6.1 Theory

Let us derive the theory of cavity feedback squeezing in the idealized three-level system first introduced in Sec. 2.1. There, we arrived at a Hamiltonian

$$H_{\text{sys}} = \hbar\omega_c c^\dagger c + \hbar\Omega c^\dagger c S_z + \hbar\omega S_z, \tag{6.1}$$

for the dynamics of the ensemble spin vector $\mathbf{S}$ interacting with the cavity mode containing $c^\dagger c$ photons. The second term produces the shift ΩS_z of the cavity resonance that allows squeezing by QND measurement. Yet the same interaction also produces a shift $\Omega c^\dagger c$ of the atomic transition frequency (between ground states $|\downarrow\rangle$ and $|\uparrow\rangle$) in proportion to intracavity photon number $c^\dagger c$. In combination, the two facets of this interaction—i.e., the action of the atoms on the light via their state-dependent refractive index and the back-action of the light on the atoms via the ac Stark shift—provide the mechanism for cavity feedback squeezing.

The cavity feedback dynamics can conveniently be analyzed in the Heisenberg picture by evaluating the time-evolution of moments of the spin operators. Causality requires that $\left[c^{(\dagger)}(t), \mathbf{S}(t)\right] = 0$ [82, 83], i.e., spin operators commute with field operators at equal times. It follows that S_z is a constant of the motion, while the evolution of an arbitrary spin operator A is given by

$$\frac{dA}{dt} = \frac{\mathrm{i}}{\hbar}\left[H_{\text{sys}}, A\right] = \mathrm{i}\left(\omega + \Omega c^\dagger c\right)\left[S_z, A\right]. \tag{6.2}$$

The cavity annihilation operator c evolves not only according to H_{sys} but also according to its coupling to a bath of modes outside the cavity. The latter can be described by the standard input-output formalism of quantum optics [82, 83], resulting in an equation of motion

$$\dot{c} = \left(-\frac{\kappa}{2} - \mathrm{i}\omega_c - \mathrm{i}\Omega S_z\right)c + \sqrt{\kappa}c_{\text{in}}, \tag{6.3}$$

where the annihilation operator c_{in} can represent either a single input mode of a one-sided cavity or, in the case relevant to our experiments, a superposition $c_{\text{in}} = (c_{\text{in}1} + c_{\text{in}2})/\sqrt{2}$ of the annihilation operators $c_{\text{in}1}, c_{\text{in}2}$ for the input fields from two sides of a symmetric cavity (Fig. 6-1). Since S_z is constant, the only atomic effect on the evolution of c is the static shift ΩS_z of the cavity resonance frequency. For a monochromatic input field in a coherent state $|\beta\rangle$ at frequency ω_L, satisfying $c_{\text{in}}(t)|\beta\rangle = e^{-\mathrm{i}\omega_L t}\beta|\beta\rangle$, the action of the annihilation operator c on the field state thus takes the simple form:

$$c|\beta\rangle = \sqrt{\kappa}\chi(S_z)e^{-\mathrm{i}\omega t}\beta|\beta\rangle, \tag{6.4}$$

where $\chi(S_z) = [\kappa/2 - \mathrm{i}(\omega_L - \omega_c - \Omega S_z)]^{-1}$ represents the S_z-dependent response function of the cavity. The state $|\beta\rangle$ in practice will consist of a coherent state incident from one

side of the cavity, i.e., $c_{\mathrm{in1}}(t)\,|\beta\rangle = \sqrt{2}e^{-\mathrm{i}\omega_L t}\beta\,|\beta\rangle$ and $c_{\mathrm{in2}}(t)\,|\beta\rangle = 0$. The assumption of a monochromatic field is germane because we wish to resolve the cavity line. Specifically, we will choose the laser-cavity detuning $\omega_L - \omega_c = \kappa/2$ to maximize the dependence $|\chi|^{-2}\,d\,|\chi|^2\,/dS_z$ of the cavity response on S_z. To allow the monochromaticity condition to be satisfied, we will always consider interaction times $t \gg \kappa^{-1}$ and assume the light to be turned on adiabatically.

The S_z-dependent cavity response entangles the light with the atoms, so that the spin dynamics alone are non-unitary. Nevertheless, we can obtain equations of motion for the spin subsystem by performing a partial trace over the field state:

$$\frac{d\langle A\rangle_\beta}{dt} \equiv \frac{d\langle\beta|\,A\,|\beta\rangle}{dt} = \frac{\mathrm{i}}{\hbar}\,\langle\beta|\,[H_{\mathrm{sys}}, A]\,|\beta\rangle\,. \tag{6.5}$$

We are interested in the evolution of an atomic system prepared initially in a CSS $|\psi_0\rangle$ along the x axis, satisfying $S_x(0)\,|\psi_0\rangle = S\,|\psi_0\rangle$. Since we wish to obtain a shearing of the CSS uncertainty region and not a more complex distortion, we require that the projection-noise-induced fluctuations in the cavity shift are sufficiently small as to be converted linearly into fluctuations in intracavity intensity, i.e., $\Omega\sqrt{S/2} \ll \kappa$. The resulting atomic phase is described by the spin raising operator S_+, whose moments S_+^q (for whole numbers q) evolve according to Eq. 6.5 as

$$\frac{d\langle S_+^q\rangle_\beta}{dt} = \mathrm{i}q\Omega\,\langle\beta|\,c^\dagger S_+^q c\,|\beta\rangle\,, \tag{6.6}$$

where I have positioned the field operators (which commute with S_+) so that we can apply Eq. 6.4 to obtain

$$\frac{d\langle S_+^q\rangle_\beta}{dt} = \mathrm{i}f_q(S_z)\langle S_+^q\rangle_\beta, \tag{6.7}$$

where

$$f_q(S_z) = \omega + q\frac{\Omega}{\kappa}\,|\beta|^2\left(1 + q(\mathrm{i}-1)\Omega/\kappa + 2(\Omega/\kappa)S_z\right), \tag{6.8}$$

to lowest order in $(\Omega/\kappa)S_z$ and for $q \lesssim \sqrt{S}$.

The phase evolution is most easily visualized in a rotating frame $\tilde{S}_+ \equiv S_+(t)e^{-\mathrm{i}\mathrm{Re}[f_1(0)]t}$, where the rotation rate $\mathrm{Re}[f_1(0)]$ is set by the atomic transition frequency at the light level corresponding to $S_z = 0$. It is now useful to recall the dimensionless parameter $Q = Sp\varphi^2$ defined in Sec. 5.1, proportional to the spin S, average photon number $p = |\beta|^2 t/2$ transmitted for $S_z = 0$ in the time t, and square of the differential atomic phase shift per transmitted photon $\varphi = 2\Omega/\kappa \ll 1$. In terms of Q and the initial spin operators $S_+(0)$ and S_z, Eqs. 6.7–6.8 yield

$$\langle\tilde{S}_+\rangle_\beta \quad = e^{-Q/(2S)}e^{\mathrm{i}QS_z/S}S_+(0), \tag{6.9}$$

$$\langle\tilde{S}_+^2\rangle_\beta \quad = e^{-(2+\mathrm{i})Q/S}e^{2\mathrm{i}QS_z/S}S_+^2(0). \tag{6.10}$$

74

Equation 6.9 shows that the phase on the Bloch sphere evolves at an S_z-dependent rate QS_z/S: we indeed obtain the desired twisting about the z-axis. The twisting is accompanied by a decay, evidencing the decoherence associated with discarding the light once it exits the cavity.

Using Eqs. 6.9–6.10, together with generating functions derived in Ref. [30], we can evaluate various other spin expectation values of interest. In particular, ΔS_z^2 is unchanged, but the S_z-dependent spin precession introduces correlations between S_y and S_z that describe the shearing of the initial CSS uncertainty region:

$$\langle \tilde{S}_y S_z + S_z \tilde{S}_y \rangle = (2S^2 - S)e^{-Q/(2S)} \sin\left(\frac{Q}{2S}\right) \mathcal{G}_S(Q/2), \tag{6.11}$$

where $\mathcal{G}_S(u) \equiv \cos^{2S-1}(u/S)$ is approximately a Gaussian $\mathcal{G}_S(u) \approx e^{-u^2/S}$ in the large-S limit. At the same time, the variance of S_y grows as

$$\Delta \tilde{S}_y^2 = \frac{S^2}{2} + \frac{S}{4} - \left(\frac{S^2}{2} - \frac{S}{4}\right) e^{-2Q/S} \mathcal{G}_S(Q), \tag{6.12}$$

which can be approximated—in the limit of a large ensemble ($S \gg 1$) and small phase $|QS_z/S| \sim Q/\sqrt{S} \ll 1$—as

$$\Delta \tilde{S}_y^2 \approx \frac{S}{2}\left(1 + 2Q + Q^2\right). \tag{6.13}$$

Here, the first term represents the variance $\Delta S_{z\,\mathrm{CSS}}^2 = S/2$ of the initial CSS, while the last represents the variance increase $Q^2 \Delta S_{z\,\mathrm{CSS}}^2$ due to the feedback-induced twisting. The middle term describes a variance increase $QS \propto p$ due to photon shot noise of the intracavity light. This broadening can in principle be eliminated by replacing the coherent-state input field with a Fock state (see Sec. 6.4). Already for the coherent-state field, though, the one-axis twisting dominates over the dissipative effect of photon shot noise due to its stronger scaling with Q.

We verify that the resulting spin state is squeezed by calculating the spin variance along the z axis after rotation about the x axis by an angle $-\alpha$:

$$\Delta S_\alpha^2 = \frac{1}{2}\left(V_+ - \sqrt{V_-^2 + W^2} \cos\left[2(\alpha - \alpha_0)\right]\right), \tag{6.14}$$

where $V_\pm = \Delta \tilde{S}_y^2 \pm \Delta S_z^2$, $W = \langle \tilde{S}_y S_z + S_z \tilde{S}_y \rangle$, and $\tan 2\alpha_0 = W/V_-$ are specified by Eqs. 6.11–6.12.

For moderate squeezing $1 \ll Q^2 \ll S$, the minimum and maximum variances, normalized to the CSS variance, are $\sigma_{\alpha_0}^2 \approx 2/Q$ and $\sigma_{\alpha_0+\pi/2}^2 \approx Q^2$, where $\sigma_\alpha^2 \equiv \Delta S_\alpha^2/(S/2)$. While the antisqueezing increases as Q^2 due to cavity feedback (Eq. 6.13), the minimum variance decreases only as Q^{-1} because of the fluctuations in spin precession angle resulting from photon shot noise in the intracavity light. The phase fluctuations imparted by the

photon shot noise constitute the back-action of an S_z-measurement that could in principle be performed (as is done for conditional squeezing) by detecting the light leaking out of the cavity. Ignoring the information in the outgoing light results in a growing uncertainty product $\sigma_{\alpha_0}\sigma_{\alpha_0+\pi/2} \approx \sqrt{2Q}$.

For a given atom number $2S$, the squeezing improves with photon number p until the shearing in the yz-plane is impeded by the curvature of the Bloch sphere [2, 49]. Expanding the minimum spin variance $\Delta S^2_{\alpha_0}$ to lowest order in the characteristic phase variance $Q^2/(2S)$, we find $\sigma^2_{\alpha_0} \approx 2/Q + Q^4/(24S^2)$. The curvature of the Bloch sphere thus limits the minimum uncertainty to $\sigma^2_{\text{curv}} = (5/2)12^{-1/5}S^{-2/5}$, reached at a shearing strength $Q_{\text{curv}} = 12^{1/5}S^{2/5}$. This is the same scaling with S as derived for an analogous feedback squeezing scheme in free space (Takeuchi *et al.* [49]).

The squeezing also faces the usual competition with Raman scattering. The random spin flips occurring at a rate $\Gamma_{\text{sc}}/2$ reduce the correlation between the time average $\overline{S}_z$ during the squeezing, which determines the evolution of S_y, and the final value $S_z(t)$ when the rotation about the x-axis is performed. To account for the scattering, we replace S_z by $\overline{S}_z$ in Eqs. 6.9 and 6.10 and evaluate the modified variance $\Delta\tilde{S}^2_y$ and covariance $\langle\tilde{S}_yS_z(t) + S_z(t)\tilde{S}_y\rangle$ in the large-S limit using $2\langle S_z(t_1)S_z(t_2)\rangle/S = e^{-\Gamma_{\text{sc}}|t_1-t_2|}$ (see App. C). We apply Eq. 6.14 as before to calculate the minimum normalized variance $\sigma^2_{\alpha_0,\eta}$. To lowest order in the number $\Gamma_{\text{sc}}t$ of scattered photons, and ignoring curvature effects for the moment,

$$\sigma^2_{\alpha_0,\eta} \approx \left(\frac{2}{Q} + \frac{Q}{3S\eta}\right). \tag{6.15}$$

This is precisely the same behavior derived for squeezing by QND measurement (Eq. 5.8), reaching an optimum value $\sigma^2_{\alpha_0,\eta} = \sqrt{\frac{8}{3S\eta}}$ at $Q_{\text{scatt}} = \sqrt{6S\eta}$.

Fig. 6-2 shows the minimum variance $\sigma^2_{\alpha_0,\eta}$ as a function of shearing strength Q for various values of the single-atom cooperativity η, calculated from the full expressions of Eqs. 6.11–6.12 modified as described above to account for Raman scattering. Whether the noise reduction is limited first by scattering or by the curvature of the Bloch sphere depends strongly on η: the curvature limit is reached first for $S\eta^5 \gtrsim 1$. Thus, already in a moderately coupled cavity ($\eta \gtrsim 1$), free-space scattering will generally not be the dominant limitation on the feedback squeezing, and indeed Fig. 6-2 shows that for a total spin $S = 10^4$ there is little to be gained by increasing η into the strong-coupling regime. Conversely, feedback squeezing schemes in free space [49], where $\eta \ll 1$, will generally be limited by scattering rather than reaching the curvature limit.

6.2   Experimental Demonstration

To implement the proposed cavity feedback scheme, we tune the cavity mode 3.18 GHz to the blue of the $F = 2 \to F' = 3$ transition, where it incurs opposite shifts $\pm\Omega/2 =$
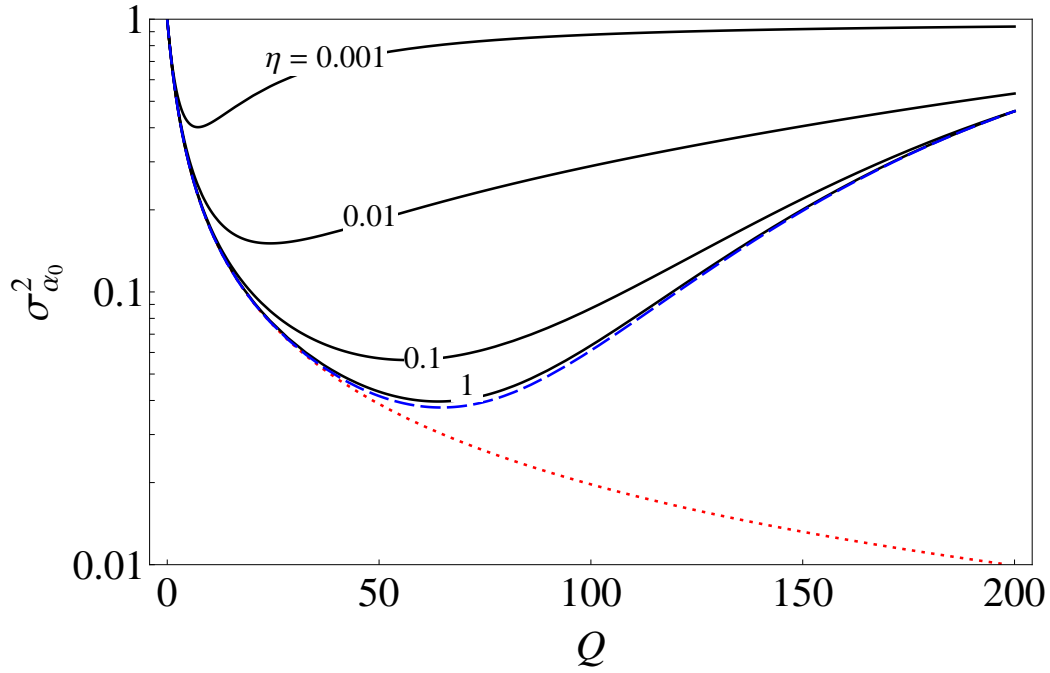
Figure 6-2: Minimum normalized variance $\sigma^2_{\alpha_0,\eta}$ as a function of shearing strength Q for $S = 10^4$ and various single-atom cooperativities $\eta = 0.001, 0.01, 0.1, 1$ (solid lines). The dashed line shows the limit σ^2_{curv} due to the curvature of the Bloch sphere when free-space scattering is ignored. The dotted line shows the variance neglecting both free-space scattering and curvature, scaling as $2/Q$ for $Q \gg 1$.
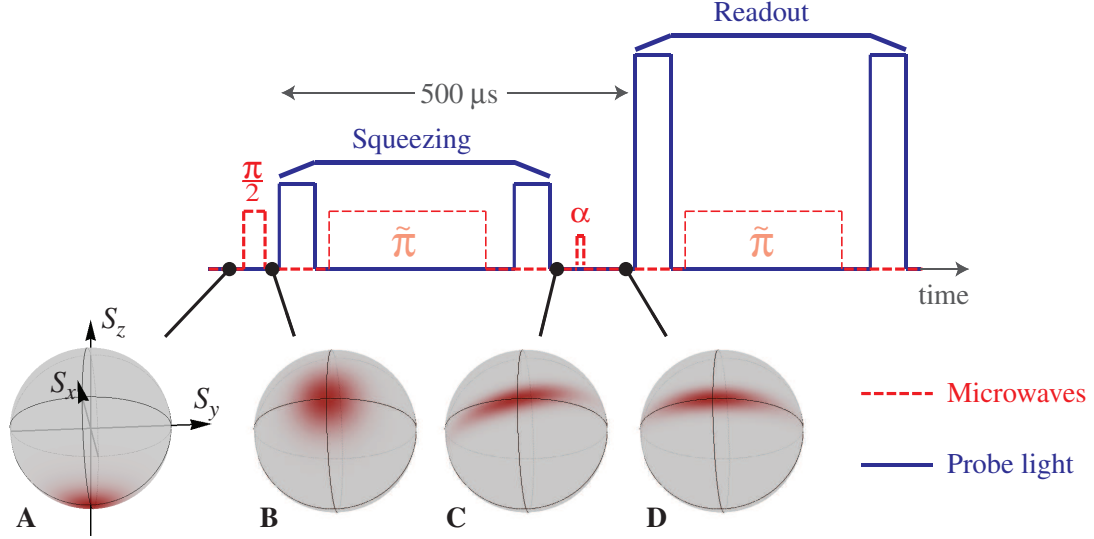
Figure 6-3: Experiment sequence for cavity feedback squeezing and characterization of the prepared state, as described in the text.

89(2) Hz/atom due to atoms in states $|\uparrow\rangle = |F = 2, m_F = 0\rangle$ and $|\downarrow\rangle = |F = 1, m_F = 0\rangle$. As usual, we place the probe laser at a half-linewidth detuning $\delta = \kappa/2$ from cavity resonance, and whenever we apply probe light—both for squeezing and for state readout—we do so with our standard two-pulse spin echo procedure (Sec. 4.4). While the spin echo undoes the precession due to the average light level, it does not cancel the S_z-dependent precession of interest (i.e., the shearing of the spin state) because the $\tilde{\pi}$ pulse changes the sign of S_z.

The squeezed-state preparation and readout sequence is illustrated in Fig. 6-3. It begins, as usual, with optical pumping into $|\downarrow\rangle$ (**A**) and preparation of a CSS along $\hat{x}$ (**B**). It further comprises two applications of probe light, the first at low intensity for coherence-preserving squeezing, the second at high intensity for optimal state detection. A variable-duration microwave rotation about $\langle \mathbf{S} \rangle \propto \hat{x}$ between squeezing and detection (**C-D**) allows for readout of an arbitrary spin component in the yz-plane.[1]

To speed up the acquisition of data, we perform the sequence in Fig. 6-3 ten (10) times with the same atoms after each cycle of MOT loading and polarization gradient cooling. Over the course of the ten repetitions, the radial temperature increases by only $\sim 10\%$.

We demonstrate cavity feedback squeezing at fixed atom number $2S \approx 3.2 \times 10^4$ for various shearing parameters $Q = Sp\varphi^2$ by varying the photon number $2 \times 10^3 < p < 5 \times 10^5$. To characterize the geometry of the prepared state, we rotate it by a variable angle α about the mean spin vector $\langle \mathbf{S} \rangle$ before performing the readout of S_z. The dependence of normalized

---

[1]Because a rotation is required to observe the squeezed quadrature, cavity feedback squeezing places technical demands on phase stability that do not arise in measurement squeezing; but because the required rotation is small, the demands are less strict than those for applying the squeezing in a clock, which I discuss in detail in Ch. 7.

spin noise $\sigma^2 = 2\Delta S_z^2/S$ on α is shown in Fig. 6-4(a) for several representative shearing parameters Q, and each data set is fit with a sinusoidal curve. Qualitatively, the curves can be understood as follows: with increasing shearing, the angle of the major axis moves toward the xy-plane, corresponding to a decreasing angle α_0 at which the minimum variance occurs. At the same time, the minimum variance $\sigma_{\min}^2$ decreases, while the maximum variance $\sigma_{\max}^2$ grows. Since the data are plotted logarithmically, an area-preserving evolution would result in curves symmetric about $\sigma^2 = 1$. The observed asymmetry about $\sigma^2 = 1$ is primarily due to the phase broadening introduced by the photon shot noise of the intracavity light, which results in an increase in the uncertainty product $\sigma_{\min}^2 \sigma_{\max}^2$ with increasing Q. In addition, the minimum spin noise intrinsic to the prepared state is substantially augmented by technical noise of the readout, independently measured to correspond to a normalized spin variance $\sigma_{\rm ro}^2 = 0.13(1)$.

Quantitatively as well as qualitatively, the data agree with the theoretical predictions from Sec. 6.1, as Fig. 6-4(b) illustrates. The black dotted curves in Fig. 6-4(b) represent the model of Sec. 6.1, showing the ideal Q-dependence of the minimum and maximum spin variances $\sigma_{\min/\max}^2$ and of the inclination angle α_0. These follow the approximate scalings $\sigma_{\min}^2 \approx 2/(2+Q)$, $\sigma_{\max}^2 \approx 1 + 2Q + Q^2$, $\alpha_0 \approx 1/(2+Q)$ until encountering the curvature of the Bloch sphere at $Q_{\rm curv} \approx 80$. Extending the idealized model [12] to incorporate independently calibrated technical imperfections in our system results in the solid curves; these account for a reduction in the radius $\langle|\mathbf{S}|\rangle$ of the Bloch sphere with increasing p and for fluctuations in the intracavity photon number $n_c = c^\dagger c$ exceeding the photon shot noise by a factor $\gamma \equiv \Delta n_c^2/n_c \approx 1 + Q/74$ due to frequency noise of the laser. With no free parameters, this model provides a good description of the spin variances (blue diamonds and squares) and the angle α_0 (green triangles) characterizing the uncertainty ellipse. In particular, the agreement of $\sigma_{\min}^2 - \sigma_{\rm ro}^2$ with the adapted model demonstrates that the noise reduction by cavity feedback—in contrast to that conditioned on a measurement as in Ch. 5—can be as close to ideal as the intracavity intensity is close to photon-shot-noise-limited. Of course, the ability to benefit from that noise reduction—and hence the metrologically relevant squeezing—is additionally limited by the readout noise $\sigma_{\rm ro}^2$.

We quantify the cavity feedback squeezing by the parameter ζ_0 defined in Sec. 5.5. Figure 6-5 shows, as a function of photon number p or shearing parameter Q, the squeezing $\zeta_0 = \mathcal{C}(0)\sigma^2(p)/[\mathcal{C}(p)]^2$ deduced from the full measured normalized spin noise σ^2 and the contrast $\mathcal{C}$. (Note that the initial contrast $\mathcal{C}(0)$ is improved over that in Secs. 5.4-5.5 because the resonator locking light is now further detuned.) At an optimum $p = 4.1 \times 10^4$ ($Q = 19$), we achieve a $\zeta_0^{-1} = 5.6(6)$ dB enhancement in angular sensitivity, compared to that of a CSS with spin length $S\mathcal{C}(0)$, including not only the intrinsic noise of the state prepared by cavity feedback squeezing but also the detection noise. At $Q = 19$ we obtain a Wineland parameter $\zeta = \zeta_0/\mathcal{C}(0) = -4.6(6)$ dB, indicating that despite the contrast reduction due to the resonator locking light, we can expect to observe a 4.6(6) dB improvement in signal-to-
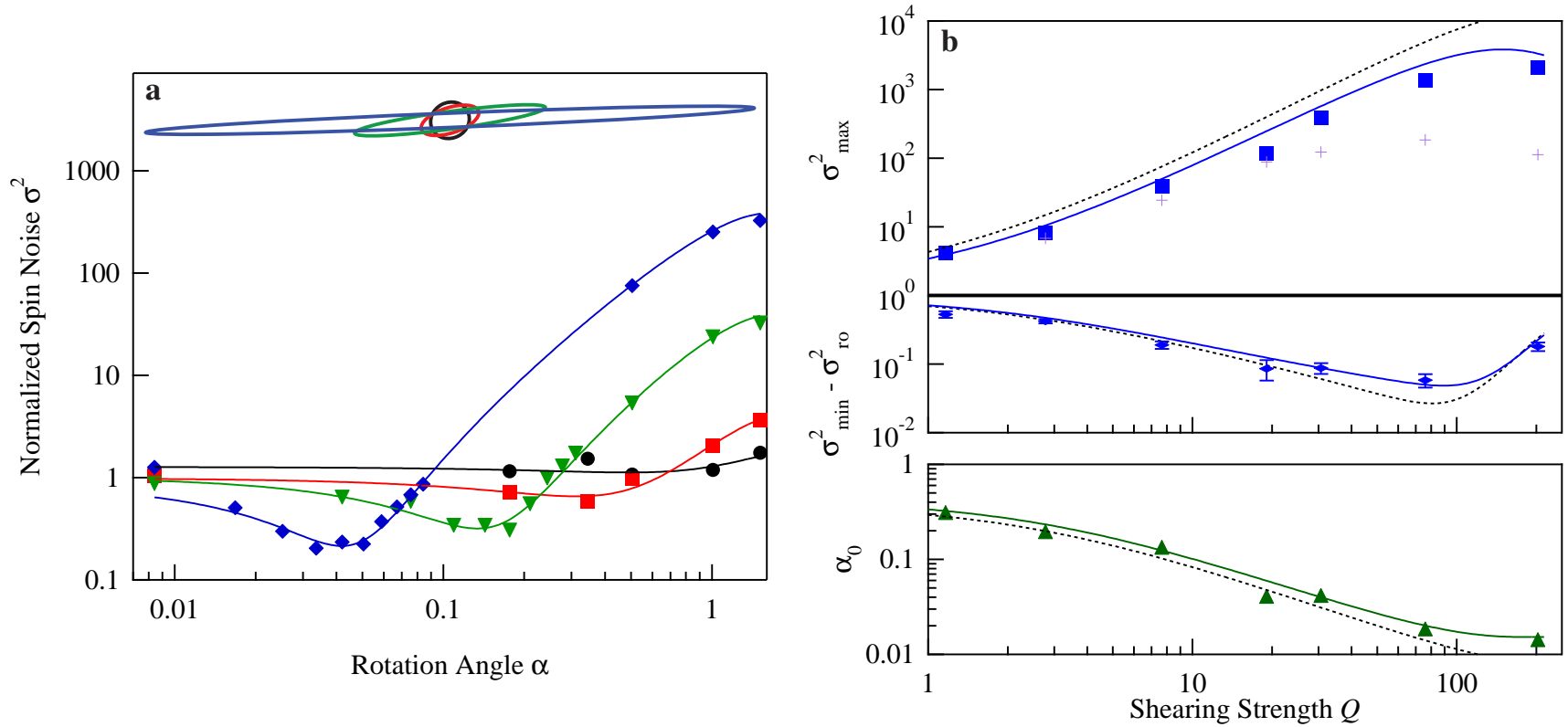
Figure 6-4: Geometry of the squeezed states prepared by cavity feedback, as determined by rotating each state by a variable angle α about the mean spin $\langle \mathbf{S} \rangle$ between squeezing and readout of S_z. The normalized spin variance $\sigma^2(\alpha) = 2\Delta S_z^2/S$ thus measured is shown in the left graph for shearing parameters $Q = 0$ (black), 1.2 (red), 7.7 (green) and 31 (blue); the ellipses in the inset are polar plots of $\sigma(\alpha)$ as given by the sinusoidal fits to the data. The maximum spin variance σ^2_{max}, minimum spin variance $\sigma^2_{\mathrm{min}} - \sigma^2_{\mathrm{ro}}$ with readout noise subtracted, and angle α_0 of the minor axis from $\hat{z}$ are summarized in the right graph and compared to both the idealized theory in Sec. 6.1 (black dotted curves) and a model accounting for contrast reduction and technical light noise (solid curves). The purple crosses show the maximum spin variance conditioned on the information in the detected squeezing light, as discussed in Sec. 6.4.

Figure 6-5: Cavity feedback squeezing results: normalized spin noise σ^2_{min} (blue diamonds), contrast $\mathcal{C}$ (gray squares), and squeezing ζ_0 (red triangles).

noise ratio over the Standard Quantum Limit for $N = 2S$ particles. We verify this directly in Ch. 7 by applying the state in an atomic clock.

A substantial portion of the observed spin noise $\sigma_{\min}^2$ is due to the imprecision $\sigma_{\mathrm{ro}}^2 = 0.13(1)$ of the readout measurement, indicated by the shaded blue region in Fig. 6-5. If we were able to detect it perfectly,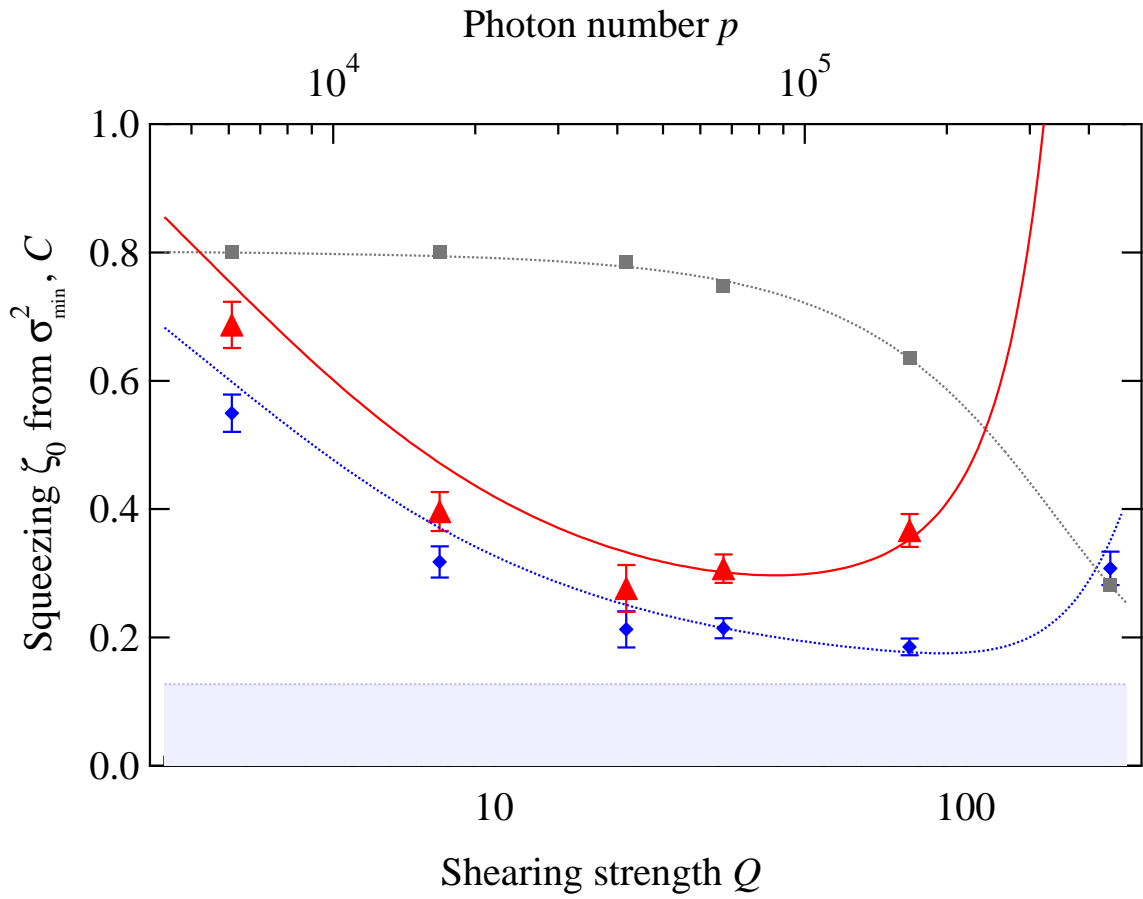 the state prepared at an optimum $Q = 76$ would enable an $\zeta^{-1} = \mathcal{C}^2/(\sigma_{\min}^2 - \sigma_{\mathrm{ro}}^2) = 8.4(7)$ dB improvement over the SQL, thanks to $\zeta_0^{-1} = 1/[\zeta\mathcal{C}(0)] = 10(1)$ dB of cavity feedback squeezing.

6.3   Multi-Partite Entanglement

The entanglement implied by $\zeta < 1$ can be further quantified by posing the following question [84]: if we express the ensemble spin state as a product of fully inseparable states, what is the largest number n of (effective) atoms that we are guaranteed to find in such a fully inseparable state? We can prove n-particle entanglement by evaluating theoretically the minimum achievable normalized spin noise σ_n^2 as a function of contrast $\mathcal{C}$ in a spin-$(n-1)/2$ system and demonstrating that our squeezed states violate this bound. Figure 6-6 shows calculated bounds on $\sigma_n^2(\mathcal{C})$ for various partition sizes $n-1$, reproducing the results of Sørensen and Mølmer [84]. The states prepared by cavity feedback squeezing (green diamonds, showing $\sigma_{\min}^2 - \sigma_{\mathrm{ro}}^2$) are characterized for $19 \leq Q \leq 76$ by at least 11-effective-atom entanglement, where each effective atom consists of on average 1.5 unentangled real atoms.

For comparison, Fig. 6-6 also shows the squeezed states prepared by QND measurement (purple triangles), where only bipartite entanglement is verifiable on the basis of the values σ^2 and $\mathcal{C}$ from Sec. 5.5. That deeper entanglement can be proved for the feedback-squeezed states is partly due to an overall improvement in contrast achieved by detuning the resonator locking light further from atomic resonance subsequent to the measurement squeezing experiments. In addition, however, cavity feedback allows a given noise reduction to be reached at lower photon number—and thus with greater preservation of contrast $\mathcal{C}(p)/\mathcal{C}(0)$—than does a measurement suffering from finite quantum efficiency and photodetection noise.

Note that in certain contexts, e.g. in the field of quantum information, the term "entangled" is restricted to describing states that are inseparable with respect to *separately addressable* particles or subsystems. Since our atoms are distributed across ~ 2000 wells of a one-dimensional lattice, small groups of atoms could be independently addressed by a laser incident from the side of the cavity. Thus, non-classical spin correlations between spatially separated groups of atoms could be directly verified in future experiments.
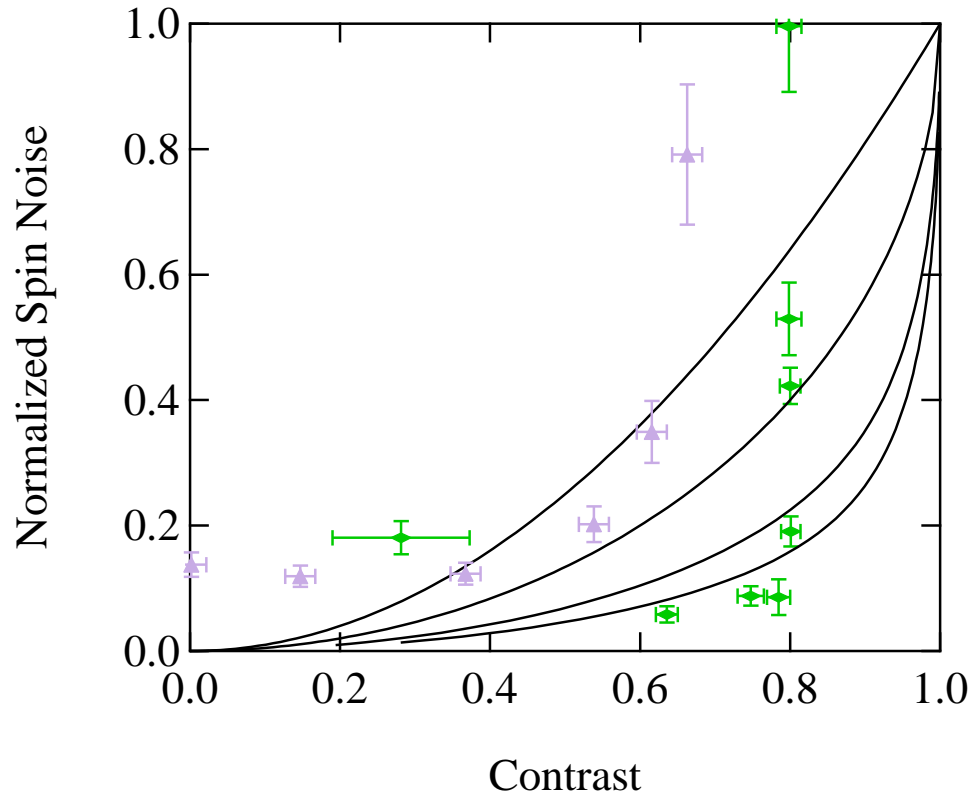
Figure 6-6: Normalized spin noise *vs.* contrast $\mathcal{C}$ for states prepared by either cavity feedback squeezing (green diamonds) or measurement squeezing (purple triangles) compared to lower bounds $\sigma_n^2(\mathcal{C})$ (black curves) on normalized spin noise for product states of spin-$(n-1)/2$ subsystems, were $n = 2, 3, 7$, or 11 (from top to bottom). The curve for $n = 2$ corresponds to $\zeta = \sigma^2/\mathcal{C}^2 = 1$, while the remaining curves are calculated in accordance with Ref. [84]. Data points falling below the curves demonstrate n-particle entanglement [84].

6.4 Outlook

We have shown that we are able to realize an effective one-axis twisting evolution that gives rise to spin squeezing, notwithstanding a net growth in uncertainty area. In the long term, however, it would be quite attractive to realize the true one-axis twisting Hamiltonian $H \propto S_z^2$. Beyond improving the scaling of fundamental limits to squeezing performance [12, 50], the unitary S_z^2 evolution would enable full quantum control over the space of symmetric ensemble spin states [51]. Achieving this evolution by cavity feedback requires either a Fock-state input field or—perhaps more realistically—quantum erasure of the information that leaves the cavity [12, 50].

To understand how such a quantum erasure scheme might work, consider first the *theoretically* simpler case of sending a Fock-state field into a one-sided cavity. That the latter gives rise to a unitary spin evolution can be understood quite intuitively. For a one-sided cavity, the intensity of the output light is independent of detuning, since all incident light—whether or not it enters the cavity—exits in a single mode; thus, information about the resonance frequency is carried only in the *phase* of the output light. Since a Fock state can carry no phase information, it cannot reveal the cavity resonance frequency or the shift of that frequency by the atoms. Since it allows no measurement of the atomic state, it need not impart any back-action broadening—and indeed it *does* not, because it is free of photon shot noise.

By extension, if the input field is instead in a coherent state, one can erase the information in the phase of the light by counting the exiting photons with high quantum efficiency,[2] and based on the count one can reverse the photon-shot-noise-induced fluctuations in the atomic phase. Already in our present system, detection of the squeezing light substantially reduces the phase broadening in Fig. 6-4 (purple crosses), but at large Q the uncertainty product remains an order of magnitude above the Heisenberg product. In light of the challenges of more perfect detection, one might alternatively arrange for the light to interact with the atoms twice in such a way that the atomic information encoded in the field during the first pass is erased during the second [50].

Such quantum erasure would allow cavity feedback to prepare non-Gaussian states, since interference fringes can arise when the spin quasiprobability distribution twists all the way around the Bloch sphere. To investigate the potential for producing non-Gaussian states, I apply a powerful result derived in the thesis of Ian Leroux: that a Fock state $|p_{\text{in}}\rangle$ of p_{in} photons incident on a one-sided cavity, at a half-linewidth detuning from cavity resonance as above, produces a unitary transformation $U(p_{\text{in}}) = \exp[i\mathcal{H}(S_z)p_{\text{in}}]$ of the spin subsystem, where

$$\mathcal{H}(S_z) = \varphi S_z + \varphi^2 S_z^2/2 + \mathcal{O}(\varphi^3) \tag{6.16}$$

---

[2]Note that for a two-sided cavity, the two output modes must first be appropriately recombined on a beam-splitter.

in terms of $\varphi = 2\Omega/\kappa$. Based on this result, we can further calculate the (non-unitary) transformation of the atomic density matrix elements $\rho_{m,m'}$—where m, m' represent eigenvalues of S_z—produced by an arbitrary field state $|\Phi\rangle$ by expanding the field state in the Fock-state basis:

$$\rho_{m,m'} \longrightarrow F_\Phi^*[\mathcal{H}(m)]F_\Phi[\mathcal{H}(m')]\rho_{m,m'}, \tag{6.17}$$

where $F_\Phi(u) \equiv \sum_{p_{\text{in}}} |\langle\Phi|p_{\text{in}}\rangle|^2 \exp(\mathrm{i}p_{\text{in}}u)$ is the characteristic function of the photon number distribution. I apply Eq. 6.17 to plot Wigner functions of the spin state [85–87] produced by the cavity feedback dynamics arising from input fields with various photon number statistics interacting with atoms initially in a CSS along $\hat{x}$. Figure 6-7 shows results for a system of $2S = 20$ atoms in a one-sided cavity driven by a field in a Fock state (top), a coherent state (bottom), or a Gaussian state squeezed by 10 dB (middle); the squeezed field state simulates a quantum erasure scheme with 90% fidelity. The (mean) incident photon number $\overline{p_{\text{in}}}$ is chosen to produce a phase difference $\overline{p_{\text{in}}}\mathcal{H}(m) - \overline{p_{\text{in}}}\mathcal{H}(m + \Delta m) = \pi$ either across the width of the CSS uncertainty region $\Delta m = \sqrt{S/2}$ (left column) or between adjacent Dicke levels $\Delta m = 1$ (right column). The latter ideally produces a Schrödinger cat state (top right), i.e., an eigenstate of the parity of S_y; however, producing such a state in practice would require not only quantum erasure but also ultra-strong coupling $\eta \gtrsim S$. The states in the left column, on the other hand, might be attained with "only" strong coupling ($\eta > 1$). Intriguingly, the Wigner function takes on negative values (blue)—a signature of non-classicality not attainable by squeezing alone—even in the state produced by a coherent input field.

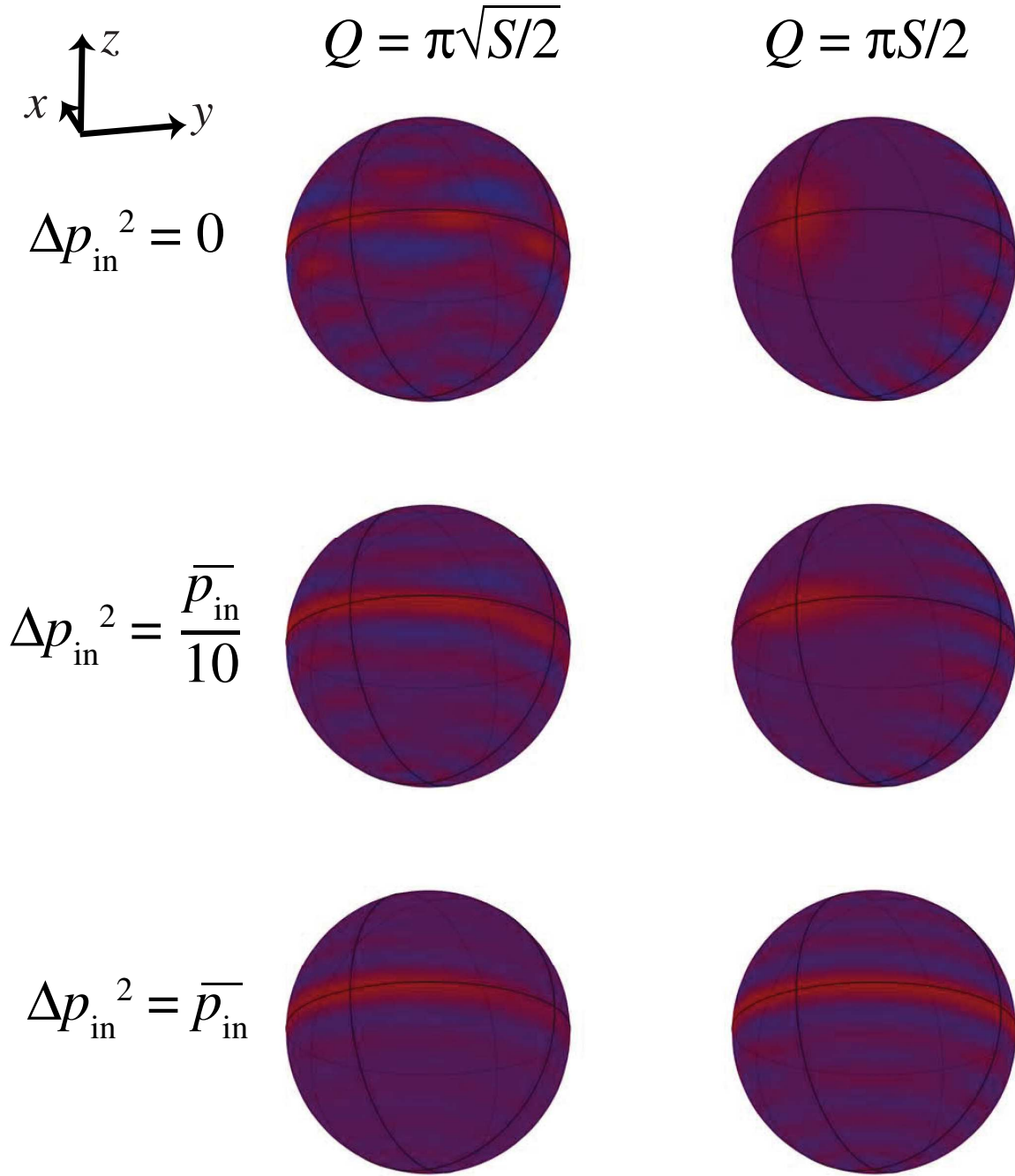Figure 6-7: Outlook toward preparing non-Gaussian states by cavity feedback. Shown are Wigner functions for the collective spin of $2S = 20$ atoms, for two different values of $Q = S(\overline{p_{in}}/2)\varphi^2$, where $\overline{p_{in}}$ is the mean photon number in the light pulse incident on a one-sided cavity. The three rows illustrate the effects of different photon number variances Δp_{in}^2.

Chapter 7

A Squeezed Atomic Clock

> *The romance of the precise is not the elision*
> *Of the tired romance of imprecision.*
> *It is the ever-never-changing same,*
> *An appearance of Again, the diva-dame.*
> —Wallace Stevens, "Adult Epigram."

The stability of an atomic clock is characterized by the Allan deviation $\sigma(\tau)$, which describes the fractional uncertainty in the clock transition frequency ω after measuring it repeatedly over a total time τ and averaging the results of these independent measurements. At the standard quantum limit, a single measurement of duration (e.g., Ramsey precession time) T using N atoms has (recalling Eq. 1.1) a fractional frequency uncertainty $\Delta\omega/\omega = 1/(\sqrt{N}\omega T)$. A clock operating at the SQL [1] with a cycle time T_{cyc} thus achieves an Allan deviation

$$\sigma_{\text{SQL}}(\tau) = \frac{1}{\sqrt{N}\omega T}\sqrt{\frac{T_{\text{cyc}}}{\tau}} \tag{7.1}$$

by averaging the results of the τ/T_{cyc} measurements performed in the total time τ. In this chapter, I will present the first demonstration of an Allan deviation beyond the standard quantum limit.

Our approach to performing Ramsey spectroscopy beyond the SQL [43,53] is illustrated in Fig. 7-1, where the red arrows indicate microwave-induced rotations on the Bloch sphere. The top panel shows an ordinary Ramsey sequence using a coherent spin state (CSS), whereas the center panel shows a modified Ramsey sequence incorporating a squeezed state prepared by cavity feedback (Ch. 6). The standard Ramsey sequence takes as its input a CSS oriented along $-\hat{z}$ (i.e., an ensemble optically pumped into $|\downarrow\rangle$). A $\pi/2$ pulse rotates this CSS into the xy plane, giving it a well-defined phase relative to the microwave oscillator and thereby starting the clock. The objective of the squeezed Ramsey sequence is to begin the precession with an even better defined phase. This requires prefatory steps of preparing (similarly) a CSS in the xy plane and applying probe light (dashed blue arrow) to shear it
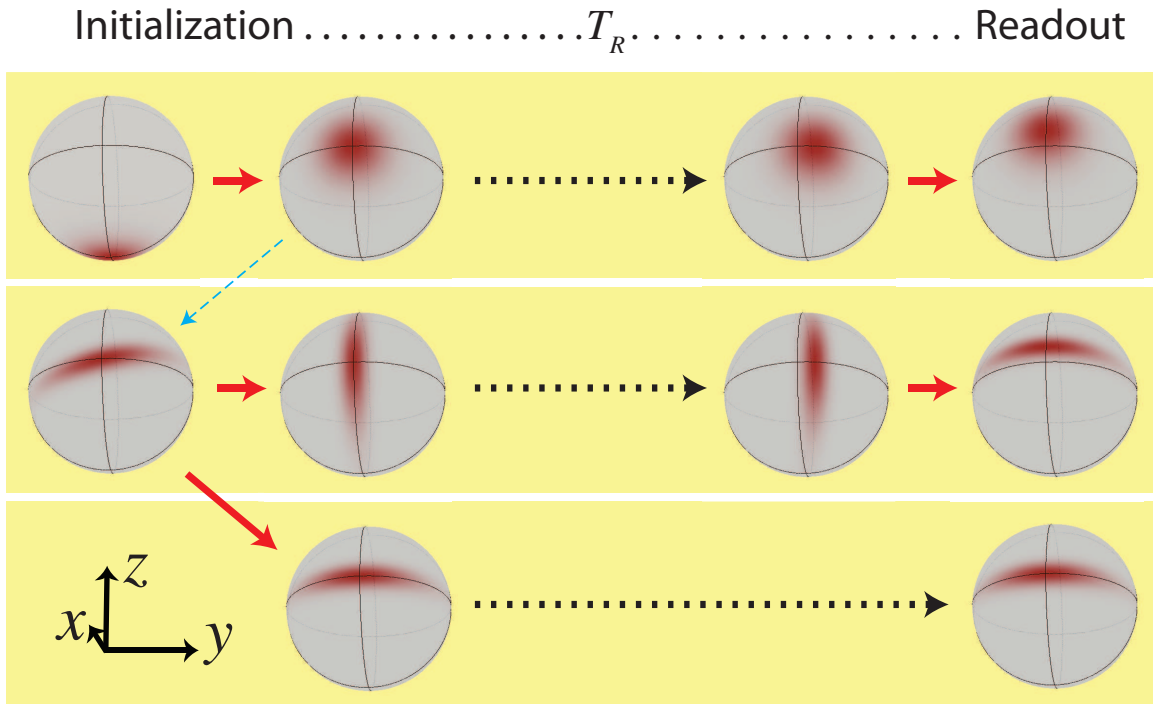
Figure 7-1: Comparison of a conventional Ramsey sequence performed with a coherent spin state (CSS; top panel) with a modified Ramsey sequence incorporating a squeezed spin state (central panel). Bold red arrows indicate microwave rotations. The spin squeezing (dashed blue arrow) is prefaced by preparation of a CSS along $\hat{x}$ equivalent to the initialization step of an ordinary Ramsey sequence; however, the modified Ramsey sequence only measures the phase acquired subsequent to a near-$\pi/2$ rotation that places the squeezed state into the phase-squeezed orientation. Conversely, sensitivity of the squeezed quadrature to phase fluctuations is minimized by placing the state into the number-squeezed orientation (bottom panel).
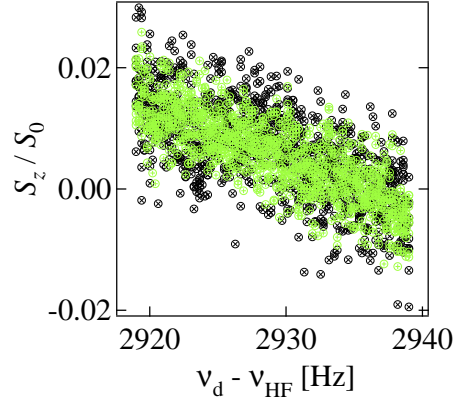
Figure 7-2: A small portion of a Ramsey fringe obtained with either a CSS (black) or a squeezed state (green). The abscissa $\nu_d - \nu_{\mathrm{HF}}$ represents the detuning of the microwave oscillator from the free-space $|F = 1, m_F = 0\rangle \rightarrow |F = 2, m_F = 0\rangle$ transition. In this particular data set, the squeezed state outperforms the unentangled state by 3.2 dB in signal-to-noise ratio.

into a state that is at a small angle $\alpha_0 \ll 1$ from a number-squeezed orientation, as described in Ch. 6. Rotating this squeezed state by $\pi/2 - \alpha_0$ into the phase-squeezed orientation starts the clock. With or without squeezing, the Ramsey sequence concludes with a $\pi/2$ pulse to convert the acquired phase into a population difference $2S_z$, which we read out by our standard cavity transmission measurement. A small portion of a Ramsey fringe thus obtained, showing the dependence of the final spin projection on the microwave drive frequency after a $T = 200\ \mu$s precession, is plotted in Fig. 7-2 for the case of either a coherent (black) or squeezed (green) input state of spin $S = 1.6 \times 10^4$. In this particular example, the signal-to-noise ratio of the squeezed clock is 3.2(2) dB higher than that achieved with the CSS.

7.1 Technical Aspects

Even reaching the standard quantum limit in a clock [1]—let alone surpassing it—places stringent technical demands. In particular, in order to operate a stable clock, it is critical to minimize all sources of classical phase noise. Note, for comparison, that such phase noise has no effect on the squeezed quadrature (S_z) of the state prepared by measurement squeezing; and its effect on a state prepared by cavity feedback squeezing is suppressed by the small angle $\alpha \ll 1$ of this state from the number-squeezed orientation. Yet as soon as a squeezed state is rotated into the phase-squeezed orientation to initiate a Ramsey sequence (see Fig. 7-1), it starts performing its function as an exquisitely sensitive detector of any fluctuations $\Delta\omega_{\mathrm{tech}}$ in the frequency of the clock transition or fluctuations $\Delta\phi_{\mathrm{tech}}$ in the phase of the reference oscillator. These fluctuations must be kept very small ($\Delta\omega_{\mathrm{tech}}T \ll$

$1/\sqrt{N}, \Delta\phi_{\text{tech}} \ll 1/\sqrt{N}$) in order for a Ramsey measurement with precession time T to be limited by the intrinsic quantum noise of even a CSS, let alone a squeezed state.

The microwave oscillator's phase fluctuations are specified as a value $L(f)$ in dBc/Hz representing the noise level relative to the carrier at an offset frequency f from the carrier. For these classical phase fluctuations, averaged over a microwave pulse of duration T_μ, to be smaller than the coherent-state phase variance of N atoms requires $L < L_{\text{CSS}} \equiv 10 \log[T_\mu \times \text{Hz}/(4N)]$. In our experiments, with a $\pi/2$ pulse duration of 30 μs and atom number up to $N \approx 4 \times 10^4$, we therefore require a phase noise $L(f) \ll L_{\text{CSS}} \approx -91$ dBc/Hz at frequencies $f \gtrsim T^{-1}$ in order to approach the SQL in a Ramsey sequence with precession time T, and correspondingly lower phase noise for a squeezed clock. The microwave synthesis chain described in Sec. 3.5 satisfies this requirement, the 6.8 GHz oscillator's phase noise being specified at $L(f) < -130$ dBc/Hz at $f = 10$ kHz.

Although we operate with the very same atomic transition ($|F = 1, m_F = 0\rangle \rightarrow |F = 2, m_F = 0\rangle$) used in ^{87}Rb fountain clocks, its function as a "clock transition" is severely degraded by our use of an optical dipole trap. Since there exists no magic wavelength for the ^{87}Rb hyperfine transition—i.e., no trapping wavelength where the two clock states experience equal light shifts—we instead employ the magic polarization trick introduced in Sec. 3.3 to minimize trap-induced fluctuations and broadening of the clock transition frequency ω. This trick requires a combination of elliptically/circularly polarized trap light and a magnetic bias field $\mathbf{B}$, and therefore comes at the expense of introducing a magnetic-field sensitivity $d\omega/dB = 2\beta_{\text{QZ}}B$, where $\beta_{\text{QZ}} = 575$ Hz/G^2 quantifies the quadratic Zeeman shift [13]. The requisite magnetic bias field (and hence $d\omega/dB$) is minimized by choosing full circular polarization for the trap, which moreover likely minimizes any effects of polarization noise. The net result, in our trap of depth $U_0 = 2\pi \times 18(6)$ MHz with a bias field $B = 2.4$ G, is a sensitivity $U_0 d\omega/dU_0 \approx 2$ Hz/% to percent fluctuations in trap depth, combined with a 3 Hz/mG sensitivity to magnetic field fluctuations. Our apparatus contains no magnetic shielding, but we do take care to synchronize the experiment to the 60 Hz AC power line.

The classical frequency noise described above limits the Ramsey precession time for which we can observe quantum-limited performance of even an unentangled clock. Nevertheless, as we shall see in Fig. 7-2 below, the classical noise is sufficiently low that there is an experimentally accessible regime where we can observe a benefit from squeezing.

7.2 Squeezing Lifetime

To what extent squeezing can benefit practical metrological applications has been a subject of numerous theoretical studies [20,88,89], as entangled states are notorious for their fragility in the face of environmental perturbations. If an entanglement-induced enhancement in phase resolution comes at the cost of a restriction on precession time to avoid decoherence,

it will not necessarily allow a more precise frequency determination in a fixed time. Thus, metrology—and particularly clocks—can profit from entangled states that are relatively robust to environmental perturbations [88].

We investigate the robustness of a squeezed state by directly comparing its performance to that of a coherent spin state in Ramsey spectroscopy with variable precession time T. We quantify the performance in each case by the Wineland parameter $\zeta = 2S\Delta S_z^2/\mathcal{C}^2$ at the end of the sequence, performed with $2S = 3 \times 10^4$ atoms. The interference contrast $\mathcal{C} = |\langle S_x \rangle|/S$ is measured by varying the phase of the final $\pi/2$ pulse in the Ramsey sequence and fitting the resulting interference fringe. Fig. 7-3 shows ζ vs T as measured using either a coherent spin state (black solid circles) or a squeezed state (red solid diamonds). Each dataset is well described by a model of the form

$$\frac{\zeta(T)}{2S} = \Delta\phi_{\mathrm{Q}}^2 + \Delta\phi_{\mathrm{Cl}}^2 \tag{7.2}$$

that describes a state-dependent initial phase variance $\Delta\phi_{\mathrm{Q}}^2$ due to quantum fluctuations (and detection noise) which, with increasing precession time, is overwhelmed by a classical phase variance $\Delta\phi_{\mathrm{Cl}}^2 = \Delta(\omega T)^2$ due to fluctuations $\Delta\omega^2 = (2\pi \times 1.3~\mathrm{Hz})^2$ of the clock transition frequency. The latter are attributable to sub-mG magnetic field fluctuations (see Sec. 7.1).

While the classical phase perturbations are detectable ($\Delta\phi_{\mathrm{Cl}}^2 \gtrsim \Delta\phi_{\mathrm{Q}}^2$) sooner with a phase-squeezed state than with a CSS, there is no evidence that these perturbations degrade the metrological usefulness of the state. Rather, Eq. 7.2 suggests that the quantum and classical phase fluctuations are independent and uncorrelated. In this case, if the classical perturbation $\Delta\phi_{\mathrm{Cl}}$ were precisely what we were trying to measure, I claim that the squeezed state would allow us to measure it to better than the standard quantum limit by the factor $\zeta(0) = 2S\Delta\phi_{\mathrm{Q}}^2 < 1$, even for precession times T where the classical phase variance results in a final Wineland parameter $\zeta(T) > 1$. However, in order to directly test this claim, we would require an independent measure of $\Delta\phi_{\mathrm{Cl}}$.

Even without independently measuring the classical perturbations $\Delta\phi_{\mathrm{Cl}}$, we can demonstrate that their effect on the squeezed state is largely reversible. We do so by adding a $\tilde{\pi}$ pulse (composite π pulse, as defined in Sec. 4.4.2) halfway through the Ramsey sequence to cancel the effect of any frequency deviation $\Delta\omega$ that is fixed over the duration T. This spin echo procedure (green triangles in Fig. 7-3) extends the time for which the state remains demonstrably squeezed ($\zeta(T) < 1$) from $\sim 500\mu$s to ~ 2 ms by removing up to 96% of the classical phase variance. The reversibility of the classical phase noise assures us that the squeezed state, while sensitive at detecting phase perturbations, is not destroyed by them.

The detectable squeezing persists even longer if, rather than performing a Ramsey sequence, one directly rotates the state prepared by cavity feedback into the number-squeezed orientation, as illustrated in the bottom panel of Fig. 7-1. The open blue diamonds in Fig.

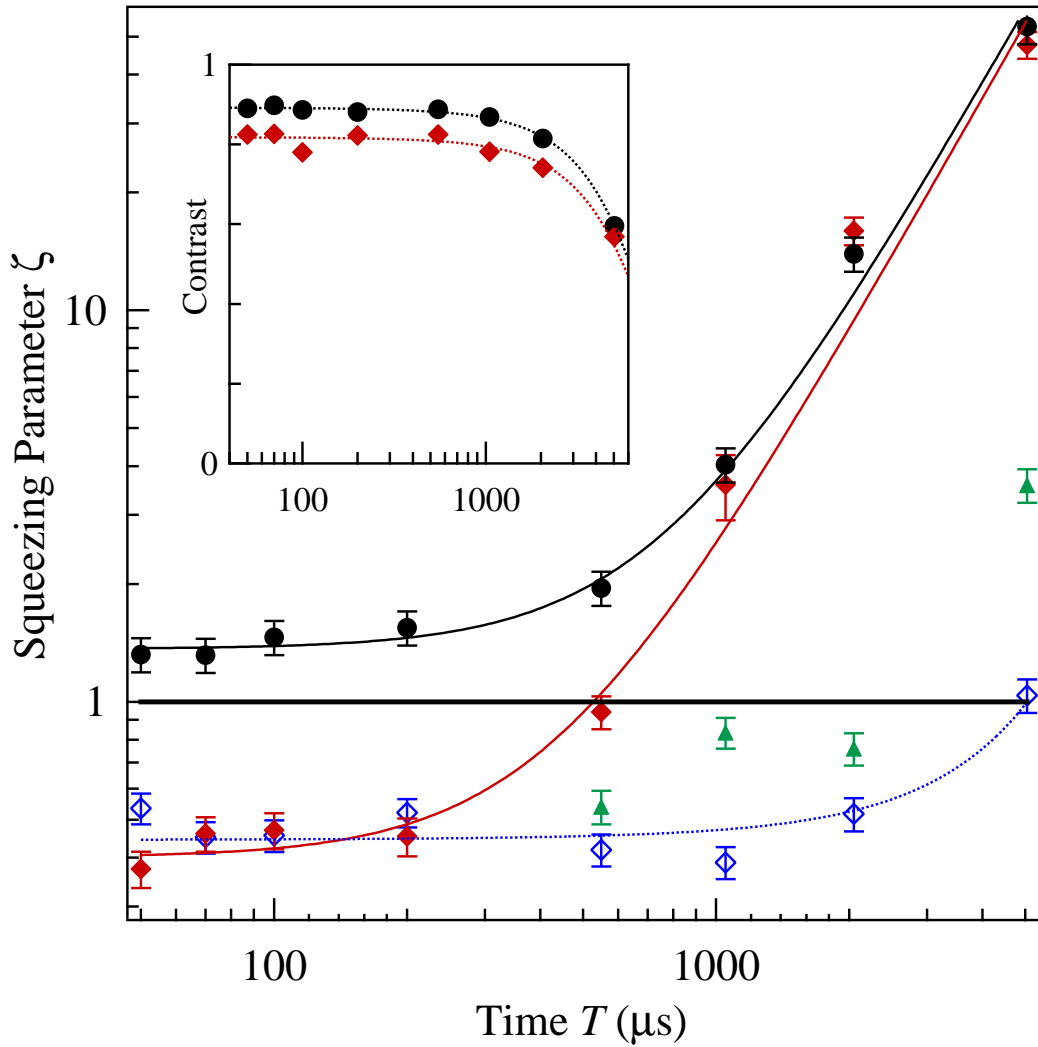Figure 7-3: Squeezing parameter ζ measured at the end of a Ramsey sequence as a function of precession time T for either a squeezed state (solid red diamonds) or a coherent spin state (solid black circles). Also shown is ζ for a state that is simply placed in the number-squeezed orientation, as a function of time T before readout. Inset: interference contrast $\mathcal{C}$ vs. precession time T.

7-3 show the squeezing parameter ζ as a function of delay time T before reading out S_z. The eventual degradation in squeezing over a time $T_2^* \sim 5$ ms is fully accounted for by a reduction in interference contrast $\mathcal{C}$ (solid blue diamonds in inset) due to inhomogeneous broadening,[1] as illustrated by consistent fits to $\mathcal{C}(T)$ (dotted red curve in inset) and $\zeta(T) \propto [\mathcal{C}(T)]^{-2}$ (dotted blue curve).

To the extent that we are able to assess, then, the squeezed state is sufficiently robust as to always either equal or outperform the unentangled state in Ramsey spectroscopy. Moreover, it is only because our measurement ceases to be quantum-limited at long precession times T—because of classical noise in our laboratory that is indistinguishable from the signal of interest—that the Wineland parameter ζ asymptotically approaches that of the CSS in the limit of long precession time. Given a measurement that is quantum-limited at a precession time $T < T_2^*$ set by some external constraint—or by a desired measurement bandwidth—squeezing can be expected to enhance the measurement performance (see Sec. 7.4).

7.3 Allan Deviation

We characterize the short-term stability of our squeezed clock, operating with $N = 3.5 \times 10^4$ effective atoms, by measuring its Allan deviation. In order that the squeezing not be obscured by the classical noise in our system, we set a short Ramsey precession time of $T = 200$ μs. Given N, T and our $T_{\text{cyc}} = 9$ s experiment cycle, the best stability that we could possibly achieve with the atoms in an uncorrelated state is (by Eq. 7.1) $\sigma_{\text{SQL}}(\tau) = 1.9 \times 10^{-9}$ Hz$^{-1/2}\tau^{-1/2}$, where τ represents the total averaging time. This standard quantum limit on the Allan deviation is indicated by the solid black line in Fig. 7-4. The Allan deviation we actually measure with an ordinary Ramsey sequence using a CSS (open black circles in Fig. 7-4) is somewhat worse than the SQL. Nevertheless, with the modified Ramsey sequence incorporating a squeezed state, we achieve a fractional frequency stability $\sigma(\tau) = 1.1 \times 10^{-9}$ Hz$^{-1/2}\tau^{-1/2}$ for averaging times τ up to 50 s, representing a 4.7(5) dB improvement over the standard quantum limit.

7.4 Outlook

Our demonstration of an Allan deviation beyond the standard quantum limit is so far a proof of principle. The fractional frequency stability of $\sigma(\tau) = 1.1 \times 10^{-9}$ Hz$^{-1/2}\tau^{-1/2}$ is nothing to brag about in absolute terms [14], but it could be improved by several orders of magnitude merely by extending the Ramsey precession time beyond its current 200 μs. Atomic phase coherence times of 1 s or more are readily achievable in trapped-atom systems

---

[1]The dominant limitation on the coherence time is most likely an inhomogeneous light shift from the lock laser carrier; see Sec. 3.4.
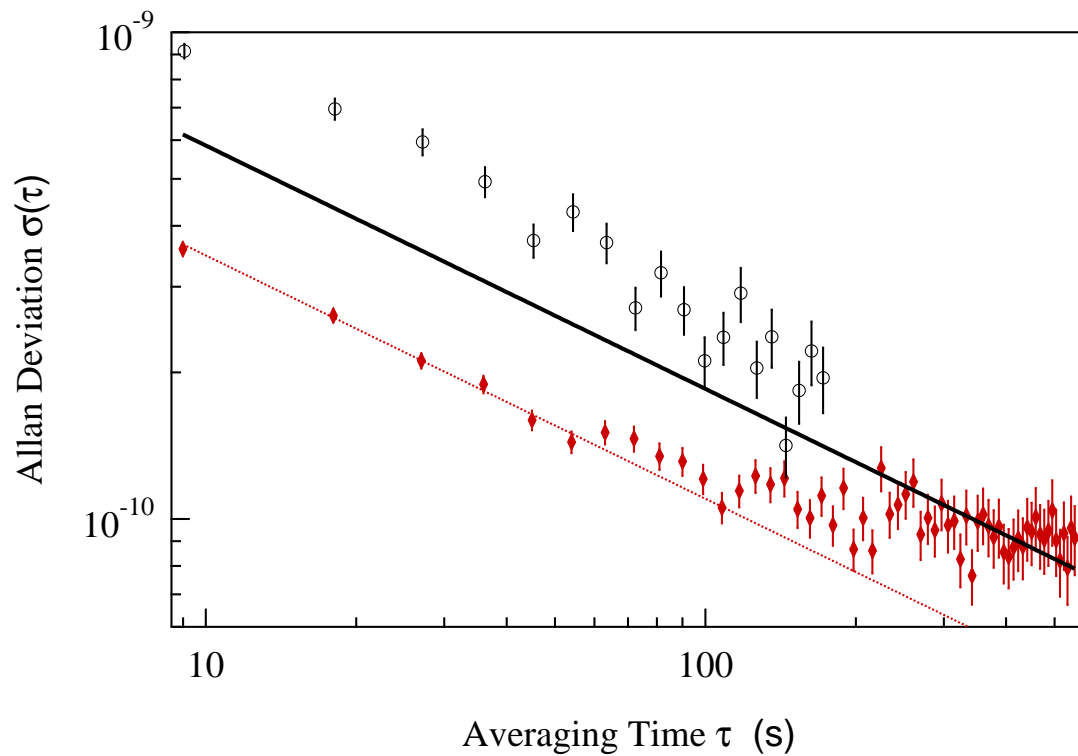
Figure 7-4: Allan deviation of a squeezed clock (red diamonds) compared to the standard quantum limit (solid black line) and to the actual performance of an unentangled state in our system (black circles).

amenable to spin squeezing, including both microwave clocks with magnetically trapped ^{87}Rb atoms [90, 91] and optical-transition clocks in magic-wavelength lattices [15–17, 92].

Optical-transition clocks, where the interrogation time T is typically limited by the phase coherence time of the interrogating laser rather than that of the atoms [15, 17], present precisely the scenario where spin squeezing is most apt to be profitable [89] for measurements of time. At fixed T, as these clocks approach the standard quantum limit [15], their stability can in principle be improved either by spin squeezing or by increasing atom number. However, the latter solution may be precluded by the density shift—already a dominant systematic effect [16, 92]. Thus, spin squeezing will be a compelling approach to continuing to advance the performance of these state-of-the-art clocks [93].

In a broader context, squeezed Ramsey spectroscopy can benefit high-bandwidth sensing applications, including accelerometry and magnetometry, simply by delivering a quantum speed-up in the time to reach a fixed measurement precision. Our method might even be extended to perform sensitive measurements with high spatial resolution by squeezing and interrogating multiple sub-ensembles in a single cavity.

Chapter 8

Collective cavity cooling

The dispersive coupling of atoms to a cavity can be used to manipulate not only the atoms' internal (spin) but also their external (motional) degrees of freedom. Whereas the former can dynamically produce spin squeezing (Ch. 6), the latter can give rise to cavity cooling [11,62,94–101] or other optomechanical effects [102–107]. In our spin squeezing experiments, we worked at sufficiently low photon scattering rates that the mechanical effects of the light were negligible. Now, we remove the spin-dependent interaction—by keeping all atoms in a single internal state—and increase the photon scattering rate to investigate cavity cooling.

Cavity cooling [11, 62, 94–96] is unique among laser cooling techniques in that it is applicable, in principle, to arbitrary scatterers of light. The spectrum of the scattering, which governs the rate of change of the scatterer's energy, is controlled by the cavity resonance [11] rather than by an atomic one. Cavity cooling thus offers enticing prospective applications, from preparation of ultracold molecular gases [108, 109] to continuous cooling of qubit registers [110]. In experiments to date [97–101], cavity cooling of one atom [97–99] or ion [100] is well described by a semiclassical model [11, 62]. Less well understood is the case of an ensemble, where the coupling of many particles to a single cavity mode yields nontrivial collective dynamics [101–107], such as enhanced cooling of the center-of-mass motion [102].

Ensemble cavity cooling (Fig. 8-1) thus differs markedly from conventional laser cooling, where emission into a plethora of free-space field modes allows for simultaneous and independent cooling of all atoms, or equivalently, all motional degrees of freedom of the ensemble. In cavity cooling, a single collective motional mode $\mathcal{X}$ can be defined that is maximally coupled to the cavity [106], while all other orthogonal ensemble modes are decoupled from the cavity due to destructive interference in the light scattering from different atoms. The coupling of $\mathcal{X}$ to the cavity is cooperatively enhanced by constructive interference in proportion to atom number [102, 108], allowing mode $\mathcal{X}$ to be cooled faster—and to lower temperatures—than a single atom. For sympathetic cooling of single-particle degrees of freedom, mixing between $\mathcal{X}$ and other ensemble modes might be introduced by an anharmonic or inhomogeneous trapping potential, or by collisions.

The collective cooling itself is most readily studied in the limit of weak mixing. Here,
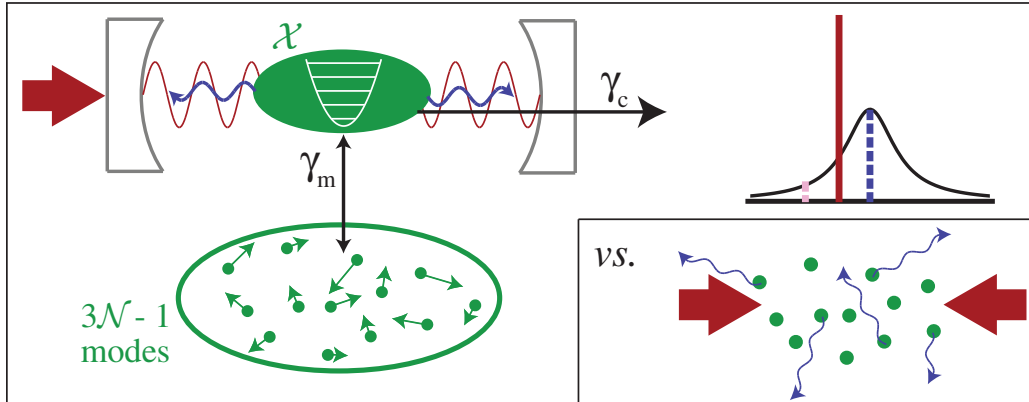
97

Figure 8-1: Ensemble cavity cooling. A probe laser (red) is placed at red detuning from cavity resonance to enhance anti-Stokes scattering into the cavity (blue), which cools a single collective mode $\mathcal{X}$ (solid green oval) at a cooperatively enhanced rate γ_c. Single-particle modes can only be cooled by mixing (at rate γ_m) with $\mathcal{X}$. This differs from ordinary laser cooling (inset), where free-space emission causes the atoms to be cooled independently.

cavity cooling is equivalent to the single-mode optomechanical cooling [111–113] of macroscopic mechanical oscillators [114–119]. The analogy with optomechanics [105, 106] has recently enabled quantitative studies of backaction-induced heating [106] and optomechanical frequency shifts [107] in an ensemble-cavity system. Yet the implications for cavity cooling have not been experimentally investigated, and the quantitative understanding of ensemble cooling [95, 108] has remained incomplete.

In this chapter, I present direct observations of the relevant collective mode $\mathcal{X}$ of our trapped atomic ensemble during cavity cooling. By studying the rate of cooling as a function of photon scattering rate and atom number, I demonstrate that the cooling relies on the cooperative emission of light by the ensemble. The cooling is well described by adapting an optomechanical model [112] to our system, where the mechanical oscillator $\mathcal{X}$ has a 500 kHz frequency, very small mass $M = (10^{-23} - 10^{-21})$ kg, and comparatively low quality factor $Q = 19$. I verify the agreement with optomechanical theory for a wide range of collective-mode occupation numbers up to $\langle n \rangle \sim 10^3$, and I demonstrate cooling down to a mean phonon number $\langle n \rangle_{\text{min}} = 2.0^{+0.9}_{-0.3}$, close to the theoretical limit for our parameters.

8.1   Theory

The optomechanical interaction in our system arises from a position-dependence of the dispersive coupling of atoms to the standing-wave cavity mode. Consider an idealized Hamiltonian H_{sys} describing an ensemble of $\mathcal{N}$ atoms that are harmonically trapped, with identical trap frequencies ω_t, at various positions ξ_i along the cavity axis. For dispersive coupling of the atoms to a cavity mode (the probe mode) of frequency ω_c with annihilation operator $\hat{c}$ and wavenumber k, assuming a large probe-atom detuning Δ relative to the

excited-state linewidth Γ, we have

$$H_{\text{sys}} = \sum_{i=1}^{\mathcal{N}} \left[\frac{1}{2} m\omega_t^2 (\hat{x}_i - \xi_i)^2 + \frac{\hat{p}_i^2}{2m} + \hbar\Omega_0 \sin^2(k\hat{x}_i)\hat{c}^\dagger\hat{c} \right] + \hbar\omega_c\hat{c}^\dagger\hat{c}. \tag{8.1}$$

Here, $\Omega_0 = g_0^2/\Delta$—with vacuum Rabi frequency $2g_0$—represents the dispersive shift of the cavity resonance due to a single atom at an antinode, or equivalently, the ac Stark shift experienced by such an atom per intracavity photon. In the Lamb-Dicke regime, where the deviation $\tilde{x}_i \equiv \hat{x}_i - \xi_i$ of each atom from the local trap minimum at ξ_i satisfies $\langle (k\tilde{x}_i)^2 \rangle \ll 1$, the optomechanical interaction term can be expressed in terms of a single collective position variable

$$\hat{X} \equiv \mathcal{N}^{-1} \sum_{i=1}^{\mathcal{N}} \sin(2k\xi_i)\tilde{x}_i. \tag{8.2}$$

The momentum conjugate to $\hat{X}$ is expressed in terms of the single-atom momenta $\hat{p}_i$ as $P = \mathcal{N} \sum_{i=1}^{\mathcal{N}} \sin(2k\xi_i)\hat{p}_i / \sum_{i=1}^{\mathcal{N}} \sin^2(2k\xi_i)$, such that $\hat{X}$ and $\hat{P}$ obey the canonical commutation relation $[\hat{X}, \hat{P}] = i\hbar$. To describe the full motion of the $\mathcal{N}$-atom ensemble, one can construct an orthogonal basis comprising $\hat{X}$, $\hat{P}$, and additional coordinate pairs representing $3\mathcal{N} - 1$ other modes of ensemble motion with energy $H_\perp$; in this basis, the system Hamiltonian takes the form

$$H_{\text{sys}} = \frac{1}{2} M\omega_t^2 \hat{X}^2 + \frac{\hat{P}^2}{2M} + \hbar \left(\omega_c + \delta\omega_c + \mathcal{G}\hat{X} \right) \hat{c}^\dagger\hat{c} + H_\perp, \tag{8.3}$$

where $M = m\mathcal{N}^2 / \sum_{i=1}^{\mathcal{N}} \sin^2(2k\xi_i)$ represents the effective mass of the collective harmonic oscillator mode $\mathcal{X}$ described by $\hat{X}$ and $\hat{P}$, in terms of the single-atom mass m. While $\delta\omega_c = \Omega_0 \sum_{i=1}^{\mathcal{N}} \sin^2(k\xi_i)$ represents the overall shift of the cavity resonance due to the atoms, the term

$$H_{\text{om}} = \hbar\mathcal{G}\hat{X}\hat{c}^\dagger c, \tag{8.4}$$

represents the canonical optomechanical interaction [111–113] describing a cavity frequency shift $\mathcal{G}\hat{X}$ proportional to $\hat{X}$, or equivalently, an intensity-dependent force on the collective mode with strength $\hbar\mathcal{G} = \mathcal{N}\hbar\Omega_0 k$ per photon.

For a probe laser detuned from the cavity line of width κ, small shifts $|\mathcal{G}\hat{X}| < \kappa$ yield proportional changes in intracavity and transmitted power. The $\hat{X}$-dependent transmission can be used to monitor mode $\mathcal{X}$, while the $\hat{X}$-dependent changes in intracavity intensity— delayed by the cavity response—induce cooling or heating: the delay converts the position-dependent into a velocity-dependent force that damps or amplifies the collective motion depending on the sign of the laser-cavity detuning [11, 62]. (Note that the cavity cooling dynamics induced by $H_{\text{om}} \propto \hat{X}\hat{c}^\dagger c$ differ from the cavity feedback squeezing induced by $H \propto S_z\hat{c}^\dagger c$ only because of the oscillatory motion of $\hat{X}$, which makes the cavity delay become relevant.)

In the frequency domain, cavity cooling can be understood as arising from unequal scattering rates on the Stokes and anti-Stokes sidebands due to the cavity resonance [62]. The full optomechanical Hamiltonian (see Eq. D.1), with the interaction term H_{om} (Eq. 8.4), predicts a cooling power [112]

$$P_{\text{c}} = \mathcal{N}\Gamma_{\text{sc}}\eta_0 E_{\text{r}}\zeta\left(\langle n\rangle\,|\mathcal{L}_+|^2 - (\langle n\rangle + 1)\,|\mathcal{L}_-|^2\right), \tag{8.5}$$

for a mean occupation number $\langle n\rangle$ of mode $\mathcal{X}$; here $\Gamma_{\text{sc}} = \langle a^\dagger a\rangle\Gamma g_0^2/\Delta^2$ is the photon scattering rate of a single atom at a probe antinode into free space, $\eta_0 = 4g_0^2/(\kappa\Gamma)$ is the cavity-to-free-space scattering ratio (single-atom cooperativity) introduced in Sec. 2.5, $E_{\text{r}} = \hbar^2 k^2/(2m)$ is the single-atom recoil energy, $\zeta = \mathcal{N}^{-1}\sum_i \sin^2(2k\xi_i)$, and $\mathcal{L}_\pm = [1 \mp 2i(\delta\pm\omega_t)/\kappa]^{-1}$ represents the cavity response at the frequency of the (anti-)Stokes sideband in terms of the probe-cavity detuning δ. In our experiments, where the atomic cloud is long ($\approx$ 1 mm) compared to the 5-μm beat length between trap and probe light, $\zeta = 1/2$. For $\omega_t \gtrsim \kappa/2$, the cooling rate is maximized by placing the anti-Stokes sideband on resonance ($\delta = -\omega_t$). Eq. 8.5 shows that the collective rate constant $\gamma_c = dP_{\text{c}}/d(\langle n\rangle\,\hbar\omega_t)$ is proportional to $\mathcal{N}$ due to cooperative scattering: the larger the ensemble, the faster $\mathcal{X}$ is cooled.

8.2 Cooling Rate

We study the cooling in the cavity described in Sec. 3.1, with linewidth $\kappa = 2\pi\times 1.01(3)$ MHz at the wavelength $2\pi/k = 780$ nm of the ^{87}Rb D$_2$ line and cooperativity $\eta_0 = 0.203(7)$. We trap 10^2-10^4 atoms of ^{87}Rb in the state $\left|5^2S_{1/2}, F = 2, m_F = 2\right\rangle$ in our standard 851-nm lattice in the cavity mode (Sec. 3.2), with trap frequency $\omega_t/(2\pi) = 480(40)$ kHz and typical trap depth $U_0/h = 18(3)$ MHz. The 780-nm probe laser drives the cavity on a TEM$_{00}$ mode with σ_+ polarization at a detuning $\Delta/(2\pi) \geq 70$ MHz from the $\left|5^2S_{1/2}, F = 2\right\rangle \rightarrow \left|5^2P_{3/2}, F' = 3\right\rangle$ transition with linewidth $\Gamma = 2\pi \times 6.1$ MHz. The probe laser is locked to a 36-GHz-detuned TEM$_{01}$ cavity mode that does not affect the atoms, in a scheme similar to that illustrated in Fig. 3.4(b).

As usual, we measure atom number via the cavity shift $\delta\omega_c = \mathcal{N}C\Omega_0$, where $C = \mathcal{N}^{-1}\sum_{i=1}^{\mathcal{N}}\sin^2(k\xi_i)$ if all atoms are situated on the cavity axis. Allowing for the small but non-zero radial cloud size $\sigma_r = 7(1)$ μm $\ll w$, $\mathcal{N}$ represents an equivalent number of on-axis atoms. Since the cloud is long ($\approx$ 1 mm) compared to the 5-μm beat length between trap and probe, $C = 1/2$ in the absence of probe light. Displacement of the atoms by the probe light reduces C by at most 12% in the experiments described below, and we account for this effect.

To perform cavity cooling/heating of the collective mode $\mathcal{X}$, we detune the laser by $\delta = \mp\kappa/2 \approx \mp\omega_t$ from cavity resonance, simultaneously probing the position $\hat{X}$ via the transmitted light. We first verify cavity heating by turning the probe light on at blue
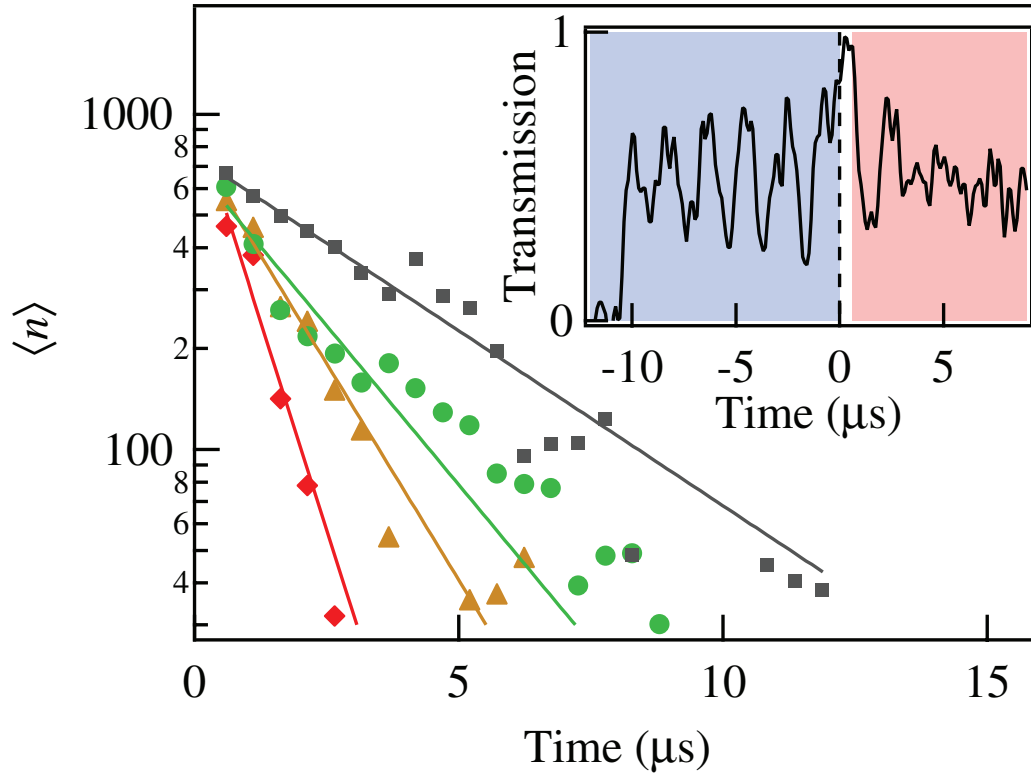
Figure 8-2: Mean occupation number $\langle n \rangle$ of mode $\mathcal{X}$ *vs.* time during cavity cooling at $\Gamma_{sc} = 1.1 \times 10^5$ s^{-1} (gray squares), 2.3×10^5 s^{-1} (green circles), 3.4×10^5 s^{-1} (gold triangles), and 6.4×10^5 s^{-1} (red diamonds). Each dataset is obtained by averaging variances from 10 traces. Inset: single trace of cavity transmission during cavity heating ($t < 0$, blue background) followed by cavity cooling ($t > 0$, red background).

detuning $\delta = +\kappa/2$. A collective oscillation triggered by the sudden turn-on of the light is indeed rapidly amplified by cavity heating (inset to Fig. 8-2). After typically 10 μs of heating, we switch to cavity cooling at $\delta = -\kappa/2$ and variable probe power. The mean occupation number $\langle n \rangle$ is obtained from the observed time trace via the fractional variance $\sigma^2 \equiv \overline{R^2}/\overline{R}^2 - 1$ of the transmitted photon rate R in a sliding 2-μs window. The linear approximation $X \propto R - \overline{R}$ gives the relation $\sigma^2 - \sigma_{\mathrm{bg}}^2 = 8(\mathcal{G}X_0/\kappa)^2 |\mathcal{L}_+ - \mathcal{L}_-|^2 \langle n \rangle$, where $X_0 = \sqrt{\hbar\zeta/(2Nm\omega_t)}$ and σ_{bg}^2 is a constant technical-noise offset (see App. D). Fig. 8-2 shows $\langle n \rangle$ $vs.$ time at four different probe intensities, with fixed atom number $\mathcal{N} = 2800(400)$ and detuning $\Delta/(2\pi) = 140$ MHz from atomic resonance. The cooling is well approximated by an exponential decay with rate constant γ_{exp} that depends on the probe power. We can also obtain γ_{exp} by fitting an exponentially decaying sinusoid to the average of the 10 transmission traces; the two methods agree.

To compare γ_{exp} to the predicted cooling rate constant γ_c, we measure the dependence of γ_{exp} on the photon scattering rate $\Gamma_{\mathrm{sc}} = \overline{R}\eta_0\Gamma^2/(2\Delta^2)$ per atom into free space for various probe-atom detunings Δ and atom numbers $\mathcal{N}$. As Fig. 8-3(a) shows, the data are consistent with a linear model $\gamma_{\mathrm{exp}} = f(\mathcal{N})\eta_0\Gamma_{\mathrm{sc}} + \gamma_{\mathrm{m}}$. The offset $\gamma_{\mathrm{m}} = 1.6(6) \times 10^5/\mathrm{s}$ indicates a quality factor $Q = \omega_t/\gamma_{\mathrm{m}} \approx 19$ for mode $\mathcal{X}$, largely attributable to mixing with other motional modes in the anharmonic trapping potential.

To verify the cooperative nature of the cavity cooling of mode $\mathcal{X}$, we plot in Fig. 8-3(b) the fitted slopes $f(\mathcal{N})$ as displayed in 8-3(a) $vs.$ atom number $\mathcal{N}$. Accounting for the slight reduction of the cooperativity $\eta = \eta_0/(1 + \alpha)$ due to atomic absorption, with $\alpha = \delta\omega_c \times \Gamma/(\kappa\Delta) < 0.2$, the measured dependence $d\gamma_{\mathrm{exp}}/d(\eta\Gamma_{\mathrm{sc}}) = 3.4(5) \times 10^{-3}\mathcal{N}$ agrees well with the prediction for cavity cooling $\gamma_c/(\eta\Gamma_{\mathrm{sc}}) = 3.0(2) \times 10^{-3}\mathcal{N}$. This confirms that the cooling speed for the collective mode $\mathcal{X}$ increases linearly with ensemble size and is proportional to the total power scattered by the ensemble into the cavity mode.

8.3 Equilibrium Temperature

To determine the equilibrium temperature of $\mathcal{X}$ under cooling, we require—given our detection noise—a longer observation time than shown in Fig. 8-2. We therefore observe the cooling or (for comparison) heating in spectra obtained from 150 time traces of the cavity transmission, each 440-μs long, with a mean photon transmission rate $\overline{R} = 1.2(2) \times 10^9 \ \mathrm{s}^{-1}$. Fig. 8-4 shows normalized one-sided spectral densities $S_I/\overline{I}^2$ of photocurrent $I \propto R$ with (a) $\mathcal{N} = 230(50)$ and (b) $\mathcal{N} = 450(90)$ atoms at a detuning $\Delta/(2\pi) = 70$ MHz from atomic resonance. Each spectrum displays a peak at ω_t with an area approximately proportional to both atom number $\mathcal{N}$ and mean occupation number $\langle n \rangle$. The disparity in area between cooling and heating increases with $\mathcal{N}$ due to the cooperative nature of the processes.

We fit the spectra in Fig. 8-4 with a quantum mechanical model (black curves) adapted from the treatment of Marquardt $et\ al.$ [112] as described in App. D. The model $S_I/\overline{I}^2 =$
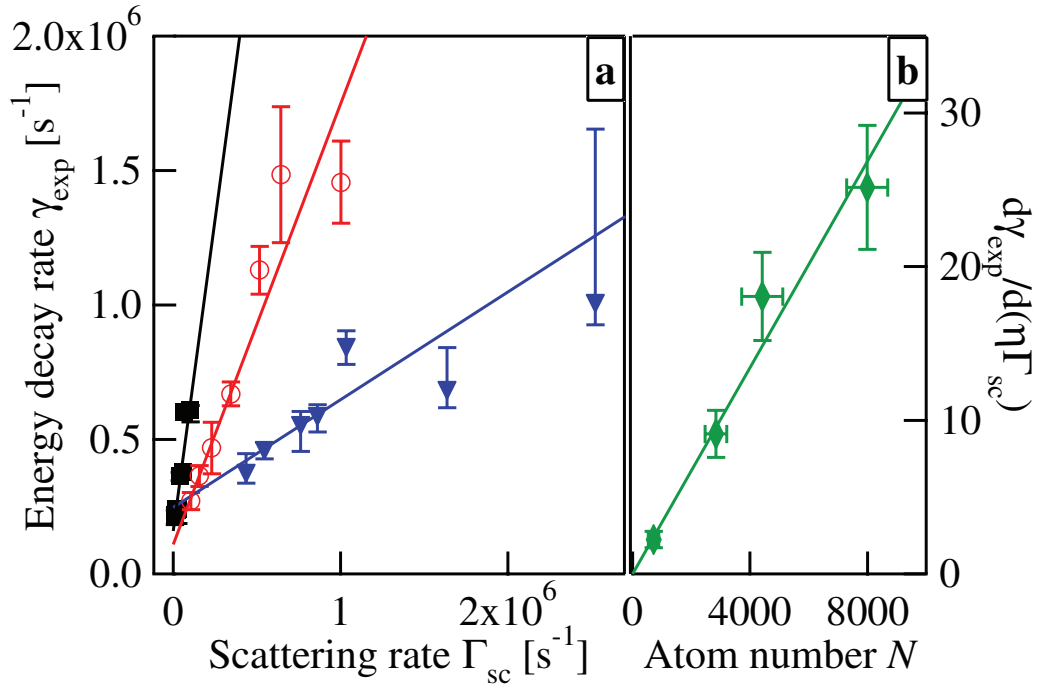
Figure 8-3: Collective cooling rates. (a) Energy decay rate γ_{exp} *vs.* scattering rate Γ_{sc} for: $\mathcal{N}$=8000(700), $\Delta/(2\pi) = 270$ MHz (solid black squares); $\mathcal{N}$=2800(400), $\Delta/(2\pi) = 140$ MHz (open red circles); $\mathcal{N}$=700(200), $\Delta/(2\pi) = 70$ MHz (solid blue triangles). Lines are fits to data. (b) $\mathcal{N}$-dependence of cooling rate normalized to single-atom scattering rate into cavity.
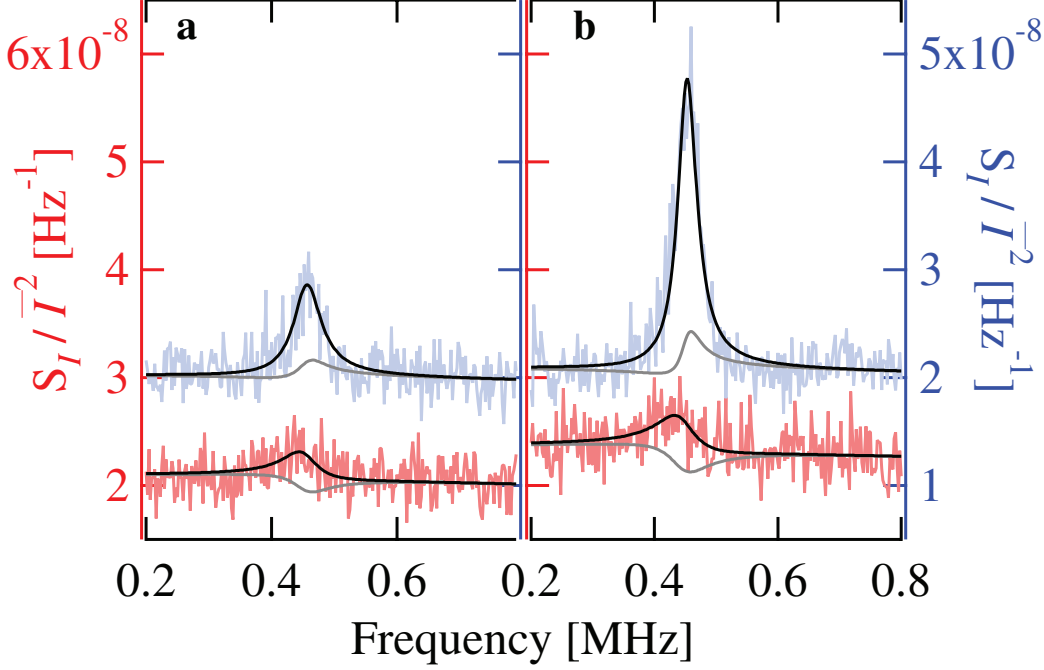
Figure 8-4: Spectra of fractional transmission fluctuations $S_I/\overline{I}^2$ taken with (a) $\mathcal{N} = 230(50)$ atoms and (b) $\mathcal{N} = 450(90)$ atoms at detuning $\delta = -\kappa/2$ (red lines) or $\delta = +\kappa/2$ (blue lines) from cavity resonance. Black curves are fits to data; subtraction of the background level S_{bg} (gray curves) yields the collective mode occupation $\langle n \rangle^\pm$ at $\delta = \pm\kappa/2$: (a) $\langle n \rangle^+ = 4.4 \pm 0.7$, $\langle n \rangle^- = 2.3^{+0.7}_{-0.3}$; (b) $\langle n \rangle^+ = 7 \pm 1$, $\langle n \rangle^- = 2.0^{+0.9}_{-0.3}$.

$S_{\text{mech}} + S_{\text{bg}}$ contains the signal of interest $S_{\text{mech}} \approx (2\mathcal{G}/\kappa)^2 \left| \mathcal{L}_+ - \mathcal{L}_- \right|^2 S_X$ arising from atomic motion with spectral density S_X; and a background S_{bg} (gray curves) that is dominated by electronic noise of the photodetector but also accounts for photon shot noise, slightly smaller fluctuations from laser phase noise, and frequency-dependent correlations between the light noise and the atomic motion. These last are responsible for the dips in S_{bg} below the white noise [119]. With the photon rate $\overline{R}$ and optomechanical coupling $\mathcal{G}$ constrained to their independently measured and calculated values, the cooling spectra are well fit by taking the collective mode to be coupled to a white Markovian bath with $\langle n_{\text{bath}} \rangle = 3.1(4)$ motional quanta per mode; the corresponding coupling rate $\gamma'_{\text{m}} = 2.6(1.1) \times 10^5 \text{ s}^{-1}$ is consistent with the mixing rate γ_{m} from Fig. 8-3. Fits to the heating spectra, which are complicated by sympathetic heating of other modes, indicate a higher mixing rate of $4.8(5) \times 10^5$ /s.

The bath occupation is consistent with a measured upper bound on the axial temperature of $150(50)$ μK, corresponding to $\langle n_{\text{bath}} \rangle = 6(2)$ (see App. D). The white spectrum of n_{bath} is a simplistic ansatz, but the resulting fit helps to establish the background S_{bg} and thus the motional spectrum S_X. By subtracting S_{bg} from the measured spectrum, we obtain a minimum mean occupation number of $\mathcal{X}$ of $\langle n \rangle_{\text{min}} = 2.0^{+0.9}_{-0.3}$ with $\mathcal{N} = 450(90)$ atoms. Note that failing to account for the dip in S_{bg} would lead to an underestimate of

$\langle n \rangle_{\mathrm{min}}$.

Let us now consider limits to cooling the collective mode. For $\gamma_c \gg \gamma_{\mathrm{m}}$, the cooling power $P_{\mathrm{c}} \propto \mathcal{N}\eta_0$ competes only with the $\mathcal{N}$-independent recoil heating $P_{\mathrm{rec}} \approx E_{\mathrm{r}}\Gamma_{\mathrm{sc}}$ of the single mode $\mathcal{X}$, yielding a fundamental limit $\langle n \rangle \geq n_0 + D(1+n_0)/(\mathcal{N}\eta_0)$, where $n_0 \equiv (\kappa/4\omega_t)^2$ and D is a prefactor of order unity [62]. Thus, for large collective cooperativity $\mathcal{N}\eta_0 \gg 1$ (easy to achieve), the resolved-sideband regime $n_0 < 1$ in principle allows ground-state cooling [62, 112, 113] of the collective mode. Cooling of $\mathcal{X}$ will then be limited by the thermal heat load from other modes mixing at rate γ_{m} with $\mathcal{X}$, yielding a limit $\langle n \rangle \gtrsim \langle n_{\mathrm{bath}} \rangle \gamma_{\mathrm{m}}/(\gamma_{\mathrm{m}}+\gamma_c)$. While this limit improves with increasing cooling rate γ_c, for the values $(\omega_t, \kappa, Q = \omega_t/\gamma'_{\mathrm{m}})$ in Fig. 8-4 amplification of low-frequency noise on approaching the regime of static bistability $\gamma_c \gtrsim \omega_t^2/\kappa$ [112] sets a bound $\langle n \rangle \geq 1.5$, even though $n_0 = 0.3$.

A low occupation $\langle n \rangle$ of the collective mode $\mathcal{X}$ is disadvantageous for cooling the individual atoms, since the absolute cooling power is proportional to $\langle n \rangle$ (see Eq. 8.5). Cooling of all degrees of freedom is thus facilitated by strong mixing $\gamma_{\mathrm{m}} \gg \gamma_c$ that keeps mode $\mathcal{X}$ in thermal equilibrium with the other $3\mathcal{N} - 1$ modes. The cooling power per atom $P_{\mathrm{c}}/\mathcal{N}$ then approaches that of an isolated atom. Thus, in contrast to a hypothesis put forward in Ref. [108], single-particle cooling cannot be improved by cooperative scattering. In particular, even in an ensemble, recoil heating sets a limit for the temperature of individual atoms $\langle n_i \rangle \gtrsim n_0 + 1/\eta_0$ that depends on the *single-atom* cooperativity η_0: ground-state cooling requires $\eta_0 > 1$ [62].

8.4 Outlook

In our system, sympathetic cooling of all modes is hampered by the weak single-atom cooperativity $\eta_0 < 1$ and by weak mixing of $\mathcal{X}$ with modes that correspond to the motion of atoms at trap locations ξ_i with $\sin(2k\xi_i) \approx 0$ (see Eq. 8.2). Even so, we are able to counteract the total axial recoil heating of the ensemble by $40(10)\%$ by applying cavity cooling to mode $\mathcal{X}$ (see App. D.2). Future experiments with $\eta_0 \gtrsim 1$ and better trapping geometry should achieve sympathetic cooling of all motional degrees of freedom. In particular, cooling of the single-atom modes might ultimately be optimized in the low-Q Doppler regime.

Conversely, deeper in the resolved-sideband regime, ground-state cooling of the collective mode could enable the preparation of non-classical collective states [114] at finite thermodynamic temperature. By analogy with the conditional spin squeezing presented in Ch. 5, squeezed mechanical states could be prepared by replacing the QND measurement of spin with a stroboscopic measurement of the displacement of the collective mode [120, 121]. Alternatively, it may even be possible to perform quantum state transfer of the spin squeezing to the mechanical degree of freedom [122].

Appendices

Appendix A

Laser-Cavity Frequency Stabilization

A key enabling technology for all of the experiments in this thesis is the locking of lasers to the optical resonator. Two principal factors can limit the performance of such locks: the gain achievable given the bandwidth of the feedback, and the signal-to-noise ratio given the allowable intracavity laser power. Section A.1 describes our general approach to laser locking with ~ 2 MHz bandwidth, which we apply to both the probe and trap lasers. For the case of the probe laser, the lock performance in the frequency range of interest is then limited only by the signal-to-noise ratio achievable given the permissible intracavity lock light power; Sec. A.2 discusses the optimization of the probe laser lock given this constraint. For the trap laser, where the lock bandwidth limits the gain achievable at the frequency ~ 500 kHz relevant to parametric heating, we benefit from narrowing the passive linewidth of the laser by optical feedback; this is described in Sec. A.3.

A.1   High-Bandwidth Locking

The most obvious reason for desiring a large lock bandwidth B is to suppress noise at high frequencies (up to B). For example, for our standing-wave dipole trap with axial trap frequency $f_{\mathrm{ax}} \approx 500$ kHz, a lock bandwidth $B > f_{\mathrm{ax}}$ is needed to suppress noise that would otherwise lead to parametric heating of the atoms (see Ch. 3). Equally important, though, the larger the bandwidth the greater a gain is achievable at low frequencies. Our spin squeezing experiments are sensitive primarily to noise at frequencies below 10 kHz, but a much larger lock bandwidth $B \sim 2$ MHz allows us to suppress this noise by orders of magnitude, narrowing the laser from a passive linewidth ~ 100 kHz to an effective linewidth < 1 kHz in the frequency range of interest. This section describes our method of high-bandwidth locking.

A.1.1 Experimental Setup

The techniques I describe below were applied to two different lasers. The 780-nm probe laser is a grating-stabilized diode laser with, in the absence of the lock, a linewidth of about 100 kHz. The 851-nm trap uses a distributed feedback (DFB) laser diode (Eagleyard Photonics) and is discussed in more detail in Sec. A.3. The cavity linewidth is $\kappa_{780} = 2\pi \times 1.01(3)$ MHz at 780 nm and $\kappa_{851} = 2\pi \times 135(2)$ kHz at 851 nm.

A.1.2 Pound-Drever-Hall Technique

We lock our lasers to the cavity using the Pound-Drever-Hall technique [123]. An excellent didactic review of this method has been written by Black [124]. The basic idea is to phase modulate the laser at a frequency $\Omega_{\mathrm{PDH}} \gg \kappa$ and detect the light reflected from the cavity on a photodiode, looking for a signal at the modulation frequency Ω_{PDH}. The directly reflected light produces no such signal (having only phase- and not amplitude modulation). However, if the carrier (or a sideband) is on or near resonance, the light that enters and leaks back out of the cavity will have acquired a phase shift. The interference of this light with the sidebands (or the carrier) produces a beat note on the photodiode at Ω_{PDH}, and by demodulating the beat note one measures the phase of the light leaking out of the cavity, which depends upon its detuning from cavity resonance. For an appropriate choice of demodulation phase, one obtains the dispersive error signal shown in the inset to Fig. A-1 (green).

The Pound-Drever-Hall technique has several attractive features. For one, it is insensitive to fluctuations or drifts in laser power. It is also immune to low-frequency electronic noise, being sensitive only to a band of frequencies centered around Ω_{PDH}. In most cases, Ω_{PDH} can be chosen fairly arbitrarily but should be large compared to the desired lock bandwidth, as well as the cavity linewidth, without exceeding the bandwidth of the photodiode.

A.1.3 Dual-Path Feedback

Typical laser locks in our lab have a bandwidth $\lesssim 100$ kHz, limited by the finite gain-bandwidth products and parasitic capacitances of a series of op-amps in the feedback circuitry. To achieve a larger bandwidth, we follow the approach of Cacciapuoti *et al.* [125], applying direct feedback to the laser diode using only passive components to tune the gain and phase. To protect the laser diode, the direct feedback is AC-coupled, so that it must be combined with an ordinary slow feedback path that locks the laser at DC via the modulation input of a current controller. The complete dual-path feedback loop is shown schematically in Fig. A-1. (Note that the current controller also applies feed-forward to a piezo to adjust the length of the laser's external cavity, so in total the error signal is fed into three paths. However, the piezo response is rolled off at a frequency < 100 Hz, and I will ignore it from
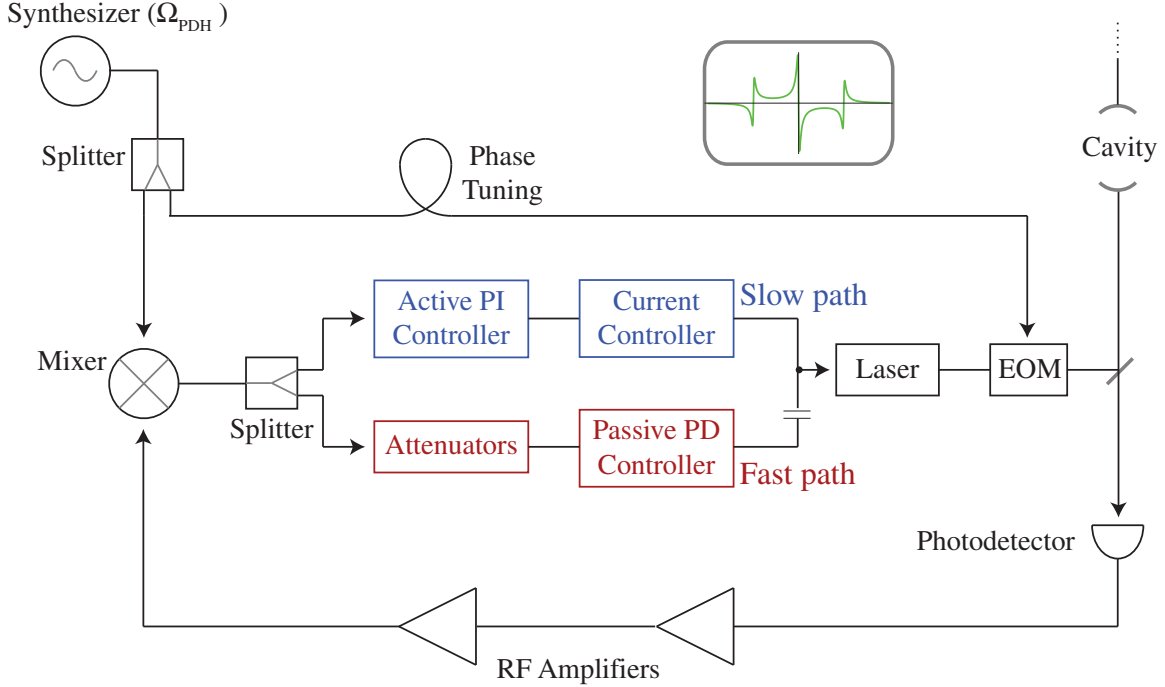
Figure A-1: Dual-path Pound-Drever-Hall lock.

here on.)

The design of the slow path is relatively uncritical; we use a standard PI controller, whose idealized transfer function is illustrated schematically by the thin-line Bode plot in Fig. A-2. For the fast path, there are several design constraints to ensure stability at its crossing with the slow path and to compensate for phase lags in the response of the laser diode and cavity. Fig. A-2 shows a schematic of the passive circuit that controls the response of the fast path; and a Bode plot (bold lines) of its transfer function.

At the crossover frequency where the fast and slow paths have equal gain, instability would arise if they had opposite phase. At DC, the slow path must be an integrator and the fast path a differentiator (due to the protective AC coupling), i.e. the two paths are in precisely the 180° phase relationship that must be avoided at the crossover. To allow for a stable crossover, the gain of the fast path is rolled back to proportional at a corner frequency of ≈ 800 Hz.

The fast path also needs to compensate for phase lags in the response of the laser and the cavity. Modulation of the laser current affects the wavelength by two different mechanisms: for slow modulation, the dominant effect is thermal, whereas at modulation frequencies $\gtrsim 1$ MHz the thermal effect becomes negligible and one is left with a weaker wavelength tuning via the current-dependent carrier density in the semiconductor [126]. Compounding the frequency-dependent response of the laser diode is the frequency-dependent response of the cavity, which constitutes a low-pass filter that rolls off at a frequency $\kappa/(2\pi)$ set by the cavity linewidth. We partially compensate for the roll-off of laser and cavity response
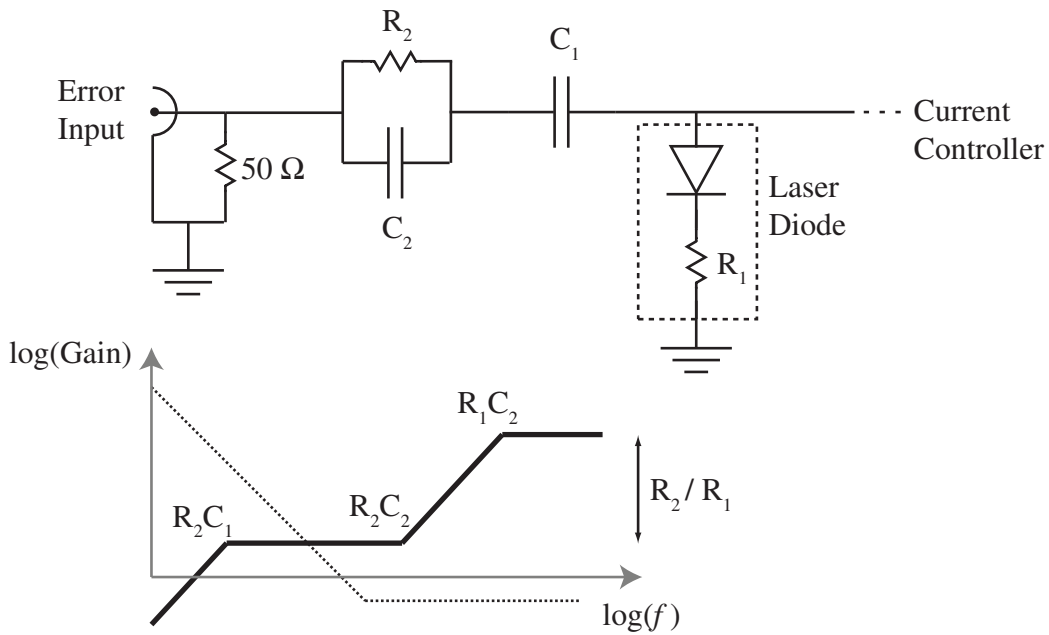
Figure A-2: Schematic of the fast feedback path. R_1 represents the internal resistance of the laser diode. Capacitance $C_1 = 1\ \mu$F provides protective ac-coupling, while values $R_2 = 200\ \Omega$ and $C_2 = 330$ pF are chosen to tune the response of the fast path, as described in the text. Also shown is a Bode gain plot of both the fast (bold) and slow (dotted) paths. Not shown are the response of the laser diode and cavity, which roll off the gain at high frequency.

by differential gain in the fast-path controller starting at an empirically optimized corner frequency of 2 MHz, set by $1/(2\pi R_2 C_2)$ in Fig. A-2.

The optimized transfer function measured for the 780 nm probe laser, including both the slow and fast paths, is shown in Fig. A-3. While Fig. A-3 shows a unity-gain bandwidth $B = 1$ MHz, we have found that the low-frequency noise is optimized by a somewhat higher overall gain—corresponding to $B \leq 3$ MHz—at the expense of servo bumps at B which are suppressed by being in the wings of the Lorentzian cavity line and are anyway far beyond the bandwidth of our measurement.

It is important to note that at bandwidths above 1 MHz, lock performance can easily be limited simply by the time it takes for the signal to travel from the laser to the cavity and back. A signal traveling through optical fibers and BNC cables at a typical speed $\sim (2/3)c$ accrues a phase lag of $\sim 2°/$MHz/m. With several meters of path length, this effect becomes noticeable around 1 MHz and will generally prohibit a bandwidth $\gtrsim 10$ MHz. Not only should path length be minimized, but components such as electronic filters introducing a group delay (often used in Pound-Drever Hall locking to suppress an unwanted signal at $2\Omega_{\mathrm{PDH}}$) should be avoided in the fast path.

A.2   Probe Frequency Noise

The spectrum of frequency fluctuations of the probe laser, either free-running (green squares) or locked to the cavity (blue circles) is shown in Fig. A-4. The noise is measured by sending a portion of the probe light to a monitor cavity with a 4 MHz linewidth, tuning the probe laser (either directly, or by tuning the cavity to which it is locked) to the slope of the monitor cavity's transmission profile, and detecting the transmission fluctuations on a fast photodiode connected to a spectrum analyzer. As expected from the transfer function in Fig. A-3, the frequency fluctuations are appreciably suppressed out to a bandwidth of 1 MHz.

The degree of noise suppression we attain is limited not only by the gain of the lock but, more importantly, by the amount of locking light to which we are willing to expose the atoms. For a fixed tolerable intracavity power, the optimal signal-to-noise ratio is attained by locking the cavity to one of the Pound-Drever-Hall sidebands and, in the limit of a strong carrier, depends only on the power P_{lock} in this sideband. Figure A-4(b) shows the dependence on lock sideband power of the probe laser's frequency noise, as quantified by the fractional variance in transmission of the probe sideband at its usual half-linewidth detuning from cavity resonance (blue circles); the scheme of locking and probing is similar to that illustrated in Fig. 3.4(b). The variance follows a photon-shot-noise scaling with the inverse of the lock power (dotted line). We typically operate with a lock power of 40 nW, corresponding to a fractional transmission variance of $6 \times 10^{-10}/$Hz in the band of frequencies $\sim 1 - 10$ kHz to which our squeezing measurements are most sensitive.
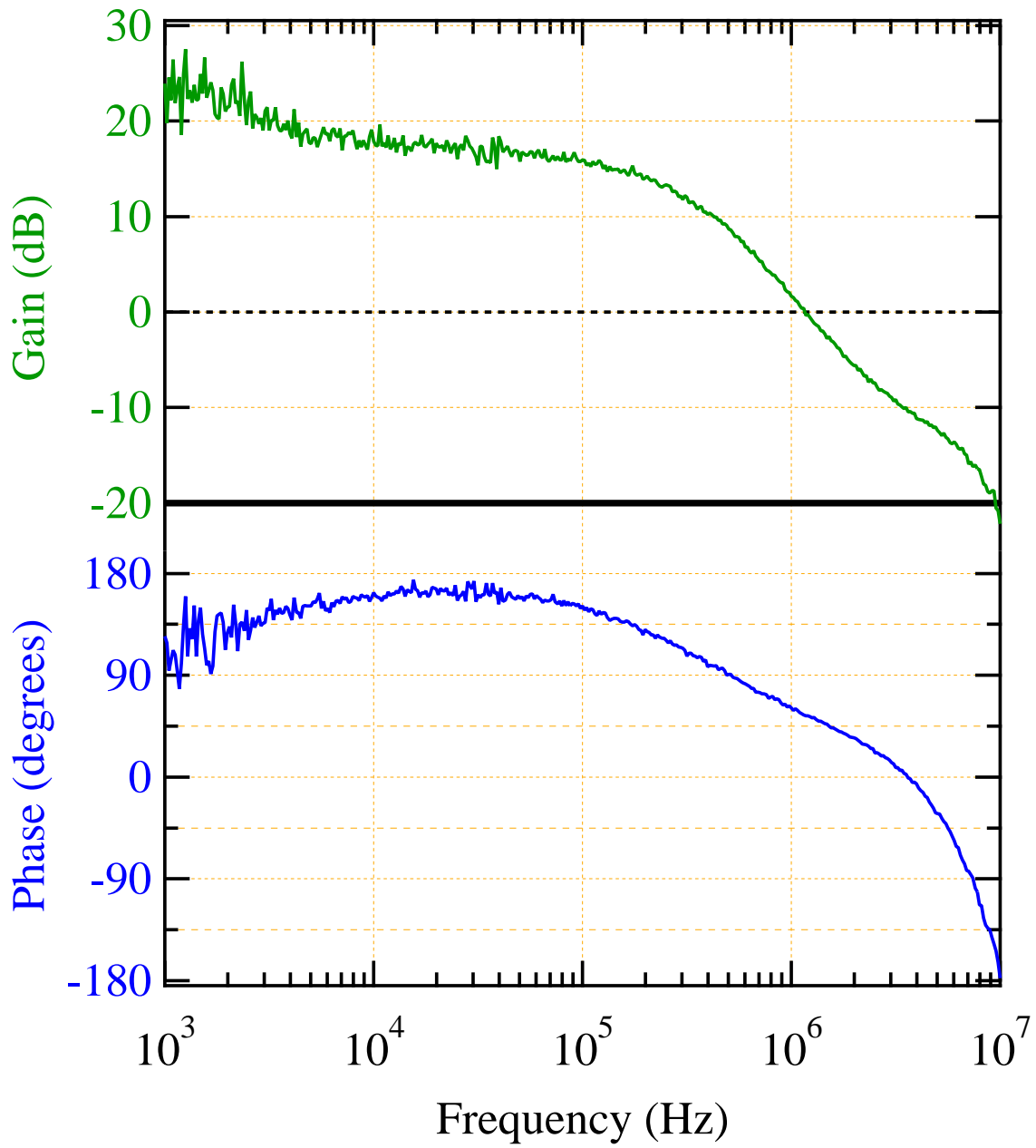
Figure A-3: Transfer function of 780 nm probe laser's lock to cavity.
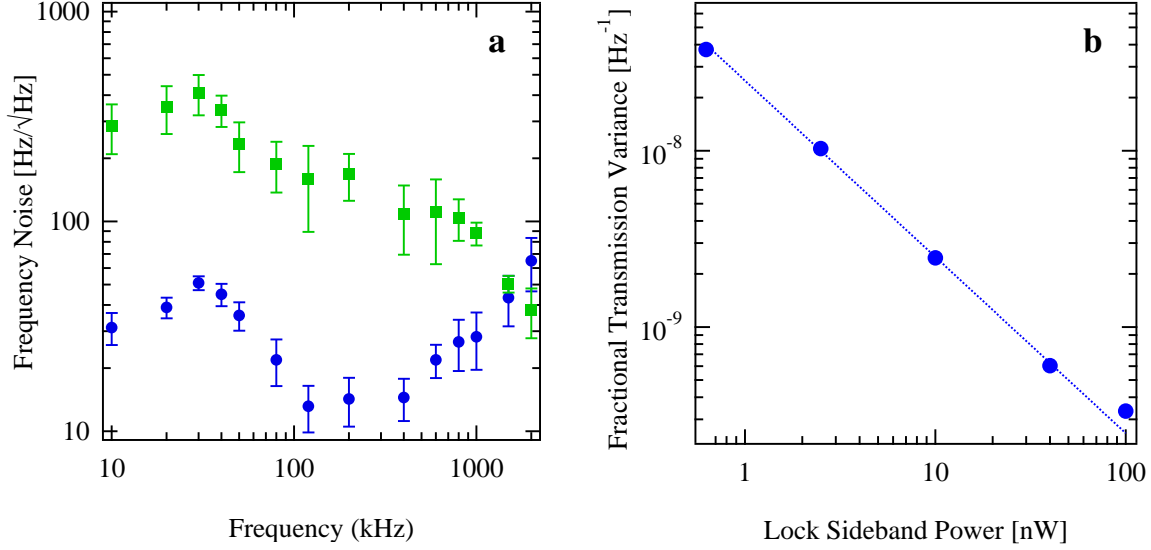
Figure A-4: (a) Spectrum of the probe laser's frequency fluctuations, measured either with the laser in lock (blue circles) or free-running (green squares). (b) Dependence of probe laser noise on lock sideband power; shown are the fractional fluctuations in probe sideband transmission at a frequency of 5 kHz, with the probed detuned by $\kappa/2$ from cavity resonance.

A.3 Passive Optical Feedback

For the trap laser, we supplement the active Pound-Drever-Hall frequency stabilization with passive optical feedback. The optical feedback is provided by a partial reflector mounted ~ 20 cm from the laser diode, as shown in Fig. A-5. The pickoff is wedged to prevent interference, and we use only the $< 1\%$ reflection from the anti-reflection-coated face, as we find that stronger feedback prevents single-mode operation.

Figure A-6 shows the fractional variance of the trap laser transmission—or, equivalently, of the trap depth—before and after applying the optical feedback. The factor of ~ 20
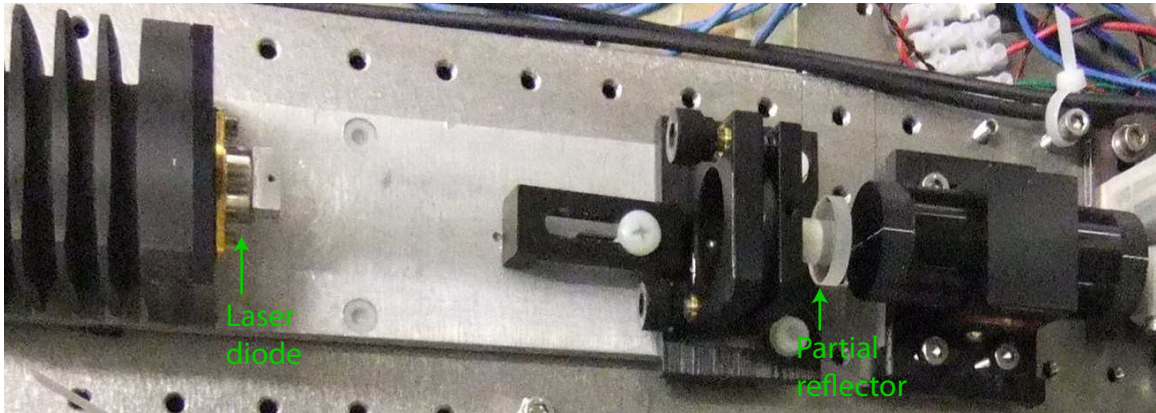
Figure A-5: Simple setup for narrowing a DFB laser by optical feedback, as described in the text.
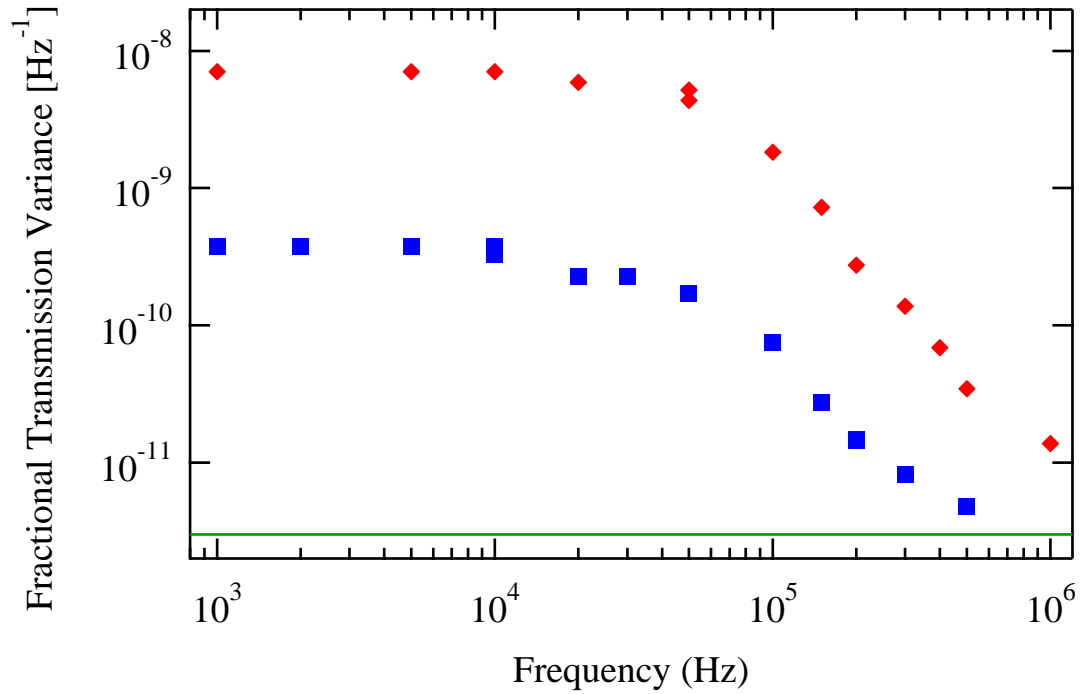
Figure A-6: Fractional intensity fluctuations of the cavity-enhanced 851-nm lattice before (red) and after (blue) optical narrowing. Green line indicates the noise floor of the measurement.

reduction in intensity variance theoretically provides the same reduction factor in the energy e-folding time associated with parametric heating in the trap [70]. We indeed observe a lengthening in the lifetime of atoms in the trap, from 70(10) ms to 540(50) ms at a trap depth of 90 MHz. The lifetime has since been further improved by reducing both the trap frequency and the initial atomic temperature.

Appendix B

Optical Pumping

We optically pump the atoms into $|F, m_F\rangle = |1, 0\rangle$ using σ_+/σ_--polarized light on the $F = 1 \to F' = 0$ transition while repumping on $F = 2 \to F' = 2$. This pumping procedure achieves only about 88% purity, with 12% of the atoms remaining in $|1, \pm 1\rangle$. We are able to ignore these spectator atoms entirely because their effect is canceled by our spin-echo probing scheme (Sec. 4.4).

Nevertheless, one can take additional steps to improve the state purity. Subsequent to the initial pumping into $|1, 0\rangle$, one can apply a $\tilde{\pi}$ pulse on the $|1, 0\rangle \to |2, 0\rangle$ transition, empty all $F = 1$ states using resonant light on the $F = 1 \to F' = 1$ transition, use a second $\tilde{\pi}$ pulse to return atoms from $|2, 0\rangle$ to $|1, 0\rangle$, and expel all atoms remaining in $F = 2$ from the trap using resonant light on the $F = 2 \to F' = 3$ transition. After this procedure, more than 99% of the remaining atoms are in the state $|1, 0\rangle$. We used this procedure in early experiments, including the squeezed-state preparation by QND measurement. Since the procedure results in loss of atoms, however, we forgo it when performing multiple trials with the same loaded atoms.

Appendix C

Scattering

C.1   Effect on Attainable Squeezing

At finite optical depth, the performance of light induced squeezing is necessarily limited by photon scattering out of the probe mode [55, 56]. Scattering can counteract the squeezing both by reducing the atomic coherence and by adding noise. The more fundamental effect is the decoherence, to which all scattering events—both Rayleigh (elastic) and Raman (inelastic)—contribute [61]. However, unless one probes only on cycling transitions [64], the dominant limitation is noise added by Raman scattering.

Raman scattering, by flipping the atomic pseudo-spins over the course of the squeezing process, reduces the correlation between the atomic-state information that was transferred to the light and the actual atomic state at the end of the squeezing. To analyze its effect, let us evaluate the correlation $\mathrm{Cov}(S_z(t), S_z(t'))$ between S_z at two arbitrary times $t' \geq t$ in terms of the Raman scattering rate Γ_{flip}. I will assume that $\langle S_z \rangle = 0$ in the initial state and remains so due to symmetric Raman scattering rates between the two spin states; then $\mathrm{Cov}(S_z(t), S_z(t')) = \langle S_z(t)S_z(t') \rangle$. In the limit of a short time-step τ, we can assume that any spin is flipped at most once; so that the number of spins N_-, N_+ that are flipped from up to down or vice versa during the time τ can be written in terms of the total numbers $N_\uparrow, N_\downarrow$ of atoms in states $|\uparrow\rangle, |\downarrow\rangle$ as

$$N_- = \Gamma_{\mathrm{flip}}\tau N_\uparrow + \delta_\uparrow, \quad N_+ = \Gamma_{\mathrm{flip}}\tau N_\downarrow + \delta_\downarrow, \tag{C.1}$$

where $\delta_{\uparrow/\downarrow}$ are uncorrelated random variables with $\langle \delta_{\uparrow/\downarrow} \rangle = 0$ and $\langle \delta_{\uparrow/\downarrow}^2 \rangle = \Gamma_{\mathrm{flip}}\tau N_{\uparrow/\downarrow}$, since the scattering is a Poisson process. With these relations, and the usual definitions $S_z = (N_\uparrow - N_\downarrow)/2$ and $S = (N_\uparrow + N_\downarrow)/2$, we evaluate $\langle S_z(t)S_z(t' + \tau) \rangle$ and $\langle S_z(t + \tau)S_z(t + \tau) \rangle$ to find that

$$\frac{d \langle S_z(t)S_z(t') \rangle}{dt'} = -2\Gamma \langle S_z(t)S_z(t') \rangle \tag{C.2}$$

and

$$\frac{d\left\langle S_z^2(t)\right\rangle}{dt} = -4\Gamma\left(\left\langle S_z^2(t)\right\rangle - \frac{S}{2}\right) \tag{C.3}$$

Thus, the Raman scattering results in a decaying correlation

$$\left\langle S_z(t)S_z(t')\right\rangle = \left\langle S_z^2(t)\right\rangle e^{-2\Gamma_{\text{flip}}|t'-t|}, \tag{C.4}$$

where for a CSS the variance $\left\langle S_z^2(t)\right\rangle$ is constant at $\left\langle S_z^2\right\rangle = S/2$. (For an arbitrary initial state $\left\langle S_z^2(t)\right\rangle$ exponentially approaches the CSS variance, with a rate constant $4\Gamma_{\text{flip}}$.)

The noise added by the scattering relative to the ideal QND squeezing is given by the fluctuations $\text{Var}(S_{zf} - \overline{S_z}) = \left\langle S_{zf}^2\right\rangle - 2\left\langle S_{zf}\overline{S_z}\right\rangle + \left\langle \overline{S_z}^2\right\rangle$ in the difference between the value S_{zf} of S_z at the end of a squeezing time $\mathcal{T}$ and the average value $\overline{S_z} = \int_0^{\mathcal{T}} S_z(t)dt$ during that time. Applying Eq. C.4 and assuming an initial CSS, to lowest order in $r \equiv \Gamma_{\text{flip}}\mathcal{T}$ we obtain

$$\frac{2}{S}\left\langle S_{zf}\overline{S_z}\right\rangle \approx 1 - r, \tag{C.5a}$$

$$\frac{2}{S}\left\langle \overline{S_z}^2\right\rangle \approx 1 - \frac{2r}{3}, \tag{C.5b}$$

and thus Raman scattering increases the normalized spin noise by

$$\frac{2}{S}\text{Var}(S_{zf} - \overline{S_z}) \approx \frac{4r}{3}. \tag{C.6}$$

C.2   Considerations in Quantifying Squeezing

Besides limiting the attainable squeezing, scattering can potentially lead to systematic errors in quantifying spin noise and squeezing. A measurement M with $\langle M\rangle_{\overline{S_z}} = \overline{S_z}$ is related to the final spin projection S_{zf}, according to Eq. C.5a, by $\langle M\rangle_{S_{zf}} \approx (1-r)S_{zf}$ for $r \ll 1$. This is because a spin that is flipped partway through the measurement contributes less to the measurement outcome, which is averaged over some time $\mathcal{T}$, than it does to S_z at any fixed time. Thus, to avoid underestimating spin noise, the measurement outcome should be rescaled by a factor of $1 + r$—or, equivalently, measured variances should be rescaled by $1 + 2r$ (still assuming $r \ll 1$). I take this small correction into account[1] in reporting the normalized spin noise $\sigma^2 = -8.8(8)$ dB in Sec. 5.3. Since the same factor affects measurements of noise and of signal (i.e., interference contrast $\mathcal{C}$) alike, it has no effect in quantifying the squeezing parameter $\zeta = \sigma^2/\mathcal{C}^2$.

---

[1]In the context of our experiments, I generalize the spin-flip probability r to a value [79] that accounts for various Raman scattering processes in our multi-level system—some of which remove atoms from the clock states entirely—as well as for microwave infidelity during the spin echo, as described in Sec. 4.5.

Appendix D

Quantifying Axial Motion

This appendix supplements the analysis of cooperative cavity cooling in Ch. 8. In Secs. D.1.1-D.1.4, I calculate the spectrum of intensity fluctuations at the output of the cavity, and I relate this spectrum to the motional spectrum of the collective mode $\mathcal{X}$. I closely follow the approach of Marquardt *et al.* [112] for calculating the displacement spectrum of a mechanical oscillator coupled to a cavity, and I additionally include lowest-order effects of laser phase noise [127]. After accounting in Sec. D.1.5 for technical effects in our photodetection of the cavity transmission, I derive in Sec. D.1.6 the relation of measured photocurrent fluctuations to the occupation $\langle n \rangle$ of the collective mode. Finally, in Sec. D.2 I describe measurements of the thermodynamic temperature associated with all $\mathcal{N}$ modes of the ensemble's axial motion.

D.1   Collective Motion and Transmission Fluctuations

In the optomechanical Hamiltonian derived in Ch. 8 (Eq. 8.3), the collective mode was entirely decoupled from all other ensemble modes due to our approximation of perfectly harmonic and homogeneous trapping. We allow for corrections to this simplified model by introducing a term H_{γ_m} representing coupling of the collective mode to a bath, which, in addition to including effects of mixing with other axial modes, might include effects of radial motion or light-induced effects beyond the optomechanical interaction included in H_{sys}. Further accounting for a coupling H_κ of the intracavity field to input field modes with energy H_{drive}, the full optomechanical Hamiltonian takes the form

$$H_{\text{tot}} = \hbar \left[\omega_c + \delta\omega_c + \mathcal{G}X_0(\hat{a}^\dagger + \hat{a}) \right] \left(\hat{c}^\dagger \hat{c} - \left\langle \hat{c}^\dagger \hat{c} \right\rangle \right) + \hbar \omega_t \hat{a}^\dagger \hat{a} + H_{\text{drive}} + H_\kappa + H_{\gamma_m}, \quad \text{(D.1)}$$

where we have subtracted an offset associated with the average intracavity light level and absorbed the associated force on the atoms into a redefinition of the trap centers ξ_i. In terms of the zero-point length $X_0 \equiv \sqrt{\hbar/(2M\omega_t)}$, the annihilation operator $\hat{a}$ for mode $\mathcal{X}$ has the usual definition such that $\hat{X} = X_0(\hat{a}^\dagger + \hat{a})$ and $\hat{P} = iM\omega_t X_0(\hat{a}^\dagger - \hat{a})$.

D.1.1 Equations of Motion

Equation D.1 is the standard optomechanical Hamiltonian [112, 113] describing a cavity mode, with operator $\hat{c}$, whose frequency is shifted in proportion to the position $X_0(\hat{a}^\dagger + \hat{a})$ of a mechanical oscillator of frequency ω_t. The last three terms in Eq. D.1 can be written out explicitly using the standard input-output formalism of quantum optics [82, 128]. One thereby derives equations of motion for $\hat{c}$ and $\hat{a}$ in terms of the optical input operators $\hat{c}_{\mathrm{in}j}$, corresponding to the fields driving the cavity from its two ends labeled by $j \in 1, 2$, and a mechanical input operator $\hat{a}_{\mathrm{in}}$ corresponding to the thermal bath. We shall describe the evolution of the field operators in a rotating frame at the drive frequency ω_L, writing the intracavity field operator $\hat{c} = (\bar{c} + \hat{d})e^{-i\omega_L t}$ in terms of a c-number $\bar{c}$ and a noise operator $\hat{d}$ that accounts for small deviations from the classical value, and similarly letting $\hat{c}_{\mathrm{in}j} = (\bar{c}_{\mathrm{in}j} + \hat{d}_{\mathrm{in}j})e^{-i\omega_L t}$. The classical field values are then in a steady-state relation

$$0 = (i\delta - \frac{\kappa}{2})\bar{c} - \sqrt{\frac{\kappa}{2}}\,(\bar{c}_{\mathrm{in}1} + \bar{c}_{\mathrm{in}2}), \tag{D.2}$$

while the deviations obey the linearized equations of motion [112]

$$\dot{\hat{d}} = (i\delta - \frac{\kappa}{2})\hat{d} + i\mathcal{C}\left(\hat{a} + \hat{a}^\dagger\right) - \sqrt{\frac{\kappa}{2}}\left(\hat{d}_{\mathrm{in}1} + \hat{d}_{\mathrm{in}2}\right), \tag{D.3}$$

$$\dot{\hat{a}} = (-i\omega_t - \frac{\gamma_m}{2})\hat{a} - \sqrt{\gamma_m}\hat{a}_{\mathrm{in}} + i\left(\mathcal{C}^*\hat{d} + \mathcal{C}\hat{d}^\dagger\right), \tag{D.4}$$

where $\delta \equiv \omega_L - (\omega_c + \delta\omega_c)$ represents the detuning of the drive field from cavity resonance for $X = 0$; and $\mathcal{C} \equiv -\mathcal{G}X_0\bar{c}$.

Defining the cavity response function $\chi_\kappa(\omega) = 1/[\kappa/2 - i(\omega + \delta)]$ and the mechanical response function $\chi_\mathrm{m}(\omega) = 1/[\gamma_m/2 - i(\omega - \omega_t)]$, and rewriting the equations of motion in the Fourier domain, we have:

$$\tilde{d}/\chi_\kappa(\omega) = i\mathcal{C}[\tilde{a}(\omega) + \tilde{a}^\dagger(-\omega)] - \sqrt{\frac{\kappa}{2}}[\tilde{d}_{\mathrm{in}1}(\omega) + \tilde{d}_{\mathrm{in}2}(\omega)], \tag{D.5}$$

$$\tilde{a}/\chi_\mathrm{m}(\omega) = i[\mathcal{C}^*\tilde{d}(\omega) + \mathcal{C}\tilde{d}^\dagger(-\omega)] - \sqrt{\gamma_m}\tilde{a}_{\mathrm{in}}(\omega). \tag{D.6}$$

Here, $\tilde{\mathcal{O}}(\omega) \equiv \int_{-T/2}^{T/2} e^{i\omega t}\hat{\mathcal{O}}(t)\,dt/\sqrt{T}$ denotes the windowed Fourier transform [128] of an operator $\hat{\mathcal{O}}$, and in calculating spectra $\left\langle \tilde{\mathcal{O}}(\omega)\tilde{\mathcal{O}}(-\omega) \right\rangle$ (for Hermitian $\hat{\mathcal{O}}$) we shall always implicitly take the limit $T \to \infty$ of a long window.

We can solve Eqs. D.5-D.6 to obtain the dependence of $\tilde{X}(\omega)/X_0 = \tilde{a}(\omega) + \tilde{a}^\dagger(-\omega)$ on the optical input fluctuations $\hat{d}_{\mathrm{in}} = (\hat{d}_{\mathrm{in}1} + \hat{d}_{\mathrm{in}2})/\sqrt{2}$ and the mechanical bath operator $\hat{a}_{\mathrm{in}}$:

$$\mathcal{D}(\omega)\left[\tilde{a}(\omega) + \tilde{a}^\dagger(-\omega)\right] = -\sqrt{\gamma_m}[\chi_\mathrm{m}^{-1*}(-\omega)\tilde{a}_{\mathrm{in}}(\omega) + \chi_\mathrm{m}^{-1}(\omega)\tilde{a}_{\mathrm{in}}^\dagger(-\omega)]$$
$$- 2\sqrt{\kappa}\omega_t\left[\mathcal{C}^*\chi_\kappa(\omega)\tilde{d}_{\mathrm{in}}(\omega) + \mathcal{C}\chi_\kappa^*(-\omega)\tilde{d}_{\mathrm{in}}^\dagger(-\omega)\right], \tag{D.7}$$

where

$$\mathcal{D}(\omega) = \chi_{\mathrm{m}}^{-1}(\omega)\chi_{\mathrm{m}}^{-1*}(-\omega) - 2i\,|\mathcal{C}|^2\,\omega_t\Pi(\omega) \tag{D.8}$$

and

$$\Pi(\omega) = \chi_\kappa(\omega) - \chi_\kappa^*(-\omega). \tag{D.9}$$

D.1.2 Input Field

We shall allow one end of the cavity to be driven by a laser at frequency ω_L that may have some phase noise. To account for this, we let $\hat{d}_{\mathrm{in}1} = \hat{d}_{\mathrm{in}0} + i\xi\overline{c}_{\mathrm{in}1}$, where $\hat{d}_{\mathrm{in}0}$ represents quantum fluctuations, while $\xi(t) \ll 1$ is a real-valued stochastic variable representing the phase noise. At the other end of the cavity, we will admit only vacuum fluctuations (setting $\overline{c}_{\mathrm{in}2} = 0$).

The quantum fluctuations ($j = 0, 2$) satisfy

$$\left\langle \tilde{d}_{\mathrm{in}j}^\dagger(\omega)\tilde{d}_{\mathrm{in}j}(\omega') \right\rangle = 0, \quad \left\langle \tilde{d}_{\mathrm{in}j}(\omega)\tilde{d}_{\mathrm{in}j}^\dagger(\omega') \right\rangle = \delta_T(\omega - \omega'), \tag{D.10}$$

where in the relevant limit $T \to \infty$, $\delta_T(0) = 1$ and $\delta_T(u) \to 0$ for $u \neq 0$. Phase noise modifies the corresponding relations for $\hat{d}_{\mathrm{in}1}$,

$$\left\langle \tilde{d}_{\mathrm{in}1}^\dagger(\omega)\tilde{d}_{\mathrm{in}1}(\omega') \right\rangle = \left\langle \tilde{\xi}(-\omega)\tilde{\xi}(\omega') \right\rangle |\overline{c}_{\mathrm{in}1}|^2,$$
$$\left\langle \tilde{d}_{\mathrm{in}1}(\omega)\tilde{d}_{\mathrm{in}1}^\dagger(\omega') \right\rangle = \delta_T(\omega - \omega') + \left\langle \tilde{\xi}(\omega)\tilde{\xi}(-\omega') \right\rangle |\overline{c}_{\mathrm{in}1}|^2, \tag{D.11}$$

and adds correlations

$$\left\langle \tilde{d}_{\mathrm{in}1}(\omega)\tilde{d}_{\mathrm{in}1}(-\omega') \right\rangle = -\left\langle \tilde{\xi}(\omega)\tilde{\xi}(-\omega') \right\rangle \overline{c}_{\mathrm{in}1}^2. \tag{D.12}$$

We will parameterize the laser noise by an effective linewidth $\gamma_L(\omega)$ given by the two-sided spectral density of frequency fluctuations, $\gamma_L(\omega) \equiv \omega^2 \left\langle \tilde{\xi}(\omega)\tilde{\xi}(-\omega) \right\rangle$. (For a laser with Lorentzian lineshape, γ_L is independent of frequency and represents the full width [129].)

D.1.3 Transmission Spectrum

We now proceed to calculate the two-sided spectrum $S_R^{(2)}(\omega)$ of cavity transmission fluctuations and relate this to the spectrum of the mechanical oscillator's motion. The rate R at which photons are transmitted from the cavity is given in terms of the output field operator $\hat{c}_{\mathrm{out}} = \hat{c}_{\mathrm{in}2} + \sqrt{\frac{\kappa}{2}}\hat{c}$ as $R = \hat{c}_{\mathrm{out}}^\dagger\hat{c}_{\mathrm{out}}$. The fluctuations of this rate about its mean value $\overline{R} = \overline{c}_{\mathrm{out}}^2$ are given by $\hat{c}_{\mathrm{out}}^\dagger\hat{c}_{\mathrm{out}} - \overline{c}_{\mathrm{out}}^2 \approx (\overline{c}_{\mathrm{out}}^*\hat{d}_{\mathrm{out}} + \overline{c}\hat{d}_{\mathrm{out}}^\dagger)$, where $\hat{d}_{\mathrm{out}} = \hat{c}_{\mathrm{out}} - \overline{c}_{\mathrm{out}}$ and we are working to lowest order in $\hat{d}_{\mathrm{out}}/\overline{c}_{\mathrm{out}}$. We assume, without loss of generality, that $\overline{c}$ is real. Defining $\epsilon(\omega) \equiv \tilde{d}_{\mathrm{out}}(\omega) + \tilde{d}_{\mathrm{out}}^\dagger(-\omega)$, we then have $S_R^{(2)}(\omega)/\overline{R} = \langle\epsilon(\omega)\epsilon(-\omega)\rangle$. Using

Eq. D.5 to evaluate $\tilde{d}_{\text{out}} = \tilde{d}_{\text{in2}} + \sqrt{\kappa/2}\tilde{d}$, we find $\epsilon(\omega) = \epsilon_{\text{opt}}(\omega) + \epsilon_{\text{mech}}(\omega)$, where

$$\epsilon_{\text{opt}}(\omega) = -(\kappa/2)\left[\chi_\kappa(\omega)\tilde{d}_{\text{in1}}(\omega) + \chi_\kappa^*(-\omega)\tilde{d}_{\text{in1}}^\dagger(-\omega)\right]$$
$$+ \left[1 - (\kappa/2)\chi_\kappa(\omega)\right]\tilde{d}_{\text{in2}}(\omega) + \left[1 - (\kappa/2)\chi_\kappa^*(-\omega)\right]\tilde{d}_{\text{in2}}^\dagger(-\omega) \tag{D.13}$$

and

$$\epsilon_{\text{mech}}(\omega) = i\mathcal{C}\sqrt{\kappa/2}\Pi(\omega)\left[\tilde{a}(\omega) + \tilde{a}^\dagger(-\omega)\right]. \tag{D.14}$$

Here, ϵ_{opt} contains the intensity fluctuations due to photon shot noise or technical noise of the drive light, whereas ϵ_{mech} describes fluctuations in transmission due to atom-induced shifts of the cavity resonance.

Using Eqs. D.13 and D.14, we can express the fractional fluctuations in transmitted intensity as the sum of three terms describing, respectively, the intrinsic optical fluctuations; the motion-induced fluctuations; and the correlations between the first two:

$$S_R^{(2)}(\omega)/\overline{R}^2 = S_{\text{opt}}^{(2)}(\omega) + S_{\text{mech}}^{(2)}(\omega) + S_{\text{fb}}^{(2)}(\omega). \tag{D.15}$$

Here,

$$S_{\text{opt}}^{(2)}(\omega) = \langle \epsilon_{\text{opt}}(\omega)\epsilon_{\text{opt}}(-\omega)\rangle/\overline{R} = 1/\overline{R} + \gamma_L(\omega)|\Pi(\omega)|^2 \tag{D.16}$$

represents the optical fluctuations that would be present even in the absence of optome-chanical coupling, namely photon shot noise and laser phase noise (converted into intensity noise by the cavity). $S_{\text{mech}}^{(2)}(\omega)$ is directly related to the spectrum $S_X^{(2)}(\omega) = \left\langle \tilde{X}(\omega)\tilde{X}(-\omega)\right\rangle$ of the mechanical motion (evaluated below in Eq. D.19) by

$$S_{\text{mech}}^{(2)}(\omega) = \langle \epsilon_{\text{mech}}(\omega)\epsilon_{\text{mech}}(-\omega)\rangle/\overline{R} = \mathcal{G}^2|\Pi(\omega)|^2 S_X^{(2)}(\omega). \tag{D.17}$$

Finally, the correlations between the mechanical motion and the optical noise are described by

$$S_{\text{fb}}^{(2)}(\omega) = \langle \epsilon_{\text{opt}}(\omega)\epsilon_{\text{mech}}(-\omega) + \epsilon_{\text{mech}}(\omega)\epsilon_{\text{opt}}(-\omega)\rangle/\overline{R}$$
$$= -4(\mathcal{G}X_0)^2\omega_t\text{Im}\left[\frac{\Pi(\omega)}{\mathcal{D}(\omega)}\left(\chi_\kappa^*(\omega) + 2\gamma_L(\omega)|\Pi(\omega)|^2\overline{R}/\kappa\right)\right]. \tag{D.18}$$

D.1.4 Displacement Spectrum

We evaluate the two-sided spectrum of the mechanical oscillator's displacement $S_X^{(2)}(\omega) = \left\langle \tilde{X}(\omega)\tilde{X}(-\omega)\right\rangle$ using Eq. D.7. Applying the simplest possible model for the bath, namely

quantum white noise [130] with $\left\langle \tilde{a}^\dagger_{\text{in}}(\omega)\tilde{a}_{\text{in}}(\omega)\right\rangle \equiv \langle n_{\text{bath}}\rangle$, we obtain

$$S_X^{(2)}(\omega)\frac{|\mathcal{D}(\omega)|^2}{X_0^2} = \gamma_m\left[(\langle n_{\text{bath}}\rangle + 1)\left|\chi_{\text{m}}^{-1}(-\omega)\right|^2 + \langle n_{\text{bath}}\rangle\left|\chi_{\text{m}}^{-1}(\omega)\right|^2\right]$$
$$+ 4\kappa\left|\omega_t\mathcal{C}\chi_\kappa(\omega)\right|^2 + 8[\gamma_L(\omega)\overline{R}/\kappa]\left|\omega_t\mathcal{C}\Pi(\omega)\right|^2. \tag{D.19}$$

The first pair of terms (in square brackets) describes motion arising from the oscillator's coupling to the bath. The middle term describes motion induced by photon shot noise of the probe light, while the last term describes motion induced by laser frequency noise.

Note that in the absence of optomechanical coupling ($\mathcal{C} = 0$), the oscillator spectrum $S_X^{(2)}(\omega)$ reduces to a pair of Lorentzians centered about $\pm\omega_t$

$$\left.\frac{S_X^{(2)}(\omega)}{X_0^2}\right|_{\mathcal{C}=0} = \gamma_m\left[(\langle n_{\text{bath}}\rangle + 1)|\chi_{\text{m}}(\omega)|^2 + \langle n_{\text{bath}}\rangle|\chi_{\text{m}}(-\omega)|^2\right], \tag{D.20}$$

whose area is set by the bath temperature

$$\int_{-\infty}^{\infty}\frac{d\omega}{2\pi}\frac{S_X^{(2)}(\omega)}{X_0^2} = 2\langle n_{\text{bath}}\rangle + 1. \tag{D.21}$$

D.1.5 Comparison with Measured Spectra

The spectra we measure are one-sided spectra, which we shall denote generically in terms of the two-sided spectra $S^{(2)}(\omega)$ by $S(\omega) \equiv S^{(2)}(\omega) + S^{(2)}(-\omega)$. The actual noise measured at the photodetector, normalized to the average photocurrent $\overline{I}$, is $S_I(\omega)/\overline{I}^2 = S_R(\omega)/\overline{R}^2 + \Sigma_{\text{det}}$. Here, Σ_{det} accounts for imperfect quantum efficiency $Q = 0.5(1)$, an excess noise factor $F = 4.5(5)$ of the avalanche photodiode, and dark (primarily Johnson) noise, and is given by

$$\Sigma_{\text{det}} = \frac{F - Q}{Q}\frac{2}{\overline{R}} + \frac{S_J}{(Q\overline{R})^2}, \tag{D.22}$$

where $S_J = 1.5(3) \times 10^9$ /(s^2 Hz) expresses the measured dark noise in units of equivalent photon rate. The spectra in Fig. 8-4 are taken with a photon rate $\overline{R} = 1.2 \times 10^9$/s at the output of the cavity, which yields $\Sigma_{\text{det}} = 1.6(1) \times 10^{-8}$/Hz.

We can now write the measured spectrum as $S_I(\omega)/\overline{I}^2 = S_{\text{mech}}(\omega) + S_{\text{bg}}(\omega)$, where

$$S_{\text{bg}}(\omega) = S_{\text{opt}}(\omega) + S_{\text{fb}}(\omega) + \Sigma_{\text{det}}. \tag{D.23}$$

From transmission noise $S_{\text{opt}}(\omega)$ measured at large photon rate in the absence of atoms, we have determined the effective laser linewidth to be $\gamma_L(\omega_t) = 2\pi \times 0.8(2)$ kHz at the trap frequency $\omega_t \approx 2\pi \times 500$ kHz (well within our 3 MHz lock bandwidth). At the photon rate $\overline{R} = 1.2 \times 10^9$/s used in the spectra of Fig. 8-4, the associated phase-noise-induced intensity

fluctuations are a factor of 1.7(5) below the photon shot noise level; correspondingly, they induce motion (included in our analysis) that is smaller than the zero-point fluctuations X_0.

In fitting the measured spectra, we constrain F, Q, γ_L and $\overline{R}$; we leave the dominant background noise contribution S_J free and obtain values consistent with the independently measured dark noise.

D.1.6 Determination of Collective Temperature

Subtracting the background level $S_{\mathrm{bg}}(\omega)$ from the measured spectrum $S_I(\omega)/\overline{I}^2$ allows us to determine $S_X(\omega)$ from Eq. D.19 and integrate it to find the occupation of the collective mode:

$$\langle n \rangle + 1/2 = \frac{1}{2} \int_0^\infty \frac{d\omega}{2\pi} S_X(\omega)/X_0^2. \tag{D.24}$$

To determine $\langle n \rangle$ in Fig. 8-2, we use not the spectrum itself but the fractional variance $\sigma_I^2 \equiv (I - \overline{I})^2/\overline{I}^2$ of the measured photocurrent $I \propto R$ in a bandwidth $B \gg \omega_t$, which is related to the spectrum $S_I(\omega)/\overline{I}^2$ by

$$\sigma_I^2 = \int_0^B \frac{d\omega}{2\pi} S_I(\omega)/\overline{I}^2 \approx \int_0^\infty \frac{d\omega}{2\pi} S_{\mathrm{mech}}(\omega) + \int_0^B \frac{d\omega}{2\pi} S_{\mathrm{bg}}(\omega). \tag{D.25}$$

We make in Eq. D.17 for $S_{\mathrm{mech}}(\omega)$ the approximation $\Pi(\omega) \approx \Pi(\omega_t) = (2/\kappa)(\mathcal{L}_+ - \mathcal{L}_-)$, which yields

$$S_{\mathrm{mech}}(\omega) \approx (2\mathcal{G}/\kappa)^2 \left| \mathcal{L}_+ - \mathcal{L}_- \right|^2 S_X(\omega). \tag{D.26}$$

Integrating Eq. D.26 allows us to obtain $\int \frac{d\omega}{2\pi} S_X(\omega)$ from σ_I^2 using Eq. D.25. The background noise term $\int_0^B \frac{d\omega}{2\pi} S_{\mathrm{bg}}(\omega)$ on the right-hand side of Eq. D.25 is independent of the occupation of the collective mode and is well approximated for the data in Fig. 8-2 by the variance $\sigma_{I,\mathrm{eq}}^2$ measured in the long-time limit. In particular, we can find the change $\langle n \rangle - \langle n \rangle_{\mathrm{eq}}$ in collective mode occupation between two different measurements $\sigma_I^2, \sigma_{I,\mathrm{eq}}^2$ of the fractional transmission variance at fixed background noise by combining Eqs. D.24-D.26:

$$\sigma_I^2 - \sigma_{I,\mathrm{eq}}^2 = 8(\mathcal{G}X_0/\kappa)^2 \left| \mathcal{L}_+ - \mathcal{L}_- \right|^2 \left(\langle n \rangle - \langle n \rangle_{\mathrm{eq}} \right). \tag{D.27}$$

The equilibrium occupation $\langle n \rangle_{\mathrm{eq}} \lesssim 3$ of the collective mode $\mathcal{X}$ is small compared to the values $\langle n \rangle$ plotted in Fig. 8-2, where mode $\mathcal{X}$ is initially excited. Therefore neglecting $\langle n \rangle_{\mathrm{eq}} \ll \langle n \rangle$, and reexpressing Eq. D.27 in terms of transmission rate variances $\sigma^2 \equiv (R - \overline{R})^2/\overline{R}^2 = \sigma_I^2 - B\Sigma_{\mathrm{det}}$ and $\sigma_{\mathrm{bg}}^2 \equiv \sigma_{I,\mathrm{eq}}^2 - B\Sigma_{\mathrm{det}}$, we obtain

$$\sigma^2 - \sigma_{bg}^2 = 8(\mathcal{G}X_0/\kappa)^2 \left| \mathcal{L}_+ - \mathcal{L}_- \right|^2 \langle n \rangle. \tag{D.28}$$

D.2 Thermodynamic Temperature

The thermodynamic axial temperature, given by the mean single-atom vibrational occupation number $\langle n_i \rangle$, is of interest both for comparison with the bath temperature inferred from the fits in Fig. 8-4 and for quantifying the suppression of recoil heating due to cavity cooling. We estimate $\langle n_i \rangle$, in an ensemble of $\mathcal{N} = 1000(100)$ atoms, by ramping off the trap over $20\ \mu s \gg 1/\omega_t$ while increasing the lattice depth of the probe to $U_{\rm p} \approx 90\hbar\omega_t$. In the probe lattice, blue-detuned by $\Delta/(2\pi) = +280$ MHz from atomic resonance, axially cold atoms localize at positions x'_i near the nodes. Before the cloud has time to expand radially, we determine the atom-probe coupling $C' = \langle \sin^2(kx'_i) \rangle$ via the cavity shift, normalized by the shift measured beforehand in the 851-nm lattice at $C = 1/2$. From $C' \approx (\langle n'_i \rangle + 1/2)\sqrt{E_{\rm r}/U_{\rm p}}$ we determine the mean vibrational level $\langle n'_i \rangle$ in the final probe lattice, which represents only an upper bound on $\langle n_i \rangle < \langle n'_i \rangle$ if the transfer into this lattice is not entirely adiabatic.

Measurements of $\langle n'_i(t) \rangle$ after applying probe light on cavity resonance ($\delta = 0$) for variable time $t \leq 100$ ms, scattering $\Gamma_{\rm sc} = 1.7(3) \times 10^4$ photons/s, show an initial temperature $\langle n'_i(0) \rangle = 6(2)$ and the expected recoil heating $d\langle n'_i \rangle/dt = (7/10)\Gamma_{\rm sc}E_{\rm r}/(\hbar\omega_t)$. Figure D-1 displays these measurements (black triangles) and compares them with the results of cavity cooling (red circles) at $\delta = -\kappa/2$ under otherwise the same conditions—in particular, at the same transmitted power, implying the same scattering rate. A linear fit to the cavity cooling data (red solid line) has a slope $d\langle n'_i \rangle/d(\Gamma_{\rm sc}t)$ that is 40(10)% lower than that of the recoil heating (black dotted line).
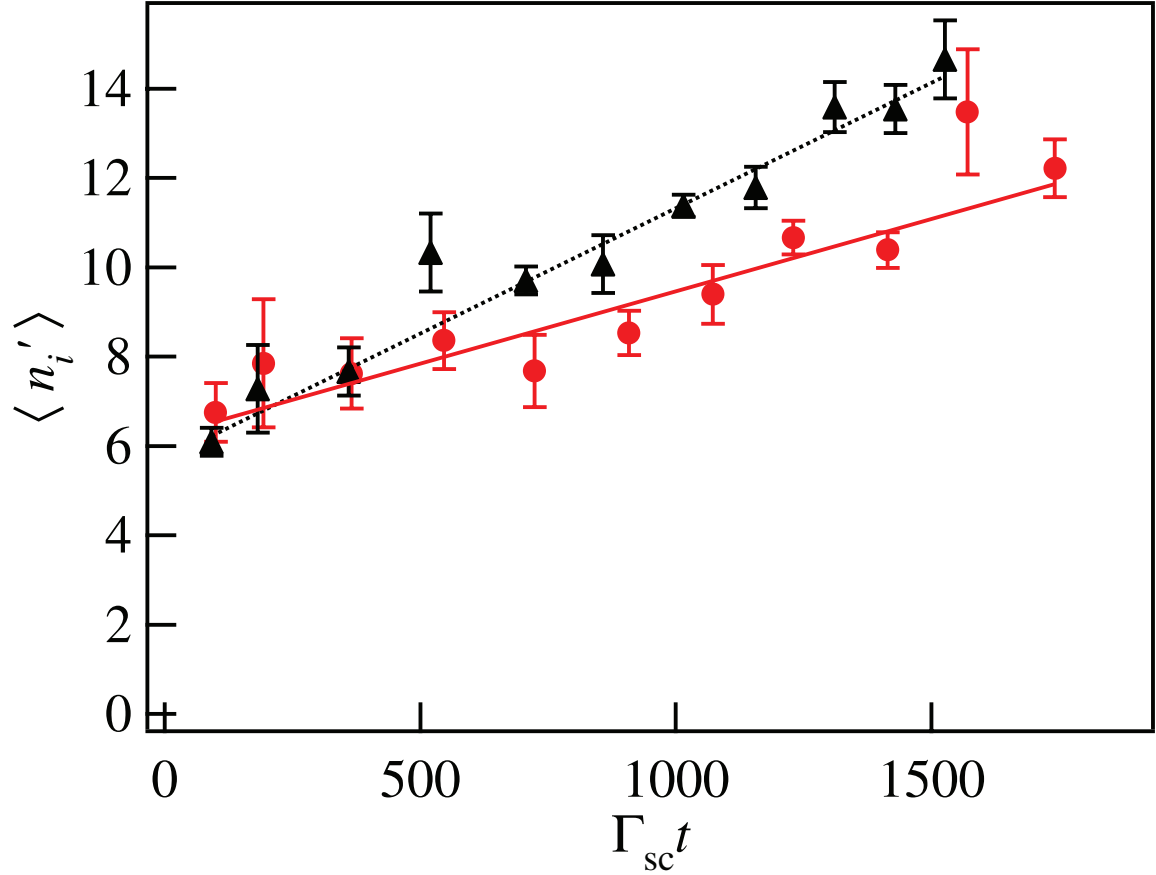
Figure D-1: Thermodynamic axial temperature $\langle n_i' \rangle$ vs number of photons scattered per atom $\Gamma_{\mathrm{sc}} t$, either with cavity cooling at $\delta = -\kappa/2$ (red) or without cavity cooling ($\delta = 0$; black). Error bars are statistical and do not include a systematic uncertainty in $\langle n_i' \rangle$ of ± 2. Black dotted line shows theoretically predicted slope $d \langle n_i' \rangle / d(\Gamma_{\mathrm{sc}} t) = (7/10) E_{\mathrm{r}} / (\hbar \omega_t) = 5.5(5) \times 10^{-3}$ for recoil heating. Red solid line is a fit to the cavity-cooling data, with reduced slope $d \langle n_i' \rangle / d(\Gamma_{\mathrm{sc}} t) = 3.5(4) \times 10^{-3}$.

Bibliography

[1] G. Santarelli, Ph. Laurent, P. Lemonde, A. Clairon, A. G. Mann, S. Chang, A. N. Luiten, and C. Salomon. Quantum projection noise in an atomic fountain: A high stability cesium frequency standard. *Phys. Rev. Lett.*, 82:4619–4622, 1999.

[2] M. Kitagawa and M. Ueda. Squeezed spin states. *Phys. Rev. A*, 47:5138, 1993.

[3] D. J. Wineland, J. J. Bollinger, W. M. Itano, F. L. Moore, and D. J. Heinzen. Spin squeezing and reduced quantum noise in spectroscopy. *Phys. Rev. A*, 46:R6797, 1992.

[4] D. J. Wineland, J. J. Bollinger, W. M. Itano, and D. J. Heinzen. Squeezed atomic states and projection noise in spectroscopy. *Phys. Rev. A*, 50:R67, 1994.

[5] A. Kuzmich, N. P. Bigelow, and L. Mandel. Atomic quantum non-demolition measurements and squeezing. *Europhys. Lett.*, 42:481, 1998.

[6] Monika H. Schleier-Smith, Ian D. Leroux, and Vladan Vuletić. States of an ensemble of two-level atoms with reduced quantum uncertainty. *Phys. Rev. Lett.*, 104:073604, 2010.

[7] J. Appel, P. Windpassinger, D. Oblak, U. Hoff, N. Kjaergaard, and E. S. Polzik. Mesoscopic atomic entanglement for precision measurements beyond the standard quantum limit. *Proceedings of the National Academy of Sciences*, 106:10960–10965, 2009.

[8] Zilong Chen, Justin G. Bohnet, Shannon R. Sankar, Jiayan Dai, and James K. Thompson. Conditional spin squeezing of a large ensemble via the vacuum rabi splitting. *Phys. Rev. Lett.*, 106:133601, 2011.

[9] Monika H. Schleier-Smith, Ian D. Leroux, and Vladan Vuletić. Squeezing the collective spin of a dilute atomic ensemble by cavity feedback. *Phys. Rev. A*, 81:021804, 2010.

[10] Ian D. Leroux, Monika H. Schleier-Smith, and Vladan Vuletić. Implementation of cavity squeezing of a collective atomic spin. *Phys. Rev. Lett.*, 104:073602, 2010.

[11] Vladan Vuletić and Steven Chu. Laser cooling of atoms, ions, or molecules by coherent scattering. *Phys. Rev. Lett.*, 84:3787–3790, 2000.

[12] Ian D. Leroux. *Squeezing Collective Atomic Spins with an Optical Resonator*. PhD thesis, Massachusetts Institute of Technology, 2011.

[13] Jacques Vanier and Claude Audoin. *The Quantum Physics of Atomic Frequency Standards*. Hilger, Philadelphia, 1989.

[14] S. Bize, P. Laurent, M. Abgrall, H. Marion, I. Maksimovic, L. Cacciapuoti, J. Grünert, C. Vian, F. Pereira dos Santos, P. Rosenbusch, P. Lemonde, G. Santarelli, P. Wolf, A. Clairon, A. Luiten, M. Tobar, and C. Salomon. Cold atom clocks and applications. *Journal of Physics B: Atomic, Molecular and Optical Physics*, 38:S449, 2005.

[15] Hidetoshi Katori. Optical lattice clocks and quantum metrology. *Nature Photonics*, 5, 2011.

[16] A. D. Ludlow, T. Zelevinsky, G. K. Campbell, S. Blatt, M. M. Boyd, M. H. G. de Miranda, M. J. Martin, J. W. Thomsen, S. M. Foreman, Jun Ye, T. M. Fortier, J. E. Stalnaker, S. A. Diddams, Y. Le Coq, Z. W. Barber, N. Poli, N. D. Lemke, K. M. Beck, and C. W. Oates. Sr Lattice Clock at 1 x 10-16 Fractional Uncertainty by Remote Optical Evaluation with a Ca Clock. *Science*, 319:1805–1808, 2008.

[17] Y. Y. Jiang, A. D. Ludlow, N. D. Lemke, R. W. Fox, J. A. Sherman, L.-S. Ma, and C. W. Oates. Making optical atomic clocks more stable with 10-16-level laser stabilization. *Nature Photonics*, 5:158–161, 2011.

[18] V. Shah, G. Vasilakis, and M. V. Romalis. High bandwidth atomic magnetometery with continuous quantum nondemolition measurements. *Phys. Rev. Lett.*, 104:013601, 2010.

[19] M. Koschorreck, M. Napolitano, B. Dubost, and M. W. Mitchell. Sub-projection-noise sensitivity in broadband atomic magnetometry. *Phys. Rev. Lett.*, 104:093602, 2010.

[20] M. Auzinsh, D. Budker, D. F. Kimball, S. M. Rochester, J. E. Stalnaker, A. O. Sushkov, and V. V. Yashchuk. Can a quantum nondemolition measurement improve the sensitivity of an atomic magnetometer? *Phys. Rev. Lett.*, 93:173002, 2004.

[21] Dmitry Budker and Michael Romalis. Optical magnetometry. *Nature Physics*, 3:227–234, 2007.

[22] W. Wasilewski, K. Jensen, H. Krauter, J. J. Renema, M. V. Balabas, and E. S. Polzik. Quantum noise limited and entanglement-assisted magnetometry. *Phys. Rev. Lett.*, 104:133601, 2010.

[23] Achim Peters, Keng Yeow Chung, and Steven Chu. Measurement of gravitational acceleration by dropping atoms. *Nature*, 400:849–852, 1999.

[24] Holger Muller, Achim Peters, and Steven Chu. A precision measurement of the gravitational redshift by the interference of matter waves. *Nature*, 463:926–929, 2010.

[25] Alexander D. Cronin, Jörg Schmiedmayer, and David E. Pritchard. Optics and interferometry with atoms and molecules. *Rev. Mod. Phys.*, 81:1051–1129, 2009.

[26] D. S. Durfee, Y. K. Shaham, and M. A. Kasevich. Long-term stability of an area-reversible atom-interferometer sagnac gyroscope. *Phys. Rev. Lett.*, 97:240801, 2006.

[27] T. Rosenband, D. B. Hume, P. O. Schmidt, C. W. Chou, A. Brusch, L. Lorini, W. H. Oskay, R. E. Drullinger, T. M. Fortier, J. E. Stalnaker, S. A. Diddams, W. C. Swann, N. R. Newbury, W. M. Itano, D. J. Wineland, and J. C. Bergquist. Frequency ratio of Al^+ and Hg^+ single-ion optical clocks; metrology at the 17th decimal place. *Science*, 319:1808–1812, 2008.

[28] C. W. Chou, D. B. Hume, J. C. J. Koelemeij, D. J. Wineland, and T. Rosenband. Frequency comparison of two high-accuracy Al$^+$ optical clocks. *Phys. Rev. Lett.*, 104:070802, 2010.

[29] R. H. Dicke. Coherence in spontaneous radiation processes. *Phys. Rev.*, 93:99, 1954.

[30] F. T. Arecchi, Eric Courtens, Robert Gilmore, and Harry Thomas. Atomic coherent states in quantum optics. *Phys. Rev. A*, 6:2211–2237, 1972.

[31] M. O. Terra Cunha, V. I. Man'ko, and M. O. Scully. Quasiprobability and probability distributions for spin-1/2 states. *Foundations of Physics Letters*, 14:103–117, 2001.

[32] A. Sørensen, L. M. Duan, J. I. Cirac, and P. Zoller. Many-particle entanglement with bose-einstein condensates. *Nature*, 409:63–66, 2001.

[33] Géza Tóth, Christian Knapp, Otfried Gühne, and Hans J. Briegel. Spin squeezing and entanglement. *Phys. Rev. A*, 79:042334, 2009.

[34] C. P. Sun Jian Ma, Xiaoguang Wang and Franco Nori. Quantum spin squeezing. 2011. arXiv:1011.2978v2.

[35] Klaus Mølmer and Anders Sørensen. Multiparticle entanglement of hot trapped ions. *Phys. Rev. Lett.*, 82:1835–1838, 1999.

[36] V. Meyer, M. A. Rowe, D. Kielpinski, C. A. Sackett, W. M. Itano, C. Monroe, and D. J. Wineland. Experimental demonstration of entanglement-enhanced rotation angle estimation using trapped ions. *Phys. Rev. Lett.*, 86:5870–5873, 2001.

[37] J. Estéve, C. Gross, A. Weller, S. Giovanazzi, and M. K. Oberthaler. Squeezing and entanglement in a bose-einstein condensate. *Nature*, 455:1216–1219, 2008.

[38] T. Gross, C.and Zibold, E. Nicklas, J. Estéve, and M. K. Oberthaler. Nonlinear atom interferometer surpasses classical precision limit. *Nature*, 464:1165–1169, 2010.

[39] Max F. Riedel, Pascal Böhi, Yun Li, Theodor W. Hänsch, Alice Sinatra, and Philipp Treutlein. Atom-chip-based generation of entanglement for quantum metrology. *Nature*, 464:1170–1173, 2010.

[40] A. Kuzmich, L. Mandel, and N. P. Bigelow. Generation of spin squeezing via continuous quantum nondemolition measurement. *Phys. Rev. Lett.*, 85:1594–1597, 2000.

[41] T. Takano, M. Fuyama, R. Namiki, and Y. Takahashi. Spin squeezing of a cold atomic ensemble with the nuclear spin of one-half. *Phys. Rev. Lett.*, 102:033601, 2009.

[42] Tetsushi Takano, Shin-Ichi-Ro Tanaka, Ryo Namiki, and Yoshiro Takahashi. Manipulation of nonclassical atomic spin states. *Phys. Rev. Lett.*, 104:013602, 2010.

[43] Anne Louchet-Chauvet, Jrgen Appel, Jelmer J Renema, Daniel Oblak, Niels Kjaergaard, and Eugene S Polzik. Entanglement-assisted atomic clock beyond the projection noise limit. *New Journal of Physics*, 12:065032, 2010.

[44] D. Leibfried, M. D. Barrett, T. Schaetz, J. Britton, J. Chiaverini, W. M. Itano, J. D. Jost, C. Langer, and D. J. Wineland. Toward Heisenberg-limited spectroscopy with multiparticle entangled states. *Science*, 304:1476–1478, 2004.

[45] Thomas Monz, Philipp Schindler, Julio T. Barreiro, Michael Chwalla, Daniel Nigg, William A. Coish, Maximilian Harlander, Wolfgang Hänsel, Markus Hennrich, and Rainer Blatt. 14-qubit entanglement: Creation and coherence. *Phys. Rev. Lett.*, 106:130506, 2011.

[46] J. Hald, J. L. Sørensen, C. Schori, and E. S. Polzik. Spin squeezed atoms: A macroscopic entangled ensemble created by light. *Phys. Rev. Lett.*, 83:1319–1322, 1999.

[47] C. Orzel, A. K. Tuchman, M. L. Fenselau, M. Yasuda, and M. A. Kasevich. Squeezed States in a Bose-Einstein Condensate. *Science*, 291:2386–2389, 2001.

[48] G.-B. Jo, Y. Shin, S. Will, T. A. Pasquini, M. Saba, W. Ketterle, D. E. Pritchard, M. Vengalattore, and M. Prentiss. Long phase coherence time and number squeezing of two Bose-Einstein condensates on an atom chip. *Phys. Rev. Lett.*, 98:030407, 2007.

[49] M. Takeuchi, S. Ichihara, T. Takano, M. Kumakura, T. Yabuzaki, and Y. Takahashi. Spin squeezing via one-axis twisting with coherent light. *Phys. Rev. Lett.*, 94:023003, 2005.

[50] Collin M. Trail, Poul S. Jessen, and Ivan H. Deutsch. Strongly enhanced spin squeezing via quantum control. *Phys. Rev. Lett.*, 105:193602, 2010.

[51] Souma Chaudhury, Seth Merkel, Tobias Herr, Andrew Silberfarb, Ivan H. Deutsch, and Poul S. Jessen. Quantum control of the hyperfine spin of a cs atom ensemble. *Phys. Rev. Lett.*, 99:163002, 2007.

[52] T. Fernholz, H. Krauter, K. Jensen, J. F. Sherson, A. S. Sørensen, and E. S. Polzik. Spin Squeezing of Atomic Ensembles via Nuclear-Electronic Spin Entanglement. *Physical Review Letters*, 101:073601, 2008.

[53] Ian D. Leroux, Monika H. Schleier-Smith, and Vladan Vuletić. Orientation-dependent entanglement lifetime in a squeezed atomic clock. *Phys. Rev. Lett.*, 104:250801, 2010.

[54] Alexander Julsgaard, Brianand Kozhekin and Eugene S. Polzik. Experimental long-lived entanglement of two macroscopic objects. *Nature*, 413:400–403, 2001.

[55] K. Hammerer, K. Mølmer, E. S. Polzik, and J. I. Cirac. Light-matter quantum interface. *Phys. Rev. A*, 70:044304, Oct 2004.

[56] Lars Bojer Madsen and Klaus Mølmer. Spin squeezing and precision probing with light and samples of atoms in the gaussian description. *Phys. Rev. A*, 70:052324, Nov 2004.

[57] E. Brion, L. H. Pedersen, and K. Mølmer. Adiabatic elimination in a lambda system. *J. Phys. A: Math. Theor.*, 40:1033–1043, 2007.

[58] Serge Haroche and Jean-Michel Raimond. *Exploring the Quantum: Atoms, Cavities, and Photons (Oxford Graduate Texts)*. Oxford University Press, USA, 2006.

[59] A. E. Siegman. *Lasers*. University Science Books, Sausalito, 1986.

[60] R. Ozeri, C. Langer, J. D. Jost, B. DeMarco, A. Ben-Kish, B. R. Blakestad, J. Britton, J. Chiaverini, W. M. Itano, D. B. Hume, D. Leibfried, T. Rosenband, P. O. Schmidt, and D. J. Wineland. Hyperfine coherence in the presence of spontaneous photon scattering. *Phys. Rev. Lett.*, 95:030403, 2005.

[61] H. Uys, M. J. Biercuk, A. P. VanDevender, C. Ospelkaus, D. Meiser, R. Ozeri, and J. J. Bollinger. Decoherence due to elastic rayleigh scattering. *Phys. Rev. Lett.*, 105:200401.

[62] Vladan Vuletić, Hilton W. Chan, and Adam T. Black. Three-dimensional cavity Doppler cooling and cavity sideband cooling by coherent scattering. *Phys. Rev. A*, 64:033405, 2001.

[63] H. J. Kimble. Strong interactions of single atoms and photons in cavity qed. *Physica Scripta*, T76:127–137, 1998.

[64] M. Saffman, D. Oblak, J. Appel, and E. S. Polzik. Spin squeezing of atomic ensembles by multicolor quantum nondemolition measurements. *Phys. Rev. A*, 79, 2009.

[65] Igor Teper. *Ultracold atoms in microfabricated magnetic traps near surfaces and inside optical resonators*. PhD thesis, Stanford University, 2006.

[66] SAES Getters S.p.A. *Alkali Metal Dispensers*, 2011. `http://www.saesgetters.com/documents/AlkaliMetalDispensers_1122.pdf`.

[67] Yu ju Lin. *Ultracold atoms magnetically trapped inside an optical resonator on a microfabricated chip.* PhD thesis, Stanford University, 2006.

[68] Igor Teper, Yuju Lin, and Vladan Vuletić. Resonator-aided single-atom detection on a microfabricated chip. *Phys. Rev. Lett.*, 97:023002, 2006.

[69] D. Boiron, A. Michaud, P. Lemonde, Y. Castin, C. Salomon, S. Weyers, K. Szymaniec, L. Cognet, and A. Clairon. Laser cooling of cesium atoms in gray optical molasses down to 1.1 μK. *Phys. Rev. A*, 53:R3734–R3737, 1996.

[70] T. A. Savard, K. M. O'Hara, and J. E. Thomas. Laser-noise-induced heating in far-off resonance optical traps. *Phys. Rev. A*, 56:R1095–R1098, 1997.

[71] Ivan H. Deutsch and Poul S. Jessen. Quantum-state control in optical lattices. *Phys. Rev. A*, 57:1972–1986, 1998.

[72] N. Lundblad, M. Schlosser, and J. V. Porto. Experimental observation of magic-wavelength behavior of ^{87}rb atoms in an optical lattice. *Phys. Rev. A*, 81:031611, 2010.

[73] R. Chicireanu, K. D. Nelson, S. Olmschenk, N. Lundblad, A. Derevianko, and J. V. Porto. Differential light-shift cancellation in a magnetic-field-insensitive transition of ^{87}rb. *Phys. Rev. Lett.*, 106:063002, 2011.

[74] Holly K. Cummins, Gavin Llewellyn, and Jonathan A. Jones. Tackling systematic errors in quantum logic gates with composite rotations. *Phys. Rev. A*, 67:042308, Apr 2003.

[75] L. M. K. Vandersypen and I. L. Chuang. Nmr techniques for quantum control and computation. *Rev. Mod. Phys.*, 76:1037–1069, 2005.

[76] R. Tycko. Broadband population inversion. *Phys. Rev. Lett.*, 51:775–777, 1983.

[77] Igor Teper, Geert Vrijsen, Jongmin Lee, and Mark A. Kasevich. Backaction noise produced via cavity-aided nondemolition measurement of an atomic clock state. *Phys. Rev. A*, 78:051803(R), 2008.

[78] Hamamatsu Photonics K.K., Solid State Division. *Technical Information SD-28: Characteristics and Use of Si APD (Avalanche Photodiode)*, 2004. http://sales.hamamatsu.com/assets/applications/SSD/Characteristics_and_use_of_SI_APD.pdf.

[79] Monika H. Schleier-Smith, Ian D. Leroux, and Vladan Vuletić. States of an ensemble of two-level atoms with reduced quantum uncertainty: Auxiliary material. *Phys. Rev. Lett.*, 104:073604, 2010. Supplementary material available at http://link.aps.org/supplemental/10.1103/PhysRevLett.104.073604.

[80] Vladimir B. Braginsky, Yuri I. Vorontsov, and Kip S. Thorne. Quantum nondemolition measurements. 209:547–557, 1980.

[81] Carlton M. Caves, Kip S. Thorne, Ronald W. P. Drever, Vernon D. Sandberg, and Mark Zimmermann. On the measurement of a weak classical force coupled to a quantum-mechanical oscillator. i. issues of principle. *Rev. Mod. Phys.*, 52:341–392, 1980.

[82] C. W. Gardiner and M. J. Collett. Input and output in damped quantum systems: Quantum stochastic differential equations and the master equation. *Phys. Rev. A*, 31:3761–3774, 1985.

[83] D.F. Walls and G. J. Milburn. *Quantum Optics*. Springer, Heidelberg, 1994.

[84] Anders S. Sørensen and Klaus Mølmer. Entanglement and extreme spin squeezing. *Phys. Rev. Lett.*, 86:4431–4434, 2001.

[85] Jonathan P. Dowling, G. S. Agarwal, and Wolfgang P. Schleich. Wigner distribution of a general angular-momentum state: Applications to a collection of two-level atoms. *Phys. Rev. A*, 49:4101–4109, 1994.

[86] G. S. Agarwal. State reconstruction for a collection of two-level systems. *Phys. Rev. A*, 57:671–673, Jan 1998.

[87] Roman Schmied and Philipp Treutlein. Tomographic reconstruction of the wigner function on the bloch sphere. 2011. arXiv:1101.4131v2[quant-ph].

[88] S. F. Huelga, C. Macchiavello, T. Pellizzari, A. K. Ekert, M. B. Plenio, and J. I. Cirac. Improvement of frequency standards with quantum entanglement. *Phys. Rev. Lett.*, 79:3865–3868, 1997.

[89] A. André, A. S. Sørensen, and M. D. Lukin. Stability of atomic clocks based on entangled atoms. *Phys. Rev. Lett.*, 92:230801, 2004.

[90] Philipp Treutlein, Peter Hommelhoff, Tilo Steinmetz, Theodor W. Hänsch, and Jakob Reichel. Coherence in microchip traps. *Phys. Rev. Lett.*, 92:203005, 2004.

[91] V. Vuletić, I. D. Leroux, and M. H. Schleier-Smith. Microchip-based trapped-atom clocks. In J. Reichel and V. Vuletić, editors, *Atom chips*, pages 265–282. Wiley-VCH, Weinheim, Germany, 2011.

[92] Matthew D. Swallows, Michael Bishof, Yige Lin, Sebastian Blatt, Michael J. Martin, Ana Maria Rey, and Jun Ye. Suppression of collisional shifts in a strongly interacting lattice clock. *Science*, 331:1043–1046, 2011.

[93] Jun Ye, H. J. Kimble, and Hidetoshi Katori. Quantum state engineering and precision metrology using state-insensitive light traps. *Science*, 320:1734–1738, 2008.

[94] Peter Horak, Gerald Hechenblaikner, Klaus M. Gheri, Herwig Stecher, and Helmut Ritsch. Cavity-induced atom cooling in the strong coupling regime. *Phys. Rev. Lett.*, 79:4974–4977, 1997.

[95] Peter Domokos and Helmut Ritsch. Mechanical effects of light in optical resonators. *J. Opt. Soc. Am. B*, 20:1098–1130, 2003.

[96] K. Murr. Large velocity capture range and low temperatures with cavities. *Phys. Rev. Lett.*, 96:253001, 2006.

[97] P. Maunz, T. Puppe, I. Schuster, N. Syassen, P. W. H. Pinkse, and G. Rempe. Cavity cooling of a single atom. *Nature*, 428:50–52, 2004.

[98] Stefan Nußmann, Karim Murr, Markus Hijlkema, Bernhard Weber, Axel Kuhn, and Gerhard Rempe. Vacuum-stimulated cooling of single atoms in three dimensions. *Nature Physics*, 1:122–125, 2005.

[99] Tobias Kampschulte, Wolfgang Alt, Stefan Brakhane, Martin Eckstein, René Reimann, Artur Widera, and Dieter Meschede. Optical control of the refractive index of a single atom. *Phys. Rev. Lett.*, 105:153603, 2010.

[100] David R. Leibrandt, Jaroslaw Labaziewicz, Vladan Vuletić, and Isaac L. Chuang. Cavity sideband cooling of a single trapped ion. *Phys. Rev. Lett.*, 103:103001, 2009.

[101] Hilton W. Chan, Adam T. Black, and Vladan Vuletić. Observation of collective-emission-induced cooling of atoms in an optical cavity. *Phys. Rev. Lett.*, 90:063003, 2003.

[102] Adam T. Black, Hilton W. Chan, and Vladan Vuletić. Observation of collective friction forces due to spatial self-organization of atoms: From rayleigh to bragg scattering. *Phys. Rev. Lett.*, 91:203001, 2003.

[103] D. Kruse, C. von Cube, C. Zimmermann, and Ph. W. Courteille. Observation of lasing mediated by collective atomic recoil. *Phys. Rev. Lett.*, 91:183601, 2003.

[104] B. Nagorny, Th. Elsässer, and A. Hemmerich. Collective atomic motion in an optical lattice formed inside a high finesse cavity. *Phys. Rev. Lett.*, 91:153003, 2003.

[105] Ferdinand Brennecke, Stephan Ritter, Tobias Donner, and Tilman Esslinger. Cavity optomechanics with a bose-einstein condensate. *Science*, 322:235–238, 2008.

[106] K. W. Murch, K. L. Moore, S. Gupta, and D. M. Stamper-Kurn. Observation of quantum-measurement backaction with an ultracold atomic gas. *Nature Physics*, 4:561–564, 2008.

[107] T. P. Purdy, D. W. C. Brooks, T. Botter, N. Brahms, Z.-Y. Ma, and D. M. Stamper-Kurn. Tunable cavity optomechanics with ultracold atoms. *Phys. Rev. Lett.*, 105:133602, 2010.

[108] Benjamin L. Lev, András Vukics, Eric R. Hudson, Brian C. Sawyer, Peter Domokos, Helmut Ritsch, and Jun Ye. Prospects for the cavity-assisted laser cooling of molecules. *Phys. Rev. A*, 77:023402, 2008.

[109] Giovanna Morigi, Pepijn W. H. Pinkse, Markus Kowalewski, and Regina de Vivie-Riedle. Cavity cooling of internal molecular motion. *Phys. Rev. Lett.*, 99:073001, 2007.

[110] A Griessner, D Jaksch, and P Zoller. Cavity-assisted nondestructive laser cooling of atomic qubits. *Journal of Physics B: Atomic, Molecular and Optical Physics*, 37:1419, 2004.

[111] V. B. Braginsky and A. B. Manukin. *Measurement of weak forces in physics experiments.* University of Chicago Press, Chicago, 1977.

[112] Florian Marquardt, Joe P. Chen, A. A. Clerk, and S. M. Girvin. Quantum theory of cavity-assisted sideband cooling of mechanical motion. *Phys. Rev. Lett.*, 99:093902, 2007.

[113] I. Wilson-Rae, N. Nooshi, W. Zwerger, and T. J. Kippenberg. Theory of ground state cooling of a mechanical oscillator using dynamical backaction. *Phys. Rev. Lett.*, 99:093901, 2007.

[114] T. J. Kippenberg and K. J. Vahala. Cavity Optomechanics: Back-Action at the Mesoscale. *Science*, 321:1172–1176, 2008.

[115] O. Arcizet, P. F. Cohadon, T. Briant, M. Pinard, and A. Heidmann. Radiation-pressure cooling and optomechanical instability of a micromirror. *Nature*, 444:71–74, 2006.

[116] S. Gigan, H. R. Bohm, M. Paternostro, F. Blaser, G. Langer, J. B. Hertzberg, K. C. Schwab, D. Bauerle, M. Aspelmeyer, and A. Zeilinger. Self-cooling of a micromirror by radiation pressure. *Nature*, 444:67–70, 2006.

[117] J. D. Thompson, B. M. Zwickl, A. M. Jayich, Florian Marquardt, S. M. Girvin, and J. G. E. Harris. Strong dispersive coupling of a high-finesse cavity to a micromechanical membrane. *Nature*, 452:72–75, 2008.

[118] A. Schliesser, O. Arcizet, R. Riviere, G. Anetsberger, and T. J. Kippenberg. Resolved-sideband cooling and position measurement of a micromechanical oscillator close to the heisenberg uncertainty limit. *Nature Physics*, 5:509–514, 2009.

[119] T. Rocheleau, T. Ndukum, C. Macklin, J. B. Hertzberg, A. A. Clerk, and K. C. Schwab. Preparation and detection of a mechanical resonator near the ground state of motion. *Nature*, 463:72–75, 2010.

[120] Kip S. Thorne, Ronald W. P. Drever, Carlton M. Caves, Mark Zimmermann, and Vernon D. Sandberg. Quantum nondemolition measurements of harmonic oscillators. *Phys. Rev. Lett.*, 40:667–671, 1978.

[121] M. S. Kim C. Brukner K. Hammerer G. J. Milburn M. Aspelmeyer M. R. Vanner, I. Pikovski. Pulsed quantum optomechanics. 2010. arXiv:1011.0879v1 [quant-ph].

[122] K. Hammerer, M. Wallquist, C. Genes, M. Ludwig, F. Marquardt, P. Treutlein, P. Zoller, J. Ye, and H. J. Kimble. Strong coupling of a mechanical oscillator and a single atom. *Phys. Rev. Lett.*, 103:063005, 2009.

[123] R. W. P. Drever, J. L. Hall, F. V. Kowalski, J. Hough, G. M. Ford, A. J. Munley, and H. Ward. Laser phase and frequency stabilization using an optical resonator. *Applied Physics B*, 31:97–105, 1983.

[124] Eric D. Black. An introduction to pound–drever–hall laser frequency stabilization. *American Journal of Physics*, 69:79–87, 2001.

[125] L. Cacciapuoti, M. de Angelis, M. Fattori, G. Lamporesi, T. Petelski, M. Prevedelli, J. Stuhler, and G. M. Tino. Analog + digital phase and frequency detector for phase locking of diode lasers. *Rev. Sci. Instrum.*, 76:1–7, 2005.

[126] Carl E. Wieman and Leo Hollberg. Using diode lasers for atomic physics. *Rev. Sci. Instrum.*, 62:1–20, 1991.

[127] P. Rabl, C. Genes, K. Hammerer, and M. Aspelmeyer. Phase-noise induced limitations on cooling and coherent evolution in optomechanical systems. *Phys. Rev. A*, 80:063819, 2009.

[128] A. A. Clerk, M. H. Devoret, S. M. Girvin, Florian Marquardt, and R. J. Schoelkopf. Introduction to quantum noise, measurement, and amplification. *Rev. Mod. Phys.*, 82:1155–1208, 2010. Also see online appendices at `http://rmp.aps.org/epaps/RMP/v82/i2/p1155_1/QNoiseRMPAppsApr2010.pdf`.

[129] G. Audoin. Frequency metrology. In P. Giacomo A. F. Milone and F. Leschiutta, editors, *Metrology and Fundamental Constants, corso 68 of the International School of Physics Enrico Fermi*, pages 169–222. North-Holland, Amsterdam, 1980.

[130] C. W. Gardiner and P. Zoller. *Quantum Noise.* Springer, Berlin, 2000.